Optomechanics in a 3D microwave cavity

Cohen, Martijn

DOI
10.4233/uuid:c946f596-54fd-41b1-b43b-63b8f9457ef8

Publication date
2019

Document Version
Final published version

Citation (APA)
Cohen, M. (2019). *Optomechanics in a 3D microwave cavity*. [Dissertation (TU Delft), Delft University of Technology]. https://doi.org/10.4233/uuid:c946f596-54fd-41b1-b43b-63b8f9457ef8

OPTOMECHANICS IN A 3D MICROWAVE CAVITY

OPTOMECHANICS IN A 3D MICROWAVE CAVITY

Proefschrift

ter verkrijging van de graad van doctor
aan de Technische Universiteit Delft,
op gezag van de Rector Magnificus prof. dr. ir. T. H. J. J. van der Hagen,
voorzitter van het College voor Promoties,
in het openbaar te verdedigen op woensdag 16 januari 2019 om 10:00 uur

door

Martijn Antonio COHEN

Master of Science in Chemical Physics,
University College London, Londen, Verenigd Koningrijk,
geboren te New York, Verenigde Staten.

Dit proefschrift is goedgekeurd door de

promotor: Prof. dr. G. A. Steele
promotor: Prof. dr. Y. M. Blanter

Samenstelling promotiecommissie:

Rector Magnificus,	voorzitter
Prof. dr. G. A. Steele,	Technische Universiteit Delft
Prof. dr. Y. M. Blanter,	Technische Universiteit Delft
Dr. R. Norte,	Technische Universiteit Delft
Prof. dr. W. Tittel,	Technische Universiteit Delft
Prof. dr. ir. T. H. Oosterkamp,	Universiteit Leiden
Dr. I. Wilson-Rae,	University of York
Prof. dr. E. Weig,	Universität Konstanz
Prof. dr. P. G. Steeneken,	Technische Universiteit Delft, reservelid

Keywords: cavity optomechanics, silicon nitride resonators, superconducting circuits

Printed by: IPSKAMP

Front & Back: Procedurally generated image written in C++/GLSL using the OpenGL API. Source code: `github.com/mtMartijn/cover`.

Casimir PhD Series, Delft-Leiden 2018-18

ISBN 978-94-028-1349-4

An electronic version of this dissertation is available at
http://repository.tudelft.nl/.

To my parents

CONTENTS

1

INTRODUCTION

1

1.1. COUPLING RESONATORS

Resonators are one of the most fundamental and important models in physics. A resonator is any object that has a natural frequency at which it shows oscillatory motion. There are countless objects and devices that rely on this simple physical fact at a wide range of frequencies:

- A pendulum clock has a frequency which is used to keep track of time (~ Hz).
- The resonance frequency of a guitar string is what gives it its pitch (~ kHz).
- Central processing units in a computer use a quartz resonator to synchronize microinstructions (~ GHz).

Furthermore, these three systems are different *types* of resonators. The first two systems are mechanical resonators, as their oscillating variable is position (some make a distinction between the two, preferring to call a guitar string an acoustic resonator, although this merely explains the difference in frequency). The last example is an electromagnetic resonator, where the oscillating variable is electric current, or voltage. Resonators are so ubiquitous because almost any system that has a local minimum of potential energy will exhibit oscillatory motion.

If one puts a large assembly of resonators within close proximity one will create travelling waves, which are more often referred to as waves. Once one resonator starts oscillating, the one next to it will also oscillate, and so on, forming a ripple through which a wavefront travels. Sound and surface waves are prime examples of this. For sound, air molecules colliding with each other play the role of mechanical resonators. Waves have a few properties which are counterintuitive. Waves transfer energy from location to location, however, there is no net transfer of mass. While ocean waves may crash on shore and emit energy in the form of heat and sound, in theory, its constituent water molecules do not travel long distances. Waves also add up to each other in ways which are unusual

Figure 1.1: Examples of resonators which are commonly found in everyday life. A pendulum clock, a guitar string, and a quartz resonator of a central processing unit [1, 2].

for solid objects – such as particles, for example – in a process called interference. When waves overlap *in-phase*, i.e. when their peaks overlap with other peaks, they constructively interfere, and the amplitudes of the waves amplify. In contrast, when they interfere *out-of-phase*, the peaks and troughs overlap and destructively interfere. This effectively cancels the propagation of the wave. Full cancellation of a travelling wave necessitates that the waves are constructed from the same frequencies. Usually wavefronts are made up of multiple frequencies and the resulting waveshape is a complex and irregular combination of peaks and troughs which requires rigorous analysis to fully understand.

Imagine if one constructs a long tube with two mirrors at both ends and a light source is placed inside it which emits light in many frequencies. A traveling light wave will be formed and will propagate along the tube, bouncing off both mirrors until an equilibrium is formed. The steady state wave will favor frequencies which constructively interfere inside this tube and these will be the ones where the antinodes match up with the mirrors. One can then conclude that travelling waves, when given appropriate boundary conditions, will also themselves exhibit a natural resonance frequency through interference. Such a construction of two mirrors is called a Fabry-Pérot cavity, or, more generally, a cavity.

Interferometers are a useful tool for measuring movement and position at high sensitivities, and rely on the ability of waves to interfere. Let's take a Fabry-Pérot cavity and assume that one of its mirrors is itself a harmonic oscillator and moves slightly back and forth. The position of this mirror will determine the natural resonance of the cavity, and by interfering this with a reference frequency we can correlate the intensity of the interference to a position of the mirror. This is the operating principle of an interferometer, although there are many variations on its design. An optomechanical system, such as the one studied in this thesis, is very similar to an interferometer, except its parameters are stretched to its limits to give rise to unique effects.

The system is engineered such that loss rates of both the cavity and mechanics are minimized and the interaction between them is maximized. This greatly increases the sensitivity of measurement, and allows us to gain high-precision information about the mirror. The further this sensitivity is increased the more relevant the following question becomes: how does the light influence the mirror?

1.2. A BRIEF HISTORY OF CAVITY OPTOMECHANICS

Radiation pressure was first proposed by Johannes Kepler almost four hundred years ago [3] as a justification for observing that the tails of comets deviated away from the sun. Conditions for detecting it in the laboratory, however, are far more difficult and scientists only succeeded in measuring it in 1900 [4, 5]. The apparatus that they used consisted of a suspended silver-coated mirror which would show torsion when pressure was applied. When a strong source of light was shone on it, it deflected, revealing an incredibly feeble force.

Radiation pressure in the context of optomechanics was explored most notably by Vladimir Braginsky, whose main interest was the use of ultrasensitive interferometers for the detection of gravitational waves. (Many of his innovations have been included in the

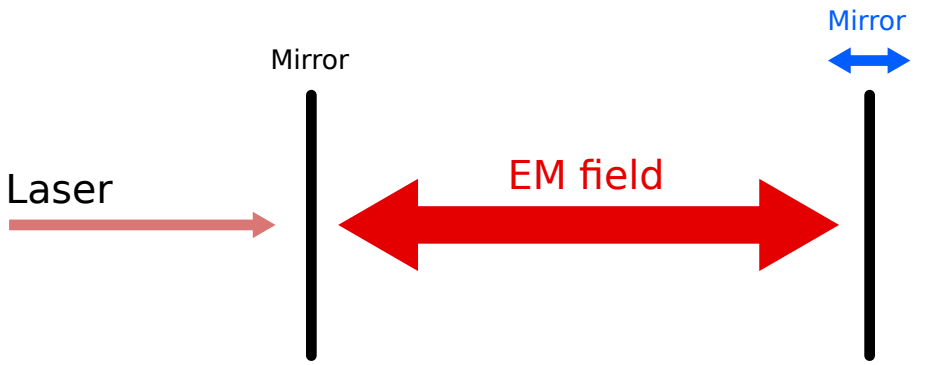

Figure 1.2: The most simplistic model of an optomechanical system. A laser is shone onto a cavity made of two opposing mirrors where one of the mirrors is free to oscillate. An optomechanical device is made up of two coupled resonators – the electromagnetic field, and the mechanical mirror.

design of the LIGO interferometers which succeeded in direct detection of gravitational waves only a few years ago [6].) Braginsky predicted that the influence of the mechanical motion on the frequency of the cavity combined with phase-delayed radiation pressure could result in a feedback loop effect called dynamical backaction. This would allow one to control the energy dissipation rate of the mechanical oscillator and effectively heat or cool it depending on the frequency of your input light field. Furthermore, he experimentally verified this mechanism in two separate experiments in the late 60s [7, 8].

Dynamical backaction is a feedback mechanism which is purely classical and doesn't depend on the quantization of light for its interpretation. Quantum backaction, however, also plays a role, and is especially important when investigating the limits of measurement sensitivity. The quantized nature of light means that there will be noise associated with the randomness of photons arriving at the sensor. Increasing the photon number of your light field will improve your signal-to-noise ratio – the downside being that this reduction in noise will be accompanied by an increase in imprecision due to the increased amount of momentum imparted onto the mechanical oscillator. The optimum balance of these two imprecision sources is called the standard quantum limit [9]. Braginsky further improved on this limit by demonstrating that if one chooses to only measure one quadrature of the oscillating light field, one can go beyond this imprecision limit [10].

Researchers also became interested in using radiation pressure to control the behavior of the mechanical oscillator at the quantum level. The creation of Fock states, superposition states, and entangled states had already been achieved with small particles such as electrons and even molecules, but was a greater challenge for the collective motion of more massive objects. Most protocols for creating quantum states dictated that the oscillator should be at, or near, the ground state, and with many mechanical oscillators having below GHz resonances would require active cooling. This was achieved

by two separate groups in the microwave and optical regime in 2011 [11, 12]. A few years later, a phononic crystal cavity was prepared in a Fock state using postselection [13], and a superconducting drum was prepared in a superposition between ground and excited state [14]. It should be noted that the creation of a macroscopic mechanical superposition state was already achieved in 2010 [15], however, they coupled the mechanical state using a piezoelectric material, not radiation pressure. Researchers have also succeeded in entangling a mechanical resonator with microwave fields [16], and has now been achieved between two separate micromechanical resonators [17, 18].

1.3. THESIS OUTLINE

Chapter 2 discusses the basic background that is necessary for the remainder of this thesis. The optomechanical equations of motion are derived from the standard harmonic oscillator, while also deriving an expression for the reflection coefficient of the cavity. The mode structure and loss mechanisms are discussed for both harmonic oscillators: Silicon nitride membranes and 3D microwave cavities. Some relations that are useful for an integrated capacitive optomechanical system is also given.

Chapter 3 gives a description of the fabrication steps that were made in creating the samples for this thesis. We start with a study on the metalization of commercial silicon nitride membrane resonators. We also go over the fabrication of specially designed trampoline resonators which increase the quality factor considerably, and also discuss the process of metalizing them. Next, the fabrication of the antenna chip and machining of the 3D cavity is covered. A lengthy discussion is reserved for the details of performing the flip-chip with a metalized membrane and an antenna chip with different methods. A last section is dedicated to outlining the measurement systems.

Chapter 4 covers an experiment that we performed where we cooled commercial metalized silicon nitride membranes to dilution refrigerator temperatures. We observe a large increase in quality factor for certain modes and give a brief justification for why we believe this effect occurs.

Chapter 5 is a chapter which explains our design for a split 3D microwave cavity which allows it to be biased with a DC voltage. The reasoning behind the design is discussed and we describe measurements at both room temperature and in a dilution refrigerator. We show that the high quality factor of the cavity is retained even when we introduce the split and add a DC bias to it.

Chapter 6 discusses an optomechanical system with a silicon nitride membrane and a low quality factor 3D microwave cavity. We observe amplification of our microwave probe tone when measuring optomechanically induced transparency in the side-band unresolved limit. The justification of the amplification reveals a mechanism that does not depend on any dynamical effects, but purely on frequency mixing. Furthermore, the configuration has the ability to reach quantum-limited amplification easily attainable in dilution refrigerators.

1

REFERENCES

[1] Megatherium, *Striking pendulum wall clock with mainspring, anchor escapement, pendulum with bob of sheet metal and wooden rod. Manufactured by Junghans, early or mid 20th century.* (Wikimedia Commons, 2016).

[2] Fir0002/Flagstaffotos - flagstaffotos.com.au, *AMD X2 3600* (Wikimedia Commons).

[3] J. Kepler, *De cometis libelli tres ...*, De cometis libelli tres (Typis Andreæ Apergeri, sumptibus Sebastiani Mylii bibliopolæ Augustani, 1619).

[4] P. Lebedew, *Untersuchungen über die druckkräfte des lichtes,* Annalen der Physik **311**, 433 (1901).

[5] E. F. Nichols and G. Hull, *A preliminary communication on the pressure of heat and light radiation,* Physical Review (Series I) **13**, 307 (1901).

[6] B. P. Abbott, R. Abbott, T. Abbott, M. Abernathy, F. Acernese, K. Ackley, C. Adams, T. Adams, P. Addesso, R. Adhikari, *et al.*, *Observation of gravitational waves from a binary black hole merger,* Physical review letters **116**, 061102 (2016).

[7] V. Braginski and A. Manukin, *Ponderomotive effects of electromagnetic radiation,* Sov. Phys. JETP **25**, 653 (1967).

[8] V. Braginskii, A. B. Manukin, and M. Y. Tikhonov, *Investigation of dissipative ponderomotive effects of electromagnetic radiation,* Soviet Journal of Experimental and Theoretical Physics **31**, 829 (1970).

[9] V. B. Braginsky, V. B. Braginsky, and F. Y. Khalili, *Quantum measurement* (Cambridge University Press, 1995).

[10] V. B. Braginsky and F. Y. Khalili, *Quantum nondemolition measurements: the route from toys to tools,* Reviews of Modern Physics **68**, 1 (1996).

[11] J. Chan, T. M. Alegre, A. H. Safavi-Naeini, J. T. Hill, A. Krause, S. Gröblacher, M. Aspelmeyer, and O. Painter, *Laser cooling of a nanomechanical oscillator into its quantum ground state,* Nature **478**, 89 (2011).

[12] J. Teufel, T. Donner, D. Li, J. Harlow, M. Allman, K. Cicak, A. Sirois, J. D. Whittaker, K. Lehnert, and R. W. Simmonds, *Sideband cooling of micromechanical motion to the quantum ground state,* Nature **475**, 359 (2011).

[13] S. Hong, R. Riedinger, I. Marinković, A. Wallucks, S. G. Hofer, R. A. Norte, M. Aspelmeyer, and S. Gröblacher, *Hanbury brown and twiss interferometry of single phonons from an optomechanical resonator,* Science **358**, 203 (2017).

[14] A. Reed, K. Mayer, J. Teufel, L. Burkhart, W. Pfaff, M. Reagor, L. Sletten, X. Ma, R. Schoelkopf, E. Knill, *et al.*, *Faithful conversion of propagating quantum information to mechanical motion,* Nature Physics **13**, 1163 (2017).

[15] A. D. O'Connell, M. Hofheinz, M. Ansmann, R. C. Bialczak, M. Lenander, E. Lucero, M. Neeley, D. Sank, H. Wang, M. Weides, *et al.*, *Quantum ground state and single-phonon control of a mechanical resonator,* Nature **464**, 697 (2010).

[16] T. Palomaki, J. Teufel, R. Simmonds, and K. Lehnert, *Entangling mechanical motion with microwave fields,* Science , 1244563 (2013).

[17] R. Riedinger, A. Wallucks, I. Marinković, C. Löschnauer, M. Aspelmeyer, S. Hong, and S. Gröblacher, *Remote quantum entanglement between two micromechanical oscillators,* Nature **556**, 473 (2018).

[18] C. Ockeloen-Korppi, E. Damskägg, J.-M. Pirkkalainen, M. Asjad, A. Clerk, F. Massel, M. Woolley, and M. Sillanpää, *Stabilized entanglement of massive mechanical oscillators,* Nature **556**, 478 (2018).

2

BACKGROUND AND THEORY

This chapter introduces the basic theoretical foundation that is necessary to understand the other chapters in this thesis. We start from individual resonators with the harmonic oscillator, and introduce important parameters such as quality factor and loss rate. From this point we reformulate the harmonic oscillator in a way that allows us to apply this to cavities which have external coupling, and derive an expression for the reflection coefficient. Optomechanical systems are mechanical oscillators coupled to an electromagnetic cavity and we use our previous expressions to create coupled differential equations. This is also the starting point for understanding an interference effect called optomechanically induced reflection. We continue with the background of silicon nitride membrane and put special emphasis on understanding the loss mechanism, and we follow by doing the same for 3D rectangular cavities. Lastly, we briefly explore an optomechanical system where the coupling is due to an oscillating capacitor.

2.1. OPTOMECHANICS: COUPLED HARMONIC OSCILLATORS

Harmonic oscillators are one of the most important and fundamental physical systems, and are essential in understanding an optomechanical system. In layman's terms, a harmonic oscillator is system in which a variable oscillates over time.

2.1.1. MECHANICAL RESONATORS

For the sake of intuition, we will discuss a mechanical oscillator with position as the oscillating variable, as in a pendulum. The key component of a mechanical oscillator is that there is a restoring force F, which is negatively proportional to the displacement x

$$F = -kx \tag{2.1}$$

where k is known as the spring constant. Using Newton's second law we transform this into a second order differential equation

$$F = m\ddot{x} = -kx \tag{2.2}$$

where $\ddot{x}$ is the second derivative of position over time, and m is the mass. We can solve this differential equation, and end up with periodic motion

$$x(t) = A\cos(\Omega_{\mathrm{m}} t + \phi) \tag{2.3}$$

where A is the amplitude, ϕ is the phase offset, and $\Omega_{\mathrm{m}} = \sqrt{k/m}$ is the resonance frequency. This is the simplest and most ideal example of a mechanical oscillator, and is thus fairly inaccurate in the real world. We need to introduce a loss term and a driving term.

$$\frac{F}{m} = \ddot{x} + \Gamma_{\mathrm{m}}\dot{x} + \Omega_{\mathrm{m}}^2 x \tag{2.4}$$

The term on the left hand side is the external force, divided by the mass of the mechanical oscillator. The second term on the right is the damping term, and Γ_{m} is the loss rate expressed as a frequency. Since the loss rate and frequency both have the same units, we can define a dimensionless constant called the quality factor, or Q-factor, $Q = \Omega_{\mathrm{m}}/\Gamma_{\mathrm{m}}$. One can see this variable as the decay time times 2π normalized by the period of the resonator. Alternatively, the Q-factor is the energy stored, divided by the energy loss per cycle of the resonator.

$$Q = \omega\frac{E}{P_{\mathrm{d}}} \tag{2.5}$$

where ω is the frequency, E is the total energy, and P_{d} is the mean dissipated power. The equivalency of these two definitions of Q-factor is only relevant in the underdamped or high-Q regime, where $Q \gg 1$ for both mechanical and cavity resonators. Optomechanical experiments are generally inside this limit.

The quality factor of a mechanical oscillator can be measured in two different ways: through a spectral response or a ringdown measurement [1]. In a spectral response measurement one sweeps the driving frequency and measures the steady state response of

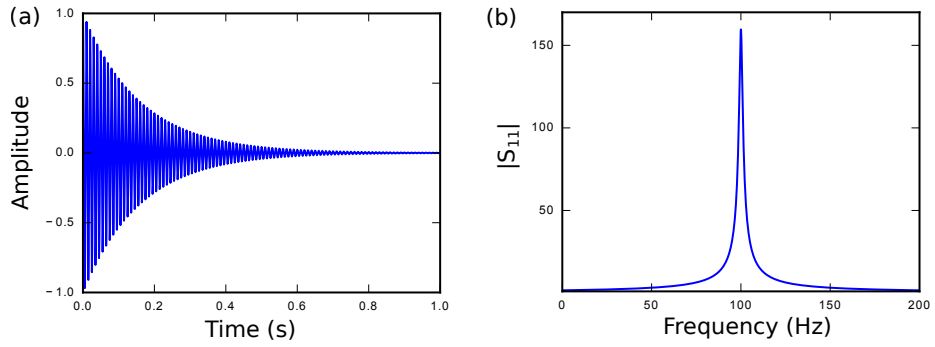

Figure 2.1: A visualization of the two ways one can measure the loss rate of a harmonic oscillator. (a) A measurement of the amplitude of the mechanical oscillator over time, where one sees an exponential decay which is proportional to a decay constant. (b) A reflection measurement of the mechanical oscillator in frequency space.

the mechanical oscillator. The linewidth of this response is inversely proportional to quality factor. In a ringdown measurement, one drives the mechanical oscillator resonantly and observes the decay in the amplitude when one turns off the driving. A ringdown measurement only measures energy dissipation, while a spectral response measures both energy dissipation and dephasing – such as instability in the resonance frequency of the resonator. Examples of such measurements are given in Fig. 2.1.

2.1.2. ELECTROMAGNETIC CAVITY RESONATORS

We now want to create an electromagnetic analog of the mechanical differential equation. This derivation follows closely the method used in Ref. [2]. For this the simplest model that we can study is an LC-circuit, where an inductor and capacitor are in parallel. Voltage V and current I can be related to each other using the following coupled first-order differential equations

$$V = L\frac{dI}{dt} \tag{2.6}$$

$$I = -C\frac{dV}{dt} \tag{2.7}$$

where L and C are the inductance and capacitance, respectively. These two equations can be rewritten in a more familiar form

$$\ddot{V} = -\omega^2 V \tag{2.8}$$

which is identical to the simple harmonic oscillator differential equation we derived above for the mechanics, the only difference being that position is substituted for volt-

age. Here, $\omega = 1/\sqrt{LC}$. We also get similar periodic solutions for these equations:

$$V(t) = |V_0|\cos(\omega t + \phi) \tag{2.9}$$

$$I(t) = \sqrt{\frac{C}{L}}|V_0|\sin(\omega t + \phi) \tag{2.10}$$

where V_0 is the peak voltage. By defining the following complex variables

$$a_\pm = \sqrt{\frac{C}{2}}V \pm i\sqrt{\frac{L}{2}}I \tag{2.11}$$

we are able to rewrite the second order differential equation as two *uncoupled* first-order differential equations:

$$\dot{a}_\pm = \pm i\omega a_\pm \tag{2.12}$$

We can discern what the meaning is of these complex variables by inserting the previous solutions into it

$$a_+ = \sqrt{\frac{C}{2}}|V_0|\big[\cos(\omega t + \phi) + i\sin(\omega t + \phi)\big] = \sqrt{\frac{C}{2}}|V_0|e^{i(\omega t+\phi)} \tag{2.13}$$

This is normalized such that the square magnitude is equal to the total energy inside the cavity $|a_+|^2 = \frac{C}{2}|V_0|^2 = E$. We can see that a_+ is an oscillation in complex form, and a_- is its conjugate so we only use a_+ in our next derivations. a_+ is called the *positive frequency component* of the mode amplitude.

Let's add an imaginary component to the resonance frequency $\omega \to \omega + i\sigma$ in an attempt to include losses into the system.

$$\dot{a}_+ = i\omega a_+ - \sigma a_+ \tag{2.14}$$

We can calculate the dissipation rate by taking the derivative of the total energy

$$\dot{E} = -2\sigma E = -P_\mathrm{d} \tag{2.15}$$

If we use the definition of Q factor $Q = \omega E/P_\mathrm{d} = \omega/\kappa$, where κ is the dissipation rate of the mechanical oscillator, we realize that the imaginary component of the frequency $\sigma = \kappa/2$. We now have a complete differential equation of the complex frequency which includes losses. Note, however, that this equation is actually an approximation, and only holds in the high-Q limit, i.e. $\kappa \ll \omega$. Still, our picture is incomplete, because we want to be able to model the effect of an input signal which is coupled to this harmonic oscillator. For this we need to add another term and the full equation is as follows

$$\dot{a}_+ = i\omega a_+ - \frac{\kappa}{2}a_+ + \sqrt{\kappa_\mathrm{e}}s_+ \tag{2.16}$$

where the term $\sqrt{\kappa_\mathrm{e}}s_+$ is the incident wave on the port of the cavity multiplied by the external coupling, such that the total coupling (loss) is the sum of external and internal coupling $\kappa = \kappa_\mathrm{e} + \kappa_\mathrm{i}$. $|s_+|^2$ is normalized to the *power* instead of the *energy*, which justifies the square root on the external coupling constant.

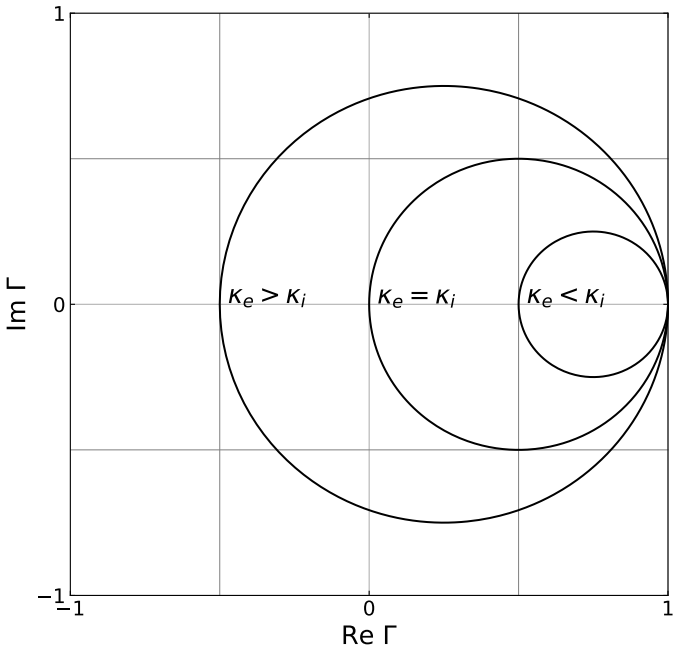

Figure 2.2: The reflection coefficient in the complex plane of a cavity with different couplings. In order of descending radius: overcoupled, criticaly coupled, and undercoupled. The point where the curve crosses the x-axis is when the frequency equals the resonance. Note that the overcoupled and undercoupled curves are identical in magnitude, but only their phase differs.

Note that this formulation is only relevant when studying a cavity in reflection geometry, as this is the only system that is studied in this thesis. If one would to explore a cavity in transmission geometry another such term would have to be added with its own external coupling constant [2]. As a last step we change to the rotating basis for the input probe $a \rightarrow ae^{-i\omega_p t}$ and introduce the detuning $\Delta = \omega_p - \omega$

$$\dot{a}_+ = \left(i\Delta - \frac{\kappa}{2}\right)a_+ + \sqrt{\kappa_e}s_+ \tag{2.17}$$

We calculate the steady state amplitude by setting $\dot{a}_+ = 0$ and solving for a_+.

$$a_+ = \frac{\sqrt{\kappa_e}}{\kappa/2 - i\Delta}s_+ \tag{2.18}$$

We can now use the standard input-output relation $s_- = s_+ - \sqrt{\kappa_e}a_+$ to derive a reflection coefficient

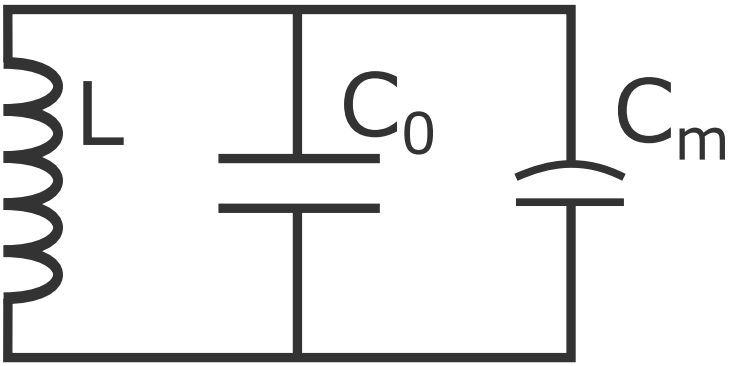

Figure 2.3: A mechanically compliant LC circuit. A traditional LC-circuit is formed by the inductance L and capacitance C_0, with the inclusion of a parallel capacitor C_m whose spacing can modulate.

$$\Gamma_r = \frac{s_-}{s_+} = 1 - \frac{\kappa_e}{\kappa/2 - i\Delta} = \frac{\kappa_i - \kappa_e - 2i\Delta}{\kappa_i + \kappa_e - 2i\Delta} \tag{2.19}$$

At resonance, the minimum value is $(\kappa_i - \kappa_e)/(\kappa_i + \kappa_e)$, so there is zero reflection at resonance only when the internal and external coupling constants are matched, a condition also known as *critically coupled*. When $\kappa_e > \kappa_i$ the cavity is called *overcoupled*, and when $\kappa_e < \kappa_i$ the cavity is called *undercoupled*. See Fig. 2.2 for a visual example. An undercoupled and overcoupled cavity can look the same in terms of magnitude, however, in an overcoupled cavity there will always be a 2π-phase flip when crossing through the resonance frequency.

2.1.3. OPTOMECHANICAL COUPLING

Now we can introduce the optomechanical coupling between a mechanical harmonic oscillator and the cavity input-output equations. Let's just recap by displaying the two equations, without any coupling between them.

$$\ddot{x} = -\Gamma_m \dot{x} - \Omega_m^2 x + \frac{F}{m} \tag{2.20}$$

$$\dot{a}_+ = \left(i\Delta - \frac{\kappa}{2}\right) a_+ + \sqrt{\kappa_e} s_+ \tag{2.21}$$

To couple these two differential equations we have to consider two effects in an optomechanical system; position-dependent cavity frequency, and radiation pressure [3]. A position dependent cavity frequency means that we can Taylor expand the cavity detuning $\Delta \to \Delta(x) \approx \Delta + \frac{d\omega}{dx} x$. For most cases it suffices to only keep the linear term. We also define the cavity pull parameter $G = \frac{d\omega}{dx}$.

We want to derive the cavity pull parameter, $G = \frac{d\omega_0}{dx}$, for a capacitively coupled optomechanical system, as shown in Fig. 2.3. Our model consists of a standard LC-circuit,

with an additional mechanically compliant capacitor C_m in parallel. We can calculate the resonance frequency as such

$$\omega_0(x) = \frac{1}{\sqrt{L(C_0 + C_\mathrm{m}(x))}} \tag{2.22}$$

We assume that the capacitor is a parallel plate and can thus be calculated as $C_\mathrm{m} = \epsilon A/x$, where ϵ is the permittivity, A is the plate area, and x is the spacing between the plates. We can now take the derivative of the previous equation

$$G = \frac{d\omega_0}{dC_\mathrm{m}}\frac{dC_\mathrm{m}}{dx} = \frac{\omega_0}{2}\frac{C_\mathrm{m}}{C_0 + C_\mathrm{m}}\frac{1}{x} \tag{2.23}$$

We can transform this variable into something more fundamental by using the zero point fluctuation of the membrane, defined as

$$x_\mathrm{zpf} = \sqrt{\frac{\hbar}{2\Omega_m m}} \tag{2.24}$$

and multiply it with G to get the single photon-coupling constant

$$g_0 = \frac{\omega_0}{2}\frac{C_\mathrm{m}}{C_0 + C_\mathrm{m}}\frac{x_\mathrm{zpf}}{x} \tag{2.25}$$

which is the amount the cavity's frequency changes when perturbed by the resonator's zero point fluctuations. The second fraction can be called the participation ratio of the mechanical capacitor and it is clear that the more this capacitance dominates, the larger the coupling. Furthermore, it is important to make the capacitive gap as small as possible. g_0 is often given as a figure of merit in optomechanical systems and a comprehensive overview of the current state-of-the-art is given in [4].

We can also use the cavity pull parameter G to determine an expression for the radiation pressure force $F = \hbar G|a_+|^2$. And thus we arrive at the coupled equations of motion for a basic optomechanical system.

$$\ddot{x} = -\Gamma_\mathrm{m}\dot{x} - \Omega_\mathrm{m}^2 x + \frac{\hbar G}{m}|a_+|^2 \tag{2.26}$$

$$\dot{a}_+ = i(\Delta + Gx)a_+ - \frac{\kappa}{2}a_+ + \sqrt{\kappa_\mathrm{e}}s_+ \tag{2.27}$$

We can further linearize these equations by assuming that both the mechanical and cavity can be split up into an average static amplitude and a fluctuating term; $a_+ = a = \bar{a} + \delta a$ and $x = \bar{x} + \delta x$. Note that we also drop the subscript for the cavity amplitude. We can first solve for the steady state solutions by setting the fluctuating terms to zero.

$$\bar{x} = \frac{\hbar G}{m\Omega_\mathrm{m}^2}|\bar{a}|^2 \tag{2.28}$$

$$\bar{a} = \frac{\sqrt{\kappa_\mathrm{e}}}{\kappa/2 - i\bar{\Delta}}s_+ \tag{2.29}$$

where $\bar{\Delta} = \Delta + G\bar{x}$. We can also solve for the fluctuating terms, and come to the following linearized coupled equations of motion. Note that we omit second order terms.

$$\delta\ddot{x} = -\Gamma_m \delta\dot{x} - \Omega_m^2 \delta x + \frac{\hbar G}{m}(\bar{a}^* \delta a + \bar{a}\delta a^*) \tag{2.30}$$

$$\delta\dot{a} = \left(i\bar{\Delta} - \frac{\kappa}{2}\right)\delta a + iG\bar{a}\delta x + \sqrt{\kappa_e}s_+ \tag{2.31}$$

where we assume that $\bar{a}$ is real. To solve this equation we use the ansatz

$$\delta a = \alpha_- e^{-i\Omega t} + \alpha_+ e^{+i\Omega t} \tag{2.32}$$

$$\delta a^* = \alpha_-^* e^{+i\Omega t} + \alpha_+^* e^{-i\Omega t} \tag{2.33}$$

$$\delta x = x_1 e^{-i\Omega t} + x_1^* e^{+i\Omega t} \tag{2.34}$$

and we keep only the terms resonant with the drive $\propto e^{-i\Omega t}$. We get three equations

$$x_1[\Omega_m^2 - \Omega^2 - i\Omega\Gamma_m] = \frac{\hbar G\bar{a}}{m}(\alpha_- + \alpha_+^*) \tag{2.35}$$

$$\alpha_-\left[\frac{\kappa}{2} - i(\bar{\Delta} + \Omega)\right] = iG\bar{a}x_1 + \sqrt{\kappa_e}s_+ \tag{2.36}$$

$$\alpha_+^*\left[\frac{\kappa}{2} + i(\bar{\Delta} - \Omega)\right] = -iG\bar{a}x_1 \tag{2.37}$$

Next, we remove α_+^* and x_1 from the first equation with the second and third and get for α_- the expression

$$\alpha_- = \frac{1 + if(\Omega)}{\kappa/2 - i(\bar{\Delta} + \Omega) + 2\bar{\Delta}f(\Omega)}\sqrt{\kappa_e}s_+ \tag{2.38}$$

with

$$f(\Omega) = \frac{\hbar G^2\bar{a}^2}{\kappa/2 + i(\bar{\Delta} - \Omega)}\chi_m(\Omega) \tag{2.39}$$

and the mechanical susceptibility

$$\chi_m(\Omega) = \frac{1}{m(\Omega_m^2 - \Omega^2 - i\Omega\Gamma_m)} \tag{2.40}$$

We can insert the solution into the input-output formalism $S_{11} = 1 - \sqrt{\kappa_e}\alpha_-/s_+$ to produce an equation for a reflection measurement. These expressions allow us to plot what happens when we do two-tone measurements – while one tone provides a strong constant drive, the other tone is scanned over the entire cavity linewidth. This gives rise to an effect called optomechanically induced transparency (OMIT) or optomechanically induced reflection (OMIR) [5, 6]. Since we mostly work in a reflection geometry cavity, the second term is the most relevant.

OMIR can be explained by the following scenario. We have a strong drive tone which is detuned from the center cavity by a mechanical linewidth $\Delta = \pm\Omega_m$ and we have a weak probe tone which scans near the center cavity. When the difference between the

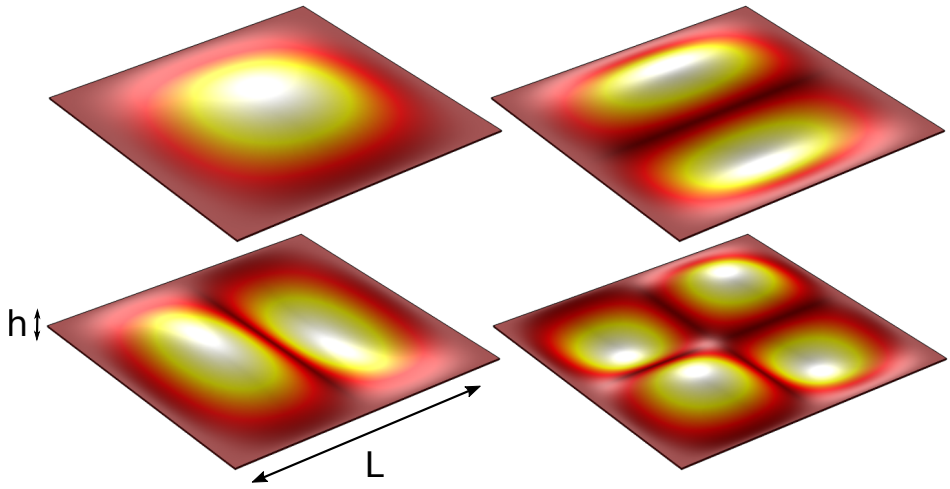

Figure 2.4: A visual representation of the first four modes of a membrane: from top-left to bottom-right (1,1), (1,2), (2,1), and (2,2). The color intensity shows the magnitude of the displacement.

probe and drive is exactly equal to the mechanical frequency, the beating between these two tones will drive the mechanical oscillator. The mechanical oscillator in turn will create sidebands of the strong drive which will interfere with the probe tone itself. This creates an interference effect which can create the appearance of a transparency window in the center of the cavity. The magnitude of the peak is dependent on the ratio of the mechanical frequency and the cavity linewidth, Ω_m/κ, the coupling constant $\eta = \kappa_e/\kappa$, amongst other parameters in a complex way. We discuss this effect in detail in chapter 6.

OMIR is also an easy method to measure what is called the multi-photon cooperativity

$$C = \frac{4g_0^2}{\kappa\Gamma_m} N \tag{2.41}$$

where N is the intracavity photon number. The cooperativity signifies the efficiency with which a mechanical oscillator can be cooled or amplified. The linewidth of an OMIT peak inside a cavity when in the side-band resolved limit and where the drive is detuned as $\Delta = -\Omega_m$, is given by $\Gamma_{OMIT} = \Gamma_m(C+1)$.

2.2. SILICON NITRIDE MEMBRANES

In this thesis the mechanical resonators take the form of a silicon nitride membrane. A membrane has a high aspect ratio – a typical example is a square membrane that is 1×1 mm wide and only 50 nm thick. A membrane is said to be under high tensile stress if its elongation energy (which is proportional to the initial film stress) is significantly larger than the bending energy. Silicon nitride membranes have been used for many optomechanical experiments, in both the optical and microwave domains [7–11]. Ex-

periments in the microwave domain do require the membrane to be coated with a conductive material, as we shall see in later chapters. The solutions for the mode structures of a square membrane can be seen in Fig. 2.4. The formula for the resonance frequency of a square membrane is given as follows

$$\omega_{jk} = \sqrt{\frac{\pi^2\sigma}{\rho L^2}}\sqrt{n^2+m^2} \tag{2.42}$$

where σ is the intrinsic tensile stress, ρ is the mass density of the resonator, and L is the lateral dimension of the membrane. n and m are integer mode indices, and can be related to the number of antinodes in the in-plane direction.

2.2.1. LOSS CHANNELS

Energy can be lost in a mechanical resonator in a few different ways. Energy can be lost by dissipation into a medium, such as gas, and energy can be lost by acoustic radiation into the substrate. Another loss mechanism is intrinsic to the material, and will be dissipated by friction into thermal energy. Gas dissipation is often irrelevant in optomechanical experiments because a high enough vacuum is easily attainable to put the loss dominance in another mechanism, such as radiation or friction [12]. Note that the acoustic radiation losses is also sometimes called clamping losses. We prefer radiation as a nomenclature because clamping can often be confused with bending losses, which is a type of friction.

RADIATION LOSSES

Acoustic radiation losses are caused by the propagation of elastic energy into the surrounding substrate. These losses are highly dependent on mode and substrate geometry and how these propagate. Conversely, temperature does not greatly affect this loss channel in the same way that the average kinetic energy of atoms does not significantly affect how a wave propagates and interferes through it. An intuitive reason how analytical models try to predict radiation losses of nanomechanical membranes is to calculate the degree of overlap between the membrane mode and the substrate modes [13, 14]. To make this derivation simpler, a half-space model is used where we assume that the membrane is connected at its edges to a bulk resonator which extends to infinity in one perpendicular direction of the membrane plane. This model is a good appromimation if one assumes that the relevant mode's wavelength is smaller than the dimensions of the substrate, but this is not always the case, especially for silicon nitride membranes with dimensions around millimeters. One can also see the issue of radiation losses as an acoustic impedance-matching problem [15].

A semi-infinite bulk resonator also creates a continuous spectrum of modes to propagate into. An introduction of boundary conditions will create a spectrum with more discrete modes and change the degree of overlap between the resonator and the bulk, and can be viewed as a mechanical analog of the Purcell effect. One also needs to take into account the interference of the propagating waves being emitted from the edges. The fundamental mode of a square membrane sets a force on the edges which are all in

phase with each other, and so a large net force is felt on the substrate. This causes the fundamental mode to often be limited by radiation losses [16–18]. On the other hand, higher modes with a high number of antinodes will emit waves with opposite phase which destructively interfere [19]. This mode dependence on radiative losses has also been observed in circular membranes [16, 20]. A model which predicts the radiation losses in a square membrane yields for large m, n the following asymptotic formula [21]

$$Q_{\text{rad}} \sim \frac{\rho_s}{\rho_r}\eta^3 \frac{n^2 m^2}{(n^2+m^2)^{3/2}} \frac{L}{h} \tag{2.43}$$

where ρ_s and ρ_r are the mass densities of the substrate and resonator, respectively. L and h are the side and thickness of the membrane. The phase velocity ratio between the substrate and resonator is given by

$$\eta \approx \sqrt{\frac{E_s}{\sigma}\frac{\rho_r}{\rho_s}} \tag{2.44}$$

where E_s is the substrate's Young's modulus, and σ is the intrinsic stress of the membrane. More precisely the above formula is valid when

$$\sqrt{m^2+n^2} \gg 0.3\eta \gg \sqrt{1+\frac{m^2}{n^2}} \tag{2.45}$$

Due to the difficulty of clamping the membrane to the chipholder in a consistent way [18, 22], radiation losses are often difficult to predict, which is why some research groups are moving towards integrating their membranes with phononic shields [11].

FRICTION

Internal friction is caused by irreversible processes during mode vibration and can involve, for example, movement of crystalline defects, and grain boundary slipping, or at low temperatures coupling to two-level fluctuators that are ubiquitous in an amorphous solid or can arise in a crystal due to disorder [12, 23]. This relaxation mechanism can be modelled using a standard linear solid model where the starting point is to understand that a solid will follow Hooke's law

$$\sigma(t) = E\epsilon(t) \tag{2.46}$$

where σ is the stress imparted onto the solid, ϵ is the induced strain, and E is the proportionality constant, the Young's modulus. During vibration of a mechanical mode, the strain will be oscillatory, and losses can be modeled by a phase delay between the stress and strain. We conclude that the Young's modulus is complex $E = E' + iE''$ where the real and imaginary components quantify the in-phase and out-of-phase components of the strain, respectively. Similar to dielectric losses, one can construct an elastic loss tangent as the ratio

$$Q_{\text{fr}} = \frac{1}{\tan\delta} = \frac{E'}{E''} \tag{2.47}$$

This equation is true for a bulk resonator, but geometrical modifications need to be included in the model for this to apply to membranes. In Ref. [17] a derivation is shown for square membranes with the following equation

$$Q_{\mathrm{fr}}(m,n) = \frac{E'}{E''}\left(\lambda + \lambda^2 \frac{(m^2+n^2)\pi^2}{4}\right)^{-1} \tag{2.48}$$

where m, n are the mode numbers and

$$\lambda = \sqrt{\frac{E'}{3\sigma(1-\nu^2)}\frac{h^2}{L^2}} \tag{2.49}$$

where σ is the internal stress, ν is the material's Poisson ratio, and h and L are the thickness and side length dimensions of the membrane, respectively. The equation Eq. (2.48) has two terms, the first term is related to the bending at the edges and the second to the bending in the bulk, which is why it scales with the mode numbers. We can see that the largest contribution to the losses comes from the bending at the edges and does not scale with frequency. For the validity of this equation we impose the limit $\lambda \ll 1$ [24]. We can also see that in this limit, it is advantageous to reduce this parameter as much as possible. This calculation also explains the trend that an increase in internal stress and/or increase in aspect ratio tends to increase the membrane's internal quality factor [23, 25].

TWO-LEVEL SYSTEMS

Certain losses can be modeled with a very general model called two-level systems, which can be seen as a form of friction, which is generally only relevant at low temperatures. The model was developed to describe losses that had a proportionality with temperature and could be measured to reach a plateau at low temperatures [26]. This model presumes that there are states within the solid that have two energy levels that are able to exchange energy. Fig. 2.5(a) shows two examples of two-level systems (TLS) which could exist in an amorphous solid – dangling bonds, or tunneling of atoms. There is an activation energy required which corresponds to the energy difference between the two states, ϵ, and is seen to be dependent on the geometrical constraints of the atomic bonds. Given the disordered nature of an amorphous solid, it is difficult to predict what this frequency might be, and is more likely a large distribution of frequencies.

Two regimes of TLS losses are interesting: resonant coupling, where the frequencies of the TLS and mechanical resonator roughly overlap ($\hbar\omega_{\mathrm{m}} \sim \epsilon(z)$), and the dispersive regime, where the TLS transition frequency is greater than the mechanical resonator ($\hbar\omega_{\mathrm{m}} \ll \epsilon(z)$). If there is resonant coupling, oscillations of the mechanical resonator will couple to the oscillations of the two level system and a phase delay between those oscillations would be observed as dissipation through the TLS's internal dissipation mechanisms. We want to focus on the dispersive case, however, as it is more relevant to our system.

The important element is that the spacing of the TLS is dependent on the displacement of the mechanical resonator, as seen in Fig. 2.5(b). An example of such a mechanism would be that the strain imparted on the amorphous solid could change the local

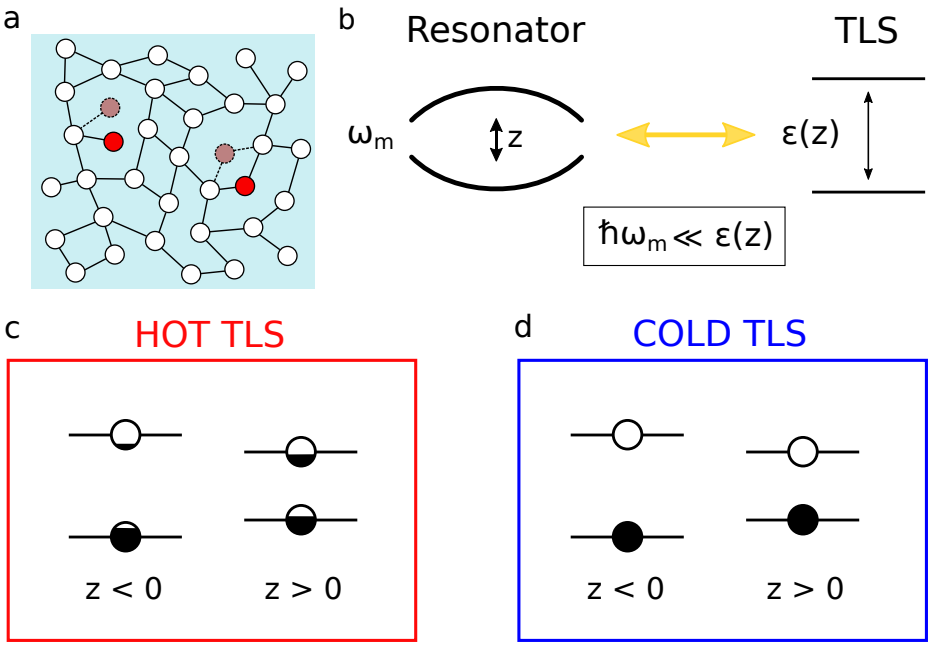

Figure 2.5: A description of how two-level system (TLS) losses work in the regime that the transition frequency of the TLS, $\epsilon/\hbar$, is greater than the frequency of the resonator, ω_m, i.e. $\hbar\omega_m \ll \epsilon$. (a) An example of what a disordered amorphous atomic network would look like and two defects which could lead to TLSs: dangling bonds, and atomic tunneling. (b) A schematic for dispersive TLS losses. The strain caused by the displacement of the resonator, z, causes a change in the geometry of the atomic bonds, thus coupling the transition energy $\epsilon(z)$ to the resonator frequency. (c)-(d) We look at what happens to the occupation of each state when the TLS's bath is hot or cold. We show the energy states where the spacing is at its largest at displacement $z < 0$ and vice versa. The coloring inside the circles show the average occupation of the state. (c) When the bath is hot, $\epsilon(z) \sim k_B T$, both energy levels will have a significant average occupation. (d) When the bath is cold, $\epsilon(z) \gg k_B T$, only the lowest energy states will be occupied, regardless of the resonator's displacement.

geometry of the bonds, and make it easier or more difficult for a dangling bond to switch states. Fig. 2.5(c)-(d) show schematics of average state occupation in a hot and cold bath. If we look at the situation where $\epsilon(z) \sim k_B T$, both levels will have roughly similar occupations. When the resonator changes displacement, the new energy levels will need to equilibrate with the bath at a rate which is equal to the loss rate of the TLS. If we go lower in temperature, one will reach a regime where the occupation of the bottom state is significantly higher than the upper level. The occupation will look there same regardless of the displacement of the mechanical resonator and there will be nothing to have to equilibrate with, thus minimizing losses. When TLSs are dispersively coupled, one is able to "freeze out" this loss channel.

This model is, however, very general and it can be very difficult to perfectly understand the nature behind these TLSs. In an amorphous solid there likely are a large

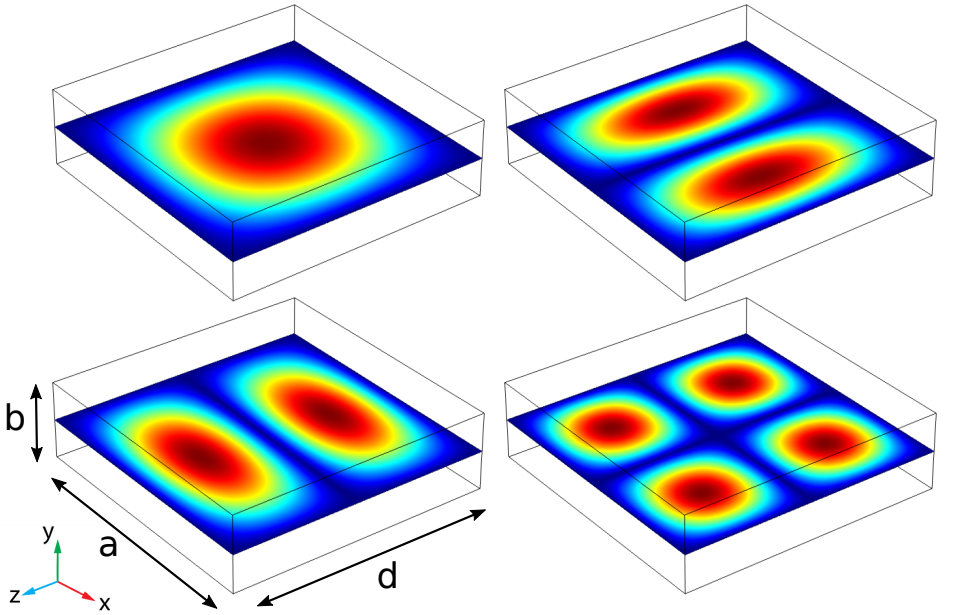

Figure 2.6: A visualization of the first four TE modes of a rectangular cavity (TE_{101}, TE_{201}, TE_{102}, TE_{202}). Note that a change in dimension b does not affect the resonance frequency. The color intensity shows the magnitude of the electric field.

number of these defects, each with their own frequency and coupling rates to the motion of the resonator. Note, that this model can also be applied to the oscillation of the electromagnetic mode, as long as this mode couples to the transition energy of certain TLSs [27].

2.3. 3D MICROWAVE CAVITIES

A 3D microwave cavity is a hollow conductive structure inside which there is an electromagnetic resonant mode. The walls form a boundary for the electric field propagating along direction d, as seen in Fig. 2.6, and the field energy is located mostly inside a vacuum. The most common shapes are cylindrical and rectangular, and we will focus solely on the rectangular kind. One can view such a cavity as a closed rectangular waveguide and this allows us to calculate the resonant frequencies by solving the Helmholtz wave equation. The result is as follows

$$\omega_{mnl} = \frac{c}{\sqrt{\mu_r \epsilon_r}} \sqrt{\left(\frac{m\pi}{a}\right)^2 + \left(\frac{n\pi}{b}\right)^2 + \left(\frac{l\pi}{d}\right)^2} \tag{2.50}$$

where m, n, l are the mode numbers, a, b, d are the cavity dimensions, and the constants c, μ_r, ϵ_r are the speed of light, the relative permeability, and the relative permittivity, respectively. Because there is only one conductor, transverse electromagnetic (TEM) modes – where neither the electric or magnetic fields are parallel to the direction of propagation – are not possible. Instead, transverse electric (TE) and transverse magnetic (TM) modes are excited. The fundamental mode is TE_{101} and for a $28 \times 28 \times 8$ mm cavity in vacuum would correspond to roughly 7.57 GHz. The fundamental mode can be approximated as an LC-circuit where the top and bottom plates are capacitor plates, and the sidewalls are conductors. A consequence of this is that the mode frequency is independent of the height of the top and bottom plates as the reduction in capacitance is counterweighted by an increase in inductance of the walls. This is true for any mode which does not have an antinode in the height direction, i.e. $n = 0$.

We can couple to this mode by introducing a small aperture through which we connect a coaxial cable. It has been noticed that the further the pin of the cable protrudes into the cavity, the greater the external coupling. This also has a tendency of distorting the mode shape a little bit.

It is worth comparing 3D cavities to their more compact 2D cousins, such as coplanar waveguide resonators. Superconducting 3D cavities have observed higher quality factors [28], because most of the mode energy is far removed from a lossy dielectric substrate. However, when introducing a device on a substrate into the cavity, you will still be affected by these losses, especially if you distort the mode so aggressively that most of the field is concentrated near the device. 3D cavities allow devices to be measured in a 'plug-and-play' method because of the simple procedure of placing the device inside the 3D cavity as opposed to having to integrate a measuring cavity as part of your 2D chip. This benefit of ease does go at a great cost of reduced consistency. For example, tuning the coupling to be the desired amount can be a difficult task as the device will introduce internal losses and distort the mode shape. The pin depth, on the other hand, will determine the external coupling and it becomes an art to try to balance these two interactions in a consistent way while trying to minimize the amount of cooling cycles your device must endure. This issue can be solved by building a variable coupling pin system [29].

2.3.1. LOSS CHANNELS

In an optomechanical system it is usually advantageous to reduce the losses of the cavity as much as possible. Losses come from three possible sources: conductive, dielectric, and radiative.

CONDUCTIVE LOSSES

Many metals, such as aluminium and niobium, become superconducting when their temperature is dropped below a certain transition temperature. The electrons inside the conductor pair up through a lattice vibration and become bosonic, known as Cooper pairs, effectively reducing resistance to zero. In practice, however, there will always be some finite surface resistance, R_s, which can be used to determine the quality factor as

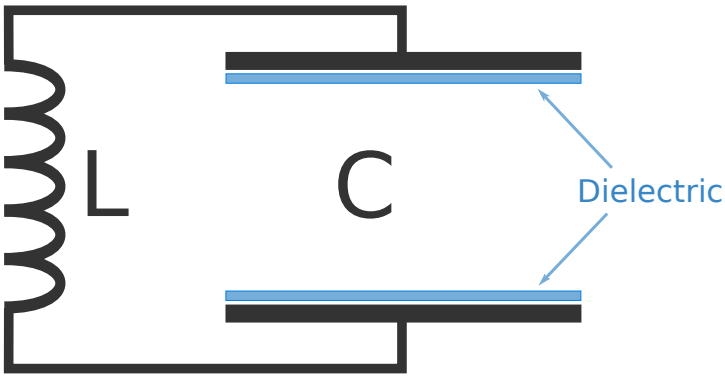

Figure 2.7: A circuit diagram of a 3D cavity with lossy dielectric on the surfaces.

limited by conductive losses [30]

$$Q_c = \frac{\omega\mu_0\delta_p}{R_s}\frac{\int_V |H|^2 dV}{\delta_p \int_S |H|^2 dA} \tag{2.51}$$

The first fraction is a standard quality factor which is calculated by dividing the reactive component – $X_s = \omega\mu_0\delta_p$ where the terms are the frequency, vacuum permeability, and penetration depth, respectively – by the resistive component. The second factor can be seen as the surface to volume ratio of the magnetic field.

An empirical formula for the ratio between superconducting and non-superconducting electrons provides an intuition into how resistive losses scale with temperature.

$$\frac{n_s}{n_n} \approx \left(\frac{T_c}{T}\right)^4 - 1 \tag{2.52}$$

where n_s and n_n give the electrons that are superconducting and non-superconducting, respectively. T is the bath temperature and T_c is the superconducting transition temperature of the metal. The term raised to the fourth power is advantageous and a typical setup with an aluminium cavity in a dilution refrigerator ($T = 15$ mK, $T_c = 1.2$ K) gives a ratio larger than 4×10^7.

DIELECTRIC LOSSES

The permittivity (also known as dielectric constant) of a medium is the proportionality constant between the electric displacement field and the electric field.

$$D(t) = \epsilon E(t) \tag{2.53}$$

The electric displacement field includes both charge migration and dipole polarization. For an oscillating electric field, there is the possibility of a phase delay in the polarization

of the dielectric's dipoles, similar to the friction loss tangent in bulk solids. The permittivity can then be expressed as a complex constant $\epsilon = \epsilon' - i\epsilon''$ from which one can define a loss tangent $\tan\delta_e = \epsilon''/\epsilon'$. If one assumes a uniform field (i.e. parallel plate capacitor) and a uniform distribution of dielectric, the conversion to a quality factor is easy. However, if one does not make this assumption one can include a participation ratio which accounts for this

$$Q_d = \frac{1}{p_e \tan\delta_e} \tag{2.54}$$

where

$$p_e = \frac{\int_d \epsilon |E|^2 dV}{\int_{tot} \epsilon |E|^2 dV} \tag{2.55}$$

where the numerator integrates over the dielectric and the denominator calculates the total electric energy in the resonator.

If we assume a simplified LC-circuit picture of a 3D rectangular resonator as seen in Fig. 2.7 then we can estimate a rough figure for Q_d. The dimensions of our 3D cavity is $28 \times 28 \times 8$ mm and we assume that there is a small 2 nm layer of aluminium oxide with a loss tangent $\tan\delta_e < 10^{-3}$ [31]. From this we calculate an upper bound on the quality factor of $Q_d \sim 2 \times 10^9$.

RADIATIVE LOSSES

Radiative losses are when energy is dissipated by waves escaping from the cavity. In order to create a 3D rectangular cavity which contained a chip, it was necessary to enable them to be opened by splitting the cavity in half. This could then be a source of dissipation. We observed that it was most advantageous to split the cavity along the direction that the current flows for the fundamental mode of the 3D rectangular cavity. Doing otherwise would cause the two halves to behave like a dipole antenna and increase radiation losses. One could also improve the quality factor by putting a small indium wire gasket in between the two halves. Indium is a malleable superconductor which can effectively seal the two halves. This has also shown to reduce what have been called "seam" losses [32].

REFERENCES

[1] B. H. Schneider, V. Singh, W. J. Venstra, H. B. Meerwaldt, and G. A. Steele, *Observation of decoherence in a carbon nanotube mechanical resonator,* Nature communications **5**, 5819 (2014).

[2] H. A. Haus, *Waves and fields in optoelectronics* (Prentice-Hall,, 1984).

[3] M. Aspelmeyer, T. J. Kippenberg, and F. Marquardt, *Cavity optomechanics,* Reviews of Modern Physics **86**, 1391 (2014).

[4] J. van Straalen, *Practical simulations of microwave devices from nanometer to centimeter scales* (Technical University of Delft, 2018).

[5] S. Weis, R. Rivière, S. Deléglise, E. Gavartin, O. Arcizet, A. Schliesser, and T. J. Kippenberg, *Optomechanically induced transparency,* Science **330**, 1520 (2010).

[6] A. Schliesser, S. Weis, S. Deléglise, R. Rivière, E. Gavartin, O. Arcizet, and T. Kippenberg, *Optomechanically induced transparency,* in *Lasers and Electro-Optics (CLEO), 2011 Conference on* (IEEE, 2011) pp. 1–2.

[7] B. Zwickl, W. Shanks, A. Jayich, C. Yang, A. Bleszynski Jayich, J. Thompson, and J. Harris, *High quality mechanical and optical properties of commercial silicon nitride membranes,* Applied Physics Letters **92**, 103125 (2008).

[8] R. W. Andrews, R. W. Peterson, T. P. Purdy, K. Cicak, R. W. Simmonds, C. A. Regal, and K. W. Lehnert, *Bidirectional and efficient conversion between microwave and optical light,* Nature Physics **10**, 321 (2014).

[9] M. Yuan, V. Singh, Y. M. Blanter, and G. A. Steele, *Large cooperativity and microkelvin cooling with a three-dimensional optomechanical cavity,* Nature communications **6** (2015).

[10] A. Noguchi, R. Yamazaki, M. Ataka, H. Fujita, Y. Tabuchi, T. Ishikawa, K. Usami, and Y. Nakamura, *Ground state cooling of a quantum electromechanical system with a silicon nitride membrane in a 3d loop-gap cavity,* New Journal of Physics **18**, 103036 (2016).

[11] Y. Tsaturyan, A. Barg, E. S. Polzik, and A. Schliesser, *Ultracoherent nanomechanical resonators via soft clamping and dissipation dilution,* Nature nanotechnology **12**, 776 (2017).

[12] S. Schmid, L. G. Villanueva, and M. L. Roukes, *Fundamentals of nanomechanical resonators* (Springer, 2016).

[13] I. Wilson-Rae, *Intrinsic dissipation in nanomechanical resonators due to phonon tunneling,* Physical Review B **77**, 245418 (2008).

[14] G. D. Cole, I. Wilson-Rae, K. Werbach, M. R. Vanner, and M. Aspelmeyer, *Phonon-tunnelling dissipation in mechanical resonators,* Nature communications **2**, 231 (2011).

[15] J. Rieger, A. Isacsson, M. J. Seitner, J. P. Kotthaus, and E. M. Weig, *Energy losses of nanomechanical resonators induced by atomic force microscopy-controlled mechanical impedance mismatching,* Nature communications **5**, 3345 (2014).

[16] I. Wilson-Rae, R. Barton, S. Verbridge, D. Southworth, B. Ilic, H. Craighead, and J. Parpia, *High-q nanomechanics via destructive interference of elastic waves,* Physical review letters **106**, 047205 (2011).

[17] P.-L. Yu, T. P. Purdy, and C. A. Regal, *Control of Material Damping in High-Q Membrane Microresonators,* Phys. Rev. Lett. **108**, 083603 (2012).

[18] S. Chakram, Y. Patil, L. Chang, and M. Vengalattore, *Dissipation in Ultrahigh Quality Factor SiN Membrane Resonators,* Phys. Rev. Lett. **112**, 127201 (2014).

[19] R. Zhang, C. Ti, M. I. Davanco, Y. Ren, V. Aksyuk, Y. Liu, and K. Srinivasan, *Integrated tuning fork nanocavity optomechanical transducers with high f mqm product and stress-engineered frequency tuning,* Applied Physics Letters **107**, 131110 (2015).

[20] V. Adiga, B. Ilic, R. Barton, I. Wilson-Rae, H. Craighead, and J. Parpia, *Modal dependence of dissipation in silicon nitride drum resonators,* Applied Physics Letters **99**, 253103 (2011).

[21] L. G. Villanueva and S. Schmid, *Evidence of surface loss as ubiquitous limiting damping mechanism in SiN micro-and nanomechanical resonators,* Physical review letters **113**, 227201 (2014).

[22] D. J. Wilson, *Cavity optomechanics with high-stress silicon nitride films* (California Institute of Technology, 2012).

[23] S. Schmid and C. Hierold, *Damping mechanisms of single-clamped and prestressed double-clamped resonant polymer microbeams,* Journal of Applied Physics **104**, 093516 (2008).

[24] A. Boisen, S. Dohn, S. S. Keller, S. Schmid, and M. Tenje, *Cantilever-like micromechanical sensors,* Reports on Progress in Physics **74**, 036101 (2011).

[25] S. S. Verbridge, J. M. Parpia, R. B. Reichenbach, L. M. Bellan, and H. G. Craighead, *High quality factor resonance at room temperature with nanostrings under high tensile stress,* J. Appl. Phys. **99**, 124304 (2006).

[26] S. Hunklinger, W. Arnold, R. Nava, K. Dransfeld, *et al., Saturation of the ultrasonic absorption in vitreous silica at low temperatures,* Physics letters A **42**, 253 (1972).

[27] C. Müller, J. H. Cole, and J. Lisenfeld, *Towards understanding two-level-systems in amorphous solids-insights from quantum devices,* arXiv preprint arXiv:1705.01108 (2017).

[28] M. Reagor, H. Paik, G. Catelani, L. Sun, C. Axline, E. Holland, I. M. Pop, N. A. Masluk, T. Brecht, L. Frunzio, *et al.*, *Reaching 10 ms single photon lifetimes for superconducting aluminum cavities,* Applied Physics Letters **102**, 192604 (2013).

[29] A. P. Sears, *Extending Coherence in Superconducting Qubits: from microseconds to milliseconds* (Yale University, 2013).

[30] D. M. Pozar, *Microwave engineering* (John Wiley & Sons, 2009).

[31] J. Zmuidzinas, *Superconducting microresonators: Physics and applications,* Annu. Rev. Condens. Matter Phys. **3**, 169 (2012).

[32] M. Reagor, W. Pfaff, C. Axline, R. W. Heeres, N. Ofek, K. Sliwa, E. Holland, C. Wang, J. Blumoff, K. Chou, *et al.*, *Quantum memory with millisecond coherence in circuit qed,* Physical Review B **94**, 014506 (2016).

3

DEVICE FABRICATION AND MEASUREMENT SETUP

This chapter gives an overview of the fabrication methods that were employed in the subsequent chapters of this thesis. We start with the fabrication methods for the silicon nitride membranes. Three different methods for metalizing commercial Norcada membranes are discussed. We move to the fabrication of tethered trampoline membranes and its own metalization process. The processing and construction of 3D cavities is discussed, and our measurements of their quality factors are presented. A brief description of the fabrication of our antenna chips is given, and we then dedicate some effort to explain our flip-chip method: variations on the method, and the difficulties inherent in each. We conclude this chapter by giving an overview of our cryogenic measurement apparatus.

3.1. OVERVIEW

The device that is used in this thesis consists of three parts: a 3D microwave cavity, an antenna chip, and a metalized membrane. These parts would be fabricated, or machined, independently, and only would be assembled together at the last part using a technique called flip-chip. The 3D cavity was machined from aluminium or copper or niobium by the machine shop at the university but would be post-processed using different techniques inside our cleanroom. The antenna chip would always be fabricated from scratch in the cleanroom, and the membrane chip would either be made in-house or store-bought (with some additional modifications) depending on the experiment. We start by discussing the fabrication of the membrane chip in two separate ways: the commercial Norcada membranes and the trampoline geometry membranes.

3.2. METALIZATION OF NORCADA MEMBRANES

Norcada manufactures high-stress silicon nitride membranes which were originally designed for use as transmission electron microscopy windows. However, they have been praised for their high mechanical quality factors for use in optomechanical experiments [1]. The windows are fabricated on a lightly-doped silicon substrate which is subsequently put inside a low-pressure chemical vapour deposition (LPCVD) oven to grow a 50 nm stoichiometric Si_3N_4 layer over it. On the backside a square window is etched to serve as a hard wet-etch mask for a solution of potassium hydroxide (KOH). It is then put inside KOH for a few hours until there is a 1×1 mm sized silicon nitride membrane. The fact that the LPCVD process is done with stoichiometric concentrations of silicon and nitride precursors allows the film to achieve the highest tensile stress as possible. A contributing factor to the tensile stress is the difference in thermal expansion coefficients between silicon ($\alpha = 2.56 \times 10^{-6}$ K^{-1} [2]) and silicon nitride ($\alpha = 3.27 \times 10^{-6}$ K^{-1} [3]) – since the silicon substrate shrinks less than the silicon nitride, the membrane layer is effectively 'stretched' over the substrate. High tensile stress is known to create high-quality factor membranes since it increases the stored energy without affecting the overall energy loss [4].

In order to increase coupling to the cavity, we coat the membrane with a thin metal superconducting layer. For this we choose either aluminium or an alloy of Molybdenum-Rhenium 60-40 (MoRe) [5] depending on which temperature we intend to perform the experiment in. Aluminium has a superconducting transition temperature at $T_c \sim 1.1$ K while MoRe has $T_c \sim 10$ K which would allow the experiment to be performed at liquid helium temperatures. The thickness of our superconducting layer would be around 20 nm. We observed that when we deposited thinner layers of aluminium the cavity would saturate at lower input powers, presumably due to the lower critical current of the film. The metal film would be deposited such that it would only be covering the mechanical element with a window of 0.9×0.9 mm such that it does not overlap with the silicon substrate frame. This is important to minimize mechanical losses [6]. However, when we purposely wanted to lower the mechanical quality factor, we would deposit a window which would cover the frame as well.

You could categorize our fabrication methods into two different types: additive fab-

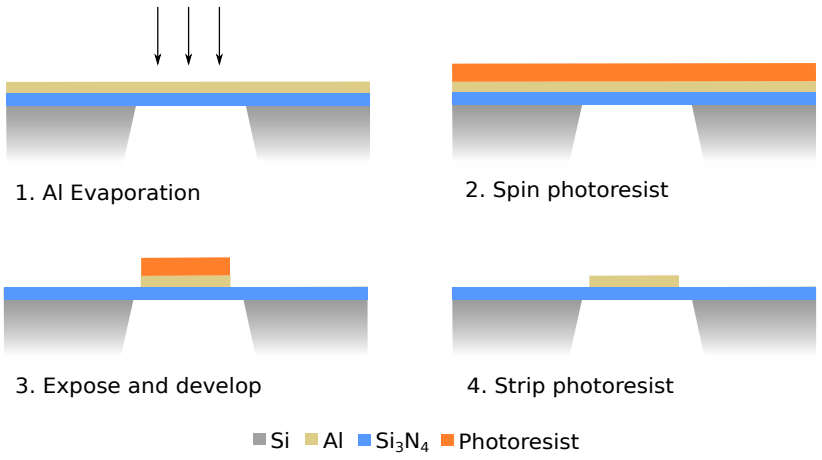

Figure 3.1: Fabrication steps when metalizing a norcada membrane subtractively.

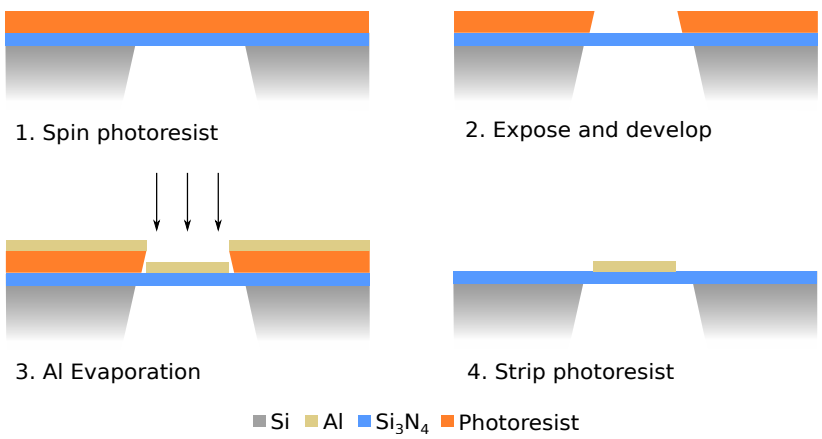

Figure 3.2: Fabrication steps when metalizing a norcada membrane additively with lift-off.

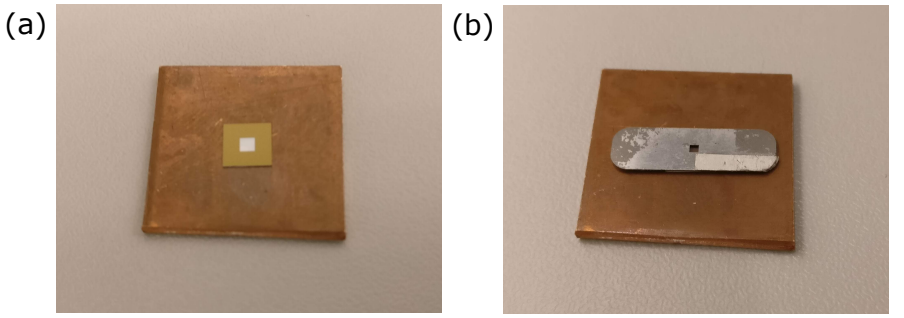

Figure 3.3: (a) We first stick the Norcada membrane onto a copper block using a thin layer of PMMA. (b) Using small carbon tape 'pillars' as spacers, we stick a shadow mask onto the copper block.

rication and subtractive fabrication. The additive method was done by using a physical shadow mask through which we would evaporate a metal layer, or with lift-off technique. The subtractive method was performed by first depositing an entire metal layer, and then using photoresist to etch away a little square in the center.

3.2.1. SHADOW MASK EVAPORATION WITH STENCIL

The shadow mask method consisted of overlaying a small metal sheet with a square hole in it and letting a metal evaporate through it, thus adopting the pattern. It is important to note that this method was not feasible with sputtering, as the mean-free path of a sputtered film is too short, and the contours of the pattern would be blurred. We would have these masks fabricated by Eurocircuits which are intended as stencil masks for integrated circuits. The trick is that to get the alignment perfect, it requires a steady hand and patience. The first step of this process was to fix the membrane onto a copper block such that you could handle it a lot better and onto which you would fix the shadow mask as seen in Fig. 3.3(a). The copper block would be roughly 3×3 cm large. We would first put a small drop of Poly(methyl methylacrylate) (PMMA) onto the copper block and spin it for 35 seconds on 1000 RPM. This would give it a very thin, sticky layer of PMMA which we use as glue to fix the membrane. After we gently put the membrane on the drop of PMMA, we heat it on a hotplate for a minute to let it dry. This timing had to be done right because if you used too wet PMMA, some of it would evaporate onto the bottom of the membrane, or would bulge it due to trapping gases.

In our first shadow mask version, we would place two small bits of carbon tape on the sides of the shadow mask to act as a spacer between the mask and fragile silicon nitride membrane. This method was feasible when the dimensions were not smaller than 0.3 mm. When we tried to align smaller features, we developed a small clamping system which would give us better control over the position of the mask and membrane. Fig. 3.3(b) shows a Norcada membrane with a stencil mask on top it.

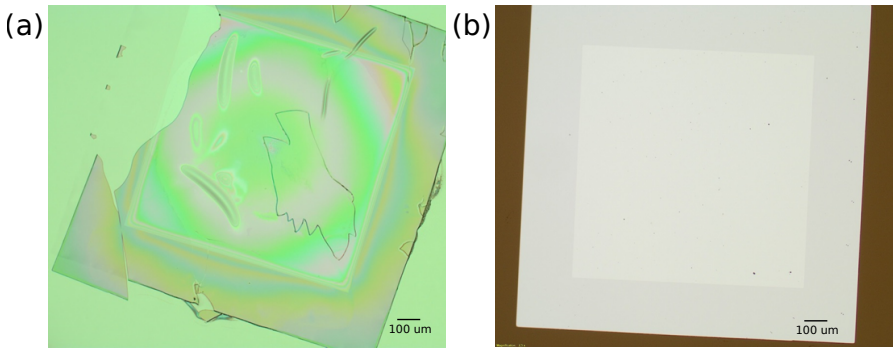

Figure 3.4: (a) An optical micrograph which shows a failed patch of photoresist that is deposited onto the Norcada membrane. What you see is photoresist which has cracked after the development stage. (b) A successful membrane chip which was fabricated using lift-off.

3.2.2. PATTERNING ELECTRODES BY ETCHING

Using the subtractive method we first evaporate or sputter a metal layer onto the entire membrane, and then use a photoresist to etch away the square patch. To be able to spin photoresist onto the 5 × 5 mm membrane chip, we again have to fasten it to a copper block. For this we use the exact same method as described above. The reason for this is that the suction cup on the spinner would otherwise implode the membrane. Once the membrane is fastened, we put a small drop of Microchemicals AZ ECI 3007 photoresist and spin it for a minute at 4000 RPM which we follow with a minute bake on the hotplate at 90° C. We then pattern the square patch using a Durham Magneto Optics Microwriter ML-2 laserwriter. When we use aluminium as the mask, the developer, Microposit MF-321, also etches aluminium, so by leaving it in the solution for a little longer (roughly 3 minutes) it takes care of both steps. The last step is to rinse off the photoresist using N-methyl-2-pyrrolidone (NMP) at 80° C for 10 minutes. This etching technique was the preferred method to get a well-aligned metal patch, however, it would only be suitable for membranes which were squarely shaped (i.e. Norcada membranes). The trampoline chips we shall see later would not allow photoresist to be spun on them without breaking. The downside was that because the chip was so small, edge beads would often form at the corners which would mean that there would be small metal dots on the corners. We found that the best method to get rid of these was to use a 'hybrid' approach between subtractive and shadow mask. We would have a large metal frame which would cover the edges when we evaporated the metal, and so there would be no underlying metal under the edge beads.

3.2.3. PATTERNING ELECTRODES WITH LIFT-OFF

We found that when we wanted to fabricate a metal patch onto the membrane that overlapped with the frame – so as to induce more mechanical losses – using the subtractive method above, it always failed. We would copy the method above, and pattern an over-

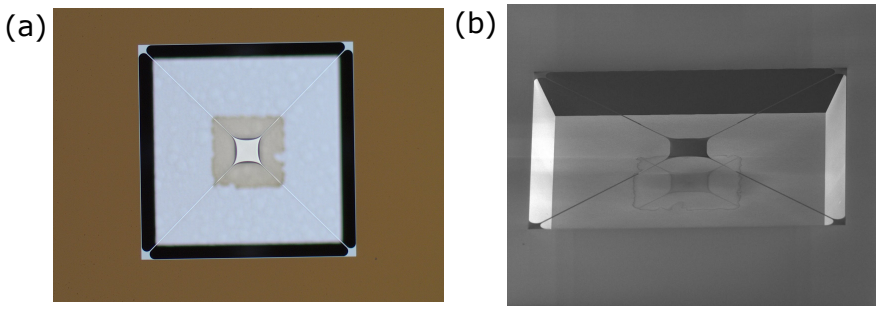

Figure 3.5: (a) An optical micrograph of a metalized trampoline, using the shadow mask method. (b) A SEM image of the same trampoline chip.

lapping square in the laserwriter, but when we developed it, the photoresist would lose adhesion and peel off as seen in Fig. 3.4. So for these chips we resorted to a lift-off technique. We would instead use Microchem AZ 5214E negative photoresist such that we would obtain a large undercut which would make it easier to lift-off MoRe. MoRe was also sputtered using an AJA system which meant it covered side walls a lot better, undermining the effectiveness of the lift-off techhnique. After sputtering a layer of 20 nm, we put the sample in NMP at 80° C for 20 minutes.

3.3. FABRICATION OF TETHERED TRAMPOLINE MEMBRANES

Another membrane geometry that we explored were what we called trampolines. These geometries were first pioneered in the group of Simon Groeblacher [7] and Jack Sankey [8]. These membranes consist of a small square patch which is suspended by four tethers emanating from its corners, and attached to a silicon frame. The shape of the structure causes the stress inside the tethers to approach the ultimate yield strength of silicon nitride. These trampolines have been shown to produce quality factors of 10^8 at room temperature and high vacuum. The method behind their fabrication is as follows.

We start with a silicon substrate on which we grow stoichiometric silicon nitride using LPCVD. We usually had a thickness of 30 nm. Then we spin electron-beam resist, Allresist AR-P 6300-13 and spin at 4000 RPM to get a resist of roughly 350 nm. We write the pattern using a 92 nm electron-beam spot size and then develop using pentyl acetate for 60 seconds. We etch away the spaces negative to the tethered membrane with a CHF_3 reactive ion etch. We descum the chip in situ with a small oxygen plasma. We then perform a thorough clean of the chip in a Piranha solution. This piranha solution is prepared by mixing a (3:1) solution of sulfuric acid to hydrogen peroxide. We first heat the sulfuric acid to 80° C and then add the hydrogen peroxide and put in the sample until the solution stops bubbling. Piranha solution is known for very thoroughly cleaning off any organics. The last step requires us to etch away the sacrificial silicon layer. This is done by heating a solution of 30% KOH to 70° C for 100 minutes. Afterwards we rinse in water 3 times and put it in 99% pure isopropyl alcohol (IPA) 2 times. We then put it into

a Leica CPD3 critical point dryer which ensures that capillary forces do not destroy the trampoline.

3.3.1. METALIZATION OF TRAMPOLINE DEVICES

The issue of metalization is difficult with trampolines as the geometry does not allow one to pattern on it when it is already released. Furthermore, the high pH etchants of silicon, which are used in the last step, etch away aluminium very quickly. We tested a few other superconductors and found that both KOH and Tetramethylammonium hydroxide (TMAH) etch away MoRe, titanium, and NbTiN alloy too quickly to allow an undercut to be etched in the silicon. There are mentions in literature where a solution of TMAH is made which is saturated with powdered silicon, and thus shifts the equilibrium in such a way that the aluminium etch rate is reduced significantly [9, 10].

The process starts in the same way as the bare trampolines as mentioned above, but diverges after the cleaning with Piranha solution. After this step a layer of 20 nm of aluminium is evaporated. After this a layer of AZ ECI 3007 photoresist is spun and a small metal patch is patterned using the laser writer. The patch is etched with MF321, which is also the developer for the photoresist. The photoresist is stripped using a 80° C solution of NMP. We create the silicon etchant by first dissolving 10 g of TMAH into 100 mL of water. The solution is heated to 80° C to allow the dissolution of powdered silicon to go as fast as possible. We obtain 3.2 g of 99.999% purity silicon powder and dissolve it, slowly, to the heated TMAH solution. It is important to not do this too fast as the solution runs the risk of boiling over, reducing the accuracy to which you know the TMAH solution. Lastly, we add 1.3 g of ammonium persulfate because it has been shown to produce smoother silicon surfaces [10]. We try to keep a funnel on the top of the beaker as much as possible such that any evaporated water eventually condenses back into the solution and the hole in the funnel is used to protrude a thermometer. Also, we keep the solution stirring vigorously using a magnetic stirrer. Once all reactants have been sufficiently dissolved, we insert the holder with the trampoline chips and wait 120 minutes. As a last step we repeat the process mentioned above, making sure the trampolines are rinsed thoroughly with water and IPA before going into the critical point dryer.

We found that it was very difficult to get the etch rate to stay consistent whenever preparing the solution. The reactant is notorious for being very sensitive to how it is prepared, and the etch rate seemed to fluctuate wildly. We also tried an alternative: metalization at the last step, using a shadow mask. The smaller size of the trampolines meant that is would require a more robust way of aligning the shadow mask, which we solved by using a clamping shadow mask holder. This proved to be the winning method for producing metalized trampolines. A downside to this technique, however, is that the metal would inevitably encompass a larger area, and thus be deposited partially on the tethers as seen in Fig. 3.5. Anecdotal evidence from colleagues suggest that any deposition of the tethers would negatively affect the quality factor. Also, we noticed that the stress gradient of the deposited metal would curve the straight sides of the center patch upwards, where the tensile stress of the silicon nitride trampoline is the weakest. We discovered in the end that for our goal to measure the quality factor of these trampolines in an op-

tomechanical system, the coupling was sufficient without any metalization as silicon nitride can serve as an oscillating dielectric of a capacitor instead of being itself an oscillating capacitor. However, the smaller the capacitive gap was, the more the difference between oscillating capacitor and oscillating dielectric diverged, and it became obvious that metalization was still necessary to gain significantly in optomechanical coupling.

3.4. ANTENNA CHIP FABRICATION

For our antenna chip we had a choice of different substrates. We chose either high resistivity silicon or double sided polished sapphire. Silicon had the advantage that it could be etched, while double side polished sapphire has a very low microwave loss tangent [11] ($\tan\delta \sim 10^{-8}$) and was see-through. We shall see in the flip-chip section why that was important. We would dice the wafer into 9×9 mm chips because this fit well with the 3D cavity design. We would clean substrates using a Piranha mixture to thoroughly remove any organics left over from the dicing. For the antenna chip we would not use additive fabrication. The easiest method was to evaporate aluminium onto the substrate and then spin photoresist AZ ECI 3007 onto it. We pattern the antennas using a laserwriter, and are able to etch away the aluminium with the photoresist developer. If we used MoRe as the superconductor we would then etch it away using a reactive ion etch plasma, as described above. The photoresist would be cleaned off using NMP.

3.5. 3D CAVITY PROCESSING

We experimented with various purities of aluminium, copper, and niobium. Aluminium is the standard in 3D cavity quantum electrodyamics literature [12–14] because it is a cheap superconductor with a transition temperature at 1.1 K, which is easily attainable inside a dilution refrigerator. Aluminium is also very easily machined because of its malleability. Niobium, or an alloy of it, on the other hand, is more common in the particle accelerator community because of an easily attainable transition temperature above the boiling point of helium. The accelerator community also has decades of experience in perfecting the loss rate of their cavities using annealing, seam control, and cleaning methods [15]. In our case, however, niobium cavities provided a quicker way to test devices by only having to thermalize to a dewar of liquid helium. Copper was used whenever there was no necessity in minimizing cavity losses.

Our 3D cavities were machined by our technicians using a computer numerical control (CNC) machine. The outer dimensions of the cavities were $36 \times 36 \times 24$ mm and the inner dimension was either $28 \times 28 \times 8$ mm or $24 \times 24 \times 8$ mm which would correspond to a fundamental frequency of 7.6 GHz and 8.9 GHz, respectively. We would first clean off organic residues by putting the cavity halves into a warm bath of acetone and sonicate it for 20 minutes after which we would dry it using IPA and a nitrogen blower. A goal of ours was to maximize our cavity photon lifetime by as much as possible. We found the biggest increase in aluminium cavities by increasing the purity of the metal. In some cases it would increase the quality factor by an order of magnitude. The first two entries of table 3.1 show an example of such a jump. It has also been documented in literature

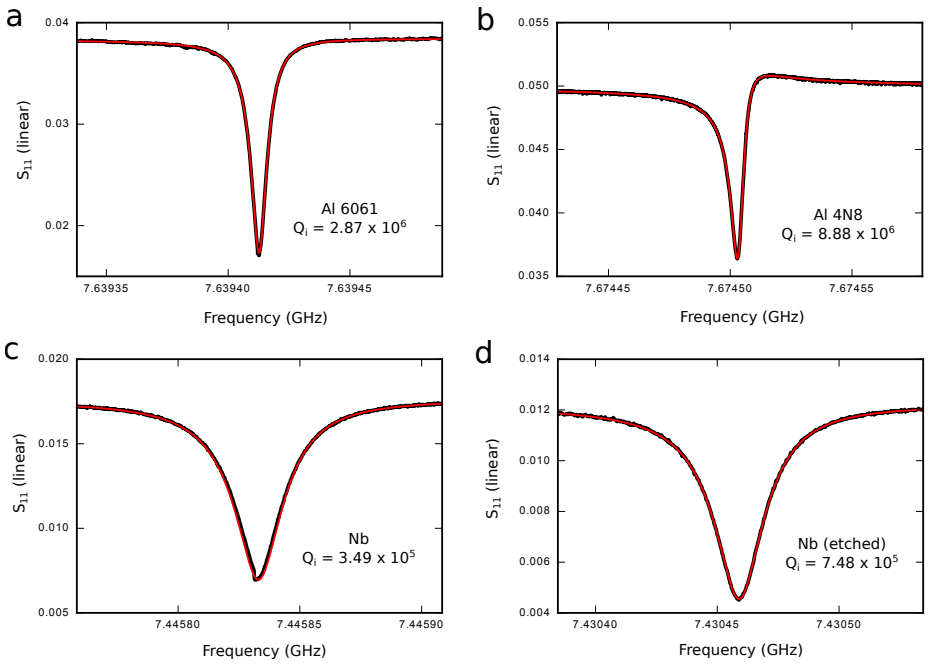

Figure 3.6: Reflection coefficients measurements for four different 3D cavities, black line is the raw data and the red line is a lorentzian fit. (a) 6061 aluminium alloy, (b) 4N8 (99.998%) purity aluminium, (c) unetched niobium, (d) etched niobium. The aluminium cavities were measured at 16 mK, and the niobium cavities were measured at 4.2 K. A summary of the fitted data can be found in table 3.1

that etching of the aluminium will increase the quality factor, however we were never able to mimick the results of other groups. Due to the scarcity of the material and duration of machining, we were also not able to create a systematic study.

We tried an etchant recipe which dissolves niobium oxides [16]. A solution made up of 40% HF, 70% HNO_3, 85% H_3PO_4 in a (1:1:2) volume ratio was created and the cavities were placed inside it for 60 minutes. After removal we rinse it in deionized (DI) water for 10 minutes. As can be seen in the last two entries of table 3.1, the increase in Q was minimal, which we attribute to a very uneven etch which introduced sharp edges.

Cavity	f_0 (GHz)	T (K)	Q_i	Q_e
Al 6061	7.639	0.016	2.87×10^6	1.08×10^6
Al 4N8	7.675	0.016	8.88×10^6	1.28×10^6
Nb	7.446	4.2	3.49×10^5	8.06×10^5
Nb (etched)	7.430	4.2	7.48×10^5	3.40×10^5

Table 3.1: Table of Q-factors of different 3D cavities in our lab.

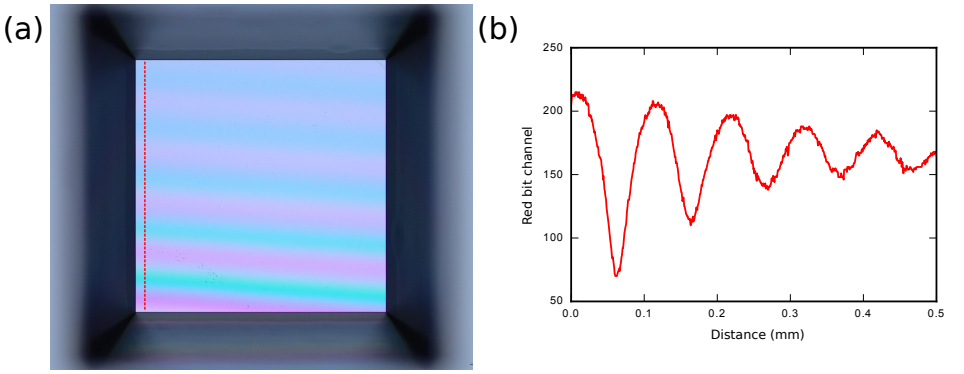

Figure 3.7: (a) A flipped chip without metalization which shows the Newton rings as a qualitative measure of the distance between the chips. (b) A vertical linecut is taken from image in (a) and the red channel is plotted over distance.

3.6. FLIP-CHIP ASSEMBLY TECHNIQUES

The most difficult process of the assembly was the 'flip-chip' method where you would have to fix the membrane chip and antenna chip using a drop of glue. The important part was that to get the coupling as large as possible you would have to get the capacitive gap as small as possible. Also, when aligning trampolines with significantly smaller areas, it required better fine-tuning when aligning the antenna chip with the membranes. In the beginning we would use a probe station and modify it to perform the flip-chip procedure. We developed another method which used a photolithography mask-aligner to obtain better ability to align, and also to be able to push the gap between the chips. We measured the gap size by putting the flip-chip assembly onto the microscope and use a magnification of 100x. By focusing on the bottom and chip and on the top chip we could notice the difference in the notches moved in the focusing dial of the microscope. Another visual clue for the gap size was also that whenever the gap was below a micron, Newton rings became very prominent. This also allowed us to easily see a gradient and determine whether the membrane was slightly tilted (it usually was, which makes sense seeing as we would always use only one drop of glue on the corner). Fig. 3.7 shows an example of what this interference pattern looks like. We take a linecut and plot the red channel over distance. Constructive interference happens when there is a gap distance which is an odd integer multiple of half the wavelength. Using the wavelength of spectral red, 647 nm, we estimate that the gap goes from 320 nm to 3.4μm.

3.6.1. PROBE STATION METHOD

Probe stations have a central platform, on which you can connect different needles and measure conductances. To facilitate the process on smaller chips, there is a microscope attached through which you can fine-tune the needle positions. The needles are fastened onto the station using suction cups which are connected to a vacuum pump. We

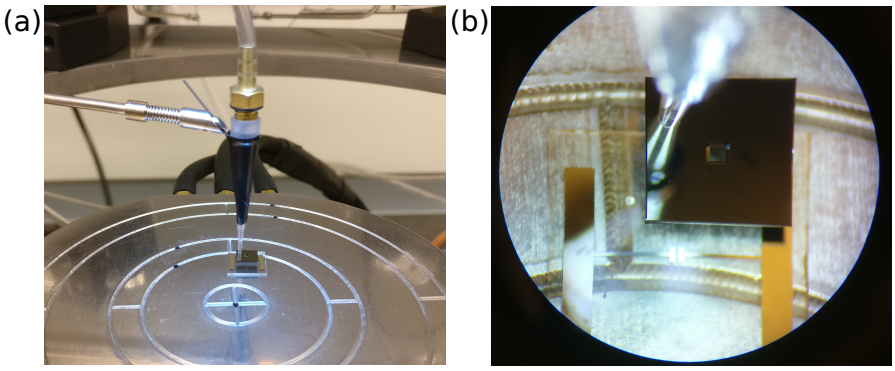

Figure 3.8: (a) A photo of the flip-chip setup on the probe station, showing the suction cup holding a 1 × 1 mm Norcada membrane chip and the antenna chip underneath. (b) A look through the viewfinder.

took one of these vacuum lines and fixed it to a small pipette tip. This we then fixed onto a holder of one of the needles because it has an easy interface to manipulate the position of the pipette.

First we put an antenna chip in the middle of the platform facing up. Then we stick a metalized membrane, facing down, onto the suction cup such that it is only holding on by the far corner of the membrane chip. It is important to make sure that the membrane is being held such that it is perfectly parallel to the surface of the antenna, otherwise when you release the vacuum, the membrane often shifts a little, misaligning it. A tiny drop of epoxy glue is put onto the corner of the antenna chip on the same spot where the suction cup is located. The drop of glue has to be small enough such that it does not spill into the membrane area when you press onto it with the probe station suction cup as this will break it. Furthermore, the less gluing there is, the higher the mechanical Q factor will be [17]. We carefully lower the membrane onto the antenna chip and push the membrane down as much as possible. This may lead to some shifting of the alignment, so this was done with caution. The result of this was that we could obtain gaps around 3 micron.

3.6.2. MASK ALIGNER METHOD

We opted for a mask aligner to flip our membranes for two reasons: alignment was better controlled, and we could push the membrane harder. The system that we used was Karl Suss MJB-3. While it was possible to align the norcada membranes properly using the previously mentioned system, when we started to work on trampolines which were around tenfold smaller in size, we really needed a better alignment method. Furthermore, the trampolines did not have a window through which we could see, which would mean that we would have to use a see-through sapphire substrate for the antennas and look through it to align the chips.

Since the machine is originally used as a mask aligner, the holders are designed for

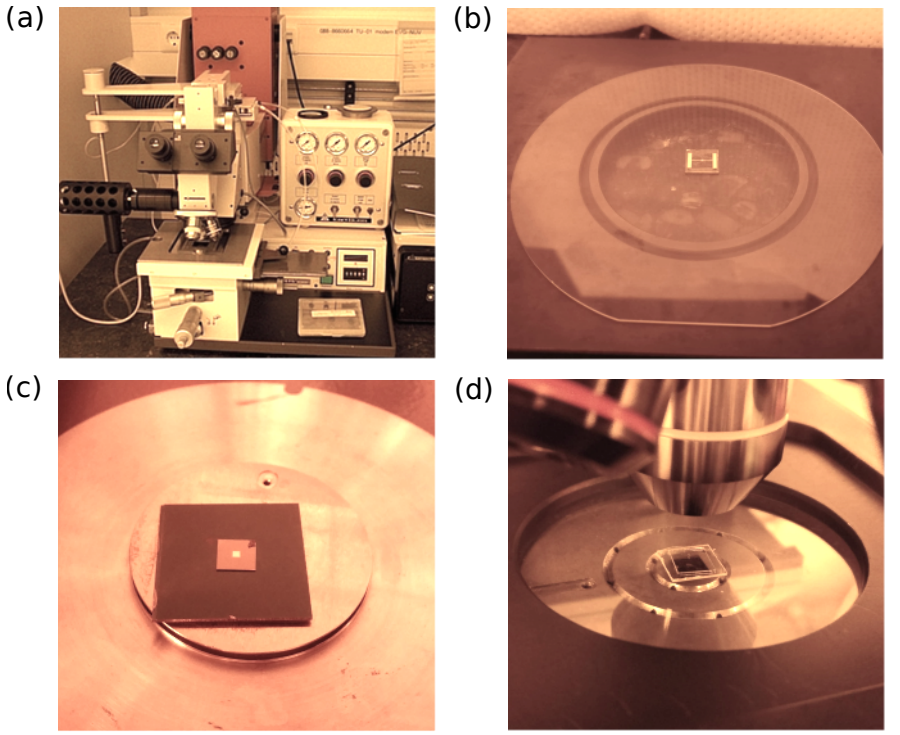

Figure 3.9: (a) A photo of the MJB-3 mask aligner system. (b) We start by putting a double-sided polished sapphire wafer on the top suction plate and stick an antenna chip on it using a bit of tape. This is then mounted into the MJB-3 such that the antenna is facing downwards. (c) We put a small drop of epoxy glue onto the membrane chip and lay it on the bottom plate. (d) The last step is to look through the viewfinder and try to align the two chips using the given manual controls. Once the alignment is satisfactory, the bottom part is pushed up.

4 inch wafers. So we would stick the double side polished (DSP) sapphire antenna chip onto another DSP sapphire 4 inch wafer and fix it to the top part of the mask aligner. On the bottom we would place the membrane or trampoline chip and use the knobs to carefully tune the position. Once the alignment was satisfactory, we would again put a drop of glue on the corner of the membrane chip and raise it until it touches the antenna chip. The advantage of this method is that we would be able to observe the drop of glue touching and expanding when sticking to the above chip. It was crucial to put as small a drop as possible, because otherwise the viscosity of the glue would prevent the gap from going below a micron. We could also push the gap with a more evenly distributed force and so there was a smaller chance that two chips would misalign significantly. Still, even with the ability to push as much as we could, it was still very difficult to get the gap to below a micron.

3.6.3. FLIP-CHIP FRAGILITY ISSUES

We observed many difficulties when trying to perfect the flip-chip method using the mask aligner. What we started noticing is that the membranes were incredibly fragile, and would break often, *after the flip was performed*. Sometimes it would take a few seconds, and sometimes it would take a few days before it would break. Importantly, the membrane would not always break due to some kind of shock (i.e. opening the lid, picking up the membrane), although sometimes it would. The inconsistent nature of the destruction of the flipped chip made it difficult to create a robust statistical analysis of the causes for breaking.

Here is a comprehensive list of all the variables we tested, but came out inconclusive:

- **Stress of the metal.** We reasoned that perhaps a metal that was deposited with a high level of stress could increase the tensile stress of the membrane and make it more prone to fracturing. This was corroborated by the fact that a membrane without any metal would not break. We tested it will aluminium that was evaporated on a cooled substrate, and with evaporated titanium (both would have higher tensile stress than room temperature evaporated aluminium) but they would still break.

- **Glue type.** We tested both vacuum grease and bison store-bough epoxy and did not find that either made the membranes break more than the other.

- **Drying times of epoxy.** We though that perhaps the glue would take a long time to dry, and would slide a little after taking it off the mask aligner, thus breaking the membrane. Yet even if we let the chip sit and dry for a whole day, it would still be observed to break every now and then.

- **Delicacy of handling.** There was no pattern related to the severity of handling of the chip. Sometimes the chip would break while transferring the chip off the sapphire holder, but sometimes it would break while resting over a few days. We also tested dropping the holder, and could not get it to reliably break. Sometimes putting on the lid violently would make it break, but again, this was not easily reproducible.

Figure 3.10: A visual demonstration of the fragility of the flip-chip method. This is a sample of the 40 Norcada chips that were flipped within this PhD.

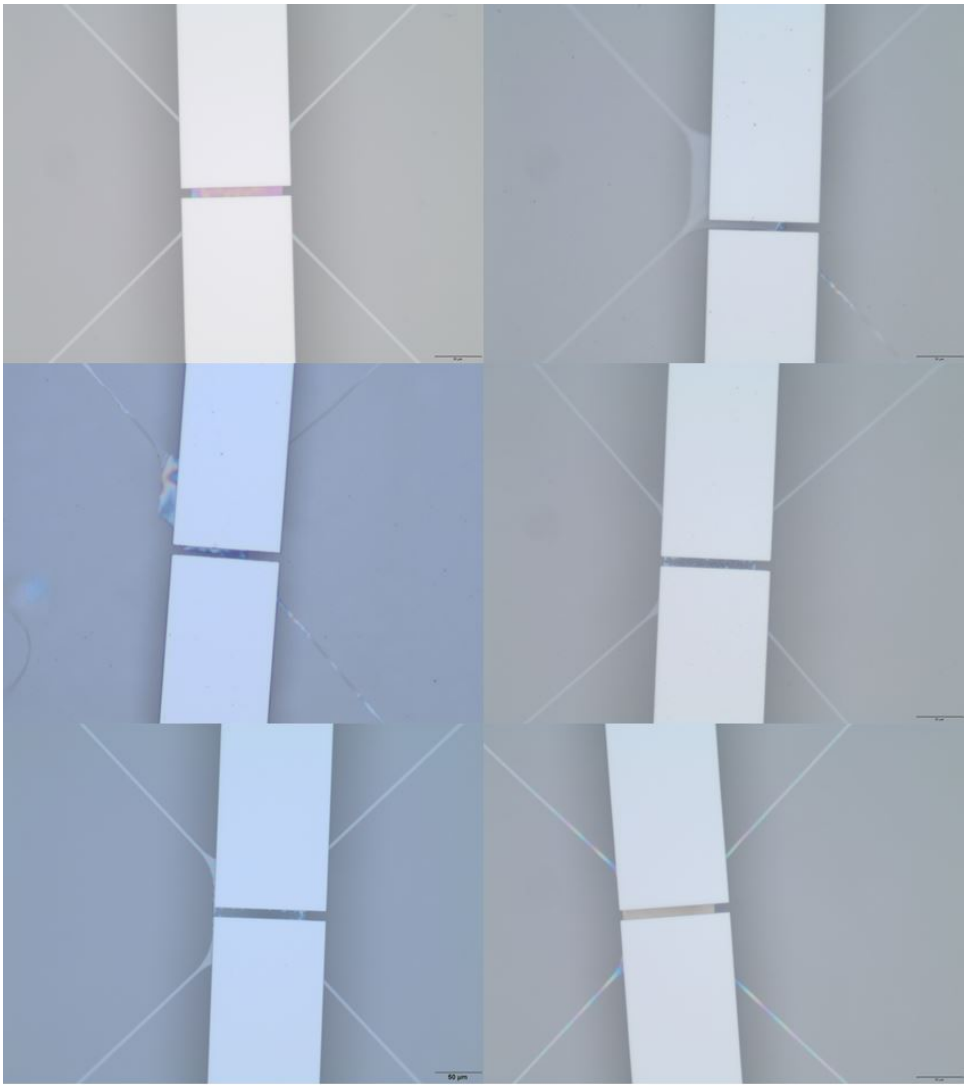

Figure 3.11: A visual demonstration of the fragility of the flip-chip method with trampolines. The vertical bars are the electrodes of the antenna chip and underneath you can see the trampoline. Close inspection reveals that the trampolines had either stuck to the antennas, or had broken tethers. Roughly 23 trampoline chips were flipped during this PhD.

- **Static electricity.** We tried to combat the possibility of static electricity building up on the chip by discharging the antenna on a probe station before flipping it. This did not help. We also tried to get rid of any static electricity by spraying it with a Milty Zerostat anti-static gun, however, this also did not seem to make a difference.

- **Different substrates.** We reasoned that different substrates would perhaps build up charge differently and induce breaking of the membrane, but again, we found no consistent patterns indicating this was the culprit.

3.7. MEASUREMENT SYSTEM

We shall now focus on the measurement systems which we used to measure the experiments within this thesis. For experiments where sensitivity is important, it is rewarding to measure using a cryogenic system as this reduces external vibrations. Furthermore, when working with superconductors, one must cross the transition temperature of the metal to be able to get the benefit of a conductor without resistance. We used two refrigeration systems to be able to reach different temperature ranges. A dilution refrigerator would be able to reach temperatures of 15 mK which would be suitable when using aluminium as a superconductor, but we also had a wet cryogenic system which would go to the boiling point of helium (4.2 K). This would be suitable when using a superconductor with a higher transition temperature, such as MoRe or NbTiN.

Having an as low as possible temperature also means that when you thermalize a harmonic oscillator to this temperature, you will reduce the average quanta occupation in the system, given by

$$\bar{n} = \left[\exp \frac{\hbar\omega}{k_B T} - 1 \right]^{-1} \tag{3.1}$$

which is the standard distribution for a bosonic system. In the context of optomechanics, this means that the thermal occupation of your cavity and mechanics will be governed by this distribution. For a GHz microwave cavity, the photon number will be in the ground state at dilution refrigerator temperatures. However, as the fundamental mode frequency of the mechanics is orders of magnitude lower than the cavity, its occupation can be significant. For our mechanical resonators that are in the hundreds of kHz, the occupation can be up to a few thousand. The issue is further complicated by the fact that mechanical vibrations of the pulse tube cooler of the refrigerator can easily couple to the mechanical system, making it difficult to determine the true effective bath temperature of the mechanical resonator. Calibration of the mode temperature is necessary to get a reliable figure for the mechanical occupation.

3.7.1. DILUTION REFRIGERATION SYSTEM

We used two different refrigeration systems, the BlueFors LD250, and the Oxford Instruments Triton 200. The latter system had a bottom-loading mechanism which would reduce cooling times to roughly 8 hours, as opposed to the full-day cooldown necessary for the former system. The immediate benefit of a dilution refrigeration unit – as mentioned above – is the reduced temperature, and thus lower contribution of thermal noise

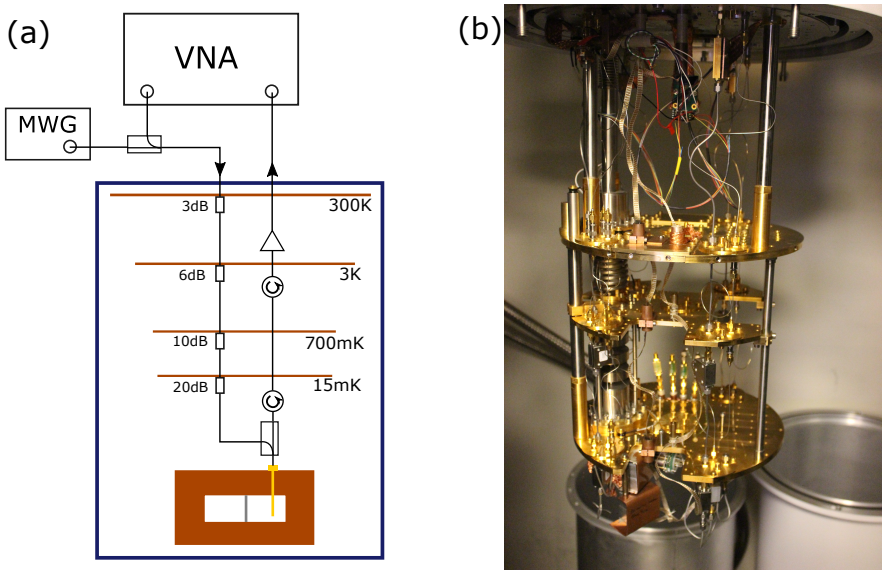

Figure 3.12: (a) A schematic of the dilution refrigeration cryogenic system. Two-tone measurements would be done with the output probe of a vector network analyzer (VNA) and a microwave generator (MWG) which would be combined using a directional coupler. The input line goes through attenuators at each temperature stage, and the output signal would be isolated and amplified by a high electron mobility transister (HEMT) amplifier. (b) A picture of the dilution refrigeration system without its vacuum can and shielding.

to your measurements. The downside is that as the cooling power is reduced at lower temperatures, the input power you can supply is also greatly reduced, as you run the risk of heating the system. The BlueFors LD250 has a cooling power of 10μW at 20 mK.

Using a 3D cavity means that you will have a higher thermal load, which means that special attention should be given to make sure that there is enough thermal conductivity between the cavity and the mixing plate, to ensure it reaches base temperature. We would always, if possible, screw the cavity into a copper plate, which would then be mounted onto the mixing plate. We would also wrap the 3D cavity with aluminium tape as tightly as possible to ensure thermal contact.

3.7.2. 4K FRIDGE SETUP

For experiments that had superconducting metals that had transition temperatures above 4 K, we could use our wet fridge. The system consisted of a copper chamber that would be submersed into a dewar of liquid helium. The top of this chamber would be connected to a steel tube which would allow wires to be accessed from the top, and a vacuum pump to reach base pressures of around 10^{-5} mBar. The system was designed such that the bottom plate on which the sample was fastened would have a tight connection to the outer walls such that thermal contact with the liquid helium would efficiently reach the device. A thermometer was fastened to the lowest stage to monitor the temperature.

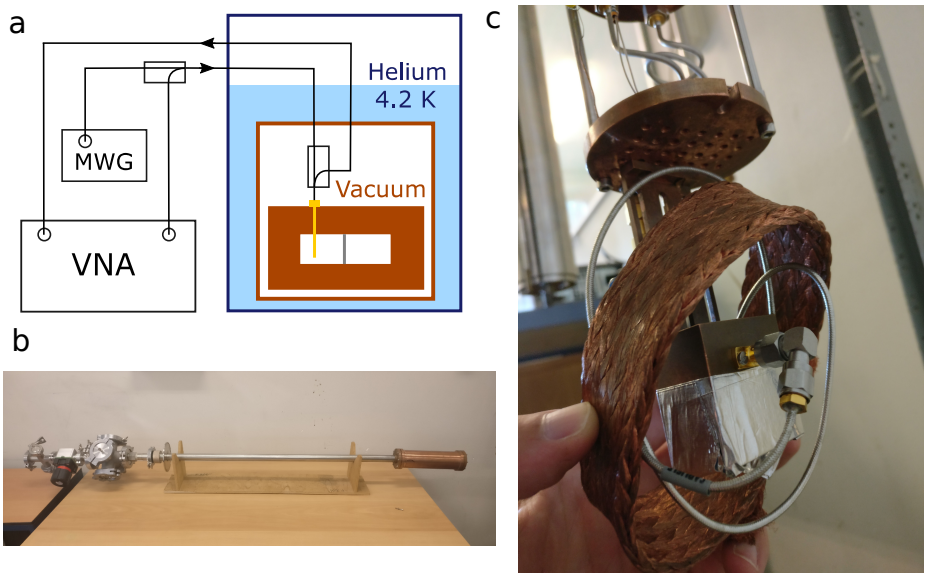

Figure 3.13: (a) A schematic of the 4 K cryogenic system. We put our 3D cavity into a dewar of liquid helium and connect to it through two directional couplers to a vector network analyzer (VNA) and a microwave generator (MWG). (b) A photograph of the 4K system before it is put inside of the helium dewar. (c) A picture of the 3D cavity when fully connected and fastened to the bottom plate before the copper chamber is screwed on. The copper braid is to improve thermal contact as much as possible. The directional coupler is behind, and is obstructed from view.

REFERENCES

[1] B. M. Zwickl, W. E. Shanks, A. M. Jayich, C. Yang, A. C. Bleszynski Jayich, J. D. Thompson, and J. G. E. Harris, *High quality mechanical and optical properties of commercial silicon nitride membranes,* Appl. Phys. Lett. **92**, 103125 (2008).

[2] P. Becker, P. Scyfried, and H. Siegert, *The lattice parameter of highly pure silicon single crystals,* Zeitschrift für Physik B Condensed Matter **48**, 17 (1982).

[3] C.-L. Tien and T.-W. Lin, *Thermal expansion coefficient and thermomechanical properties of sin x thin films prepared by plasma-enhanced chemical vapor deposition,* Applied optics **51**, 7229 (2012).

[4] L. G. Villanueva and S. Schmid, *Evidence of surface loss as ubiquitous limiting damping mechanism in SiN micro-and nanomechanical resonators,* Physical review letters **113**, 227201 (2014).

[5] V. Singh, B. H. Schneider, S. J. Bosman, E. P. Merkx, and G. A. Steele, *Molybdenum-Rhenium alloy based high-Q superconducting microwave resonators,* Applied Physics Letters **105**, 222601 (2014).

[6] P.-L. Yu, T. P. Purdy, and C. A. Regal, *Control of Material Damping in High-Q Membrane Microresonators,* Phys. Rev. Lett. **108**, 083603 (2012).

[7] R. A. Norte, J. P. Moura, and S. Gröblacher, *Mechanical resonators for quantum optomechanics experiments at room temperature,* Physical review letters **116**, 147202 (2016).

[8] C. Reinhardt, T. Müller, A. Bourassa, and J. C. Sankey, *Ultralow-noise SiN trampoline resonators for sensing and optomechanics,* Physical Review X **6**, 021001 (2016).

[9] G. Yan, P. C. Chan, I.-M. Hsing, R. K. Sharma, J. K. Sin, and Y. Wang, *An improved TMAH Si-etching solution without attacking exposed aluminum,* Sensors and Actuators A: physical **89**, 135 (2001).

[10] N. Fujitsuka, K. Hamaguchi, H. Funabashi, E. Kawasaki, and T. Fukada, *Aluminum protected silicon anisotropic etching technique using tmah with an oxidizing agent and dissolved si,* R&D. Rev. Toyota CRDL **39**, 34 (2004).

[11] D. L. Creedon, Y. Reshitnyk, W. Farr, J. M. Martinis, T. L. Duty, and M. E. Tobar, *High Q-factor sapphire whipsering gallery mode microwave resonator at single photon energies and millikelvin temperatures,* Applied Physics Letters **98**, 222903 (2011).

[12] H. Paik, D. Schuster, L. S. Bishop, G. Kirchmair, G. Catelani, A. Sears, B. Johnson, M. Reagor, L. Frunzio, L. Glazman, *et al.*, *Observation of high coherence in josephson junction qubits measured in a three-dimensional circuit qed architecture,* Physical Review Letters **107**, 240501 (2011).

[13] C. Rigetti, J. M. Gambetta, S. Poletto, B. Plourde, J. M. Chow, A. Córcoles, J. A. Smolin, S. T. Merkel, J. Rozen, G. A. Keefe, *et al.*, *Superconducting qubit in a waveguide cavity with a coherence time approaching 0.1 ms,* Physical Review B **86**, 100506 (2012).

[14] M. Reagor, W. Pfaff, C. Axline, R. W. Heeres, N. Ofek, K. Sliwa, E. Holland, C. Wang, J. Blumoff, K. Chou, *et al.*, *Quantum memory with millisecond coherence in circuit qed,* Physical Review B **94**, 014506 (2016).

[15] H. S. Padamsee, *Superconducting radio-frequency cavities,* Annual Review of Nuclear and Particle Science **64**, 175 (2014).

[16] M. Kelly and T. Reid, *Surface processing for bulk niobium superconducting radio frequency cavities,* Superconductor Science and Technology **30**, 043001 (2017).

[17] D. J. Wilson, *Cavity optomechanics with high-stress silicon nitride films* (California Institute of Technology, 2012).

4

HIGH-Q SILICON NITRIDE MEMBRANE RESONATORS AT MK TEMPERATURES

We study mechanical dissipation in millimeter-sized, high quality-factor (Q) metalized silicon nitride membranes at temperatures down to 14 *mK using a three-dimensional optomechanical cavity. Below* 200 *mK, high-Q modes of the membranes show a diverging increase of Q with decreasing temperature, reaching* $Q = 1.27 \times 10^8$ *at* 14 *mK, an order of magnitude higher than reported before. The ultra-low dissipation makes the membranes highly attractive for the study of optomechanics in the quantum regime, as well as for other applications of optomechanics such as microwave to optical photon conversion.*

Parts of this chapter have been published. Yuan, M., Cohen, M. A., Steele, G. A. (2015). Silicon nitride membrane resonators at millikelvin temperatures with quality factors exceeding 10^8. Applied Physics Letters, 107(26), 263501.

4.1. INTRODUCTION

Mechanical resonators made from silicon nitride have shown great potentials for both fundamental researches and applications. They have become platforms for studying quantum optomechanics [1–9] and key elements for applications such as optical to microwave photon transducers [10, 11] and NEMS/MEMS sensors [12–14]. High-stress SiN_x devices typically have very high quality factors, which is one of the most crucial features for a mechanical resonator. In optomechanics, low dissipation reduces the mechanical resonator's coupling to the environment and improves the cooperativity, enabling cooling to a lower temperature and state preparation with higher fidelity. High quality factors also enhances the efficiency of a transducer as well as the sensitivity of a NEMS/MEMS sensor.

Studies of the quality factor of SiN_x resonators have found Q-factors at room temperature of up to 10^6 for nanostrings [15], 10^5 for beams [12, 13], 10^5 for trampolines [16], and 10^6 for the fundamental mode of membranes [17]. Higher modes of membranes have been observed to have higher Q-factors [18, 19], up to 5×10^7 [19], but show weaker optomechanical coupling, and have smaller mode spacing leading to a dense mode spectrum. Smaller membranes were studied down to millikelvin temperatures, but Q was relatively low due to their lower aspect ratio [20]. Measurements of the Q of the fundamental mode of millimeter-sized membranes down to 300 mK demonstrated a plateau in Q below 1K at a value up to 10^7 [17].

Here, we study the quality factor of large, high-Q SiN_x membranes at temperatures down to 14 mK. We use a three-dimensional (3D) superconducting optomechanical cavity [9] to detect the motion. Similar to previous reports, we observe a plateau in Q down to 200 mK. Below 200 mK, we observe a new behavior of the quality factors of high-Q modes that diverges down to the lowest temperature we can measure, reaching a record of $Q = 1.27\times10^8$ for a fundamental mode at 14 mK, promising for future applications in optomechanics in both the microwave and optical domains.

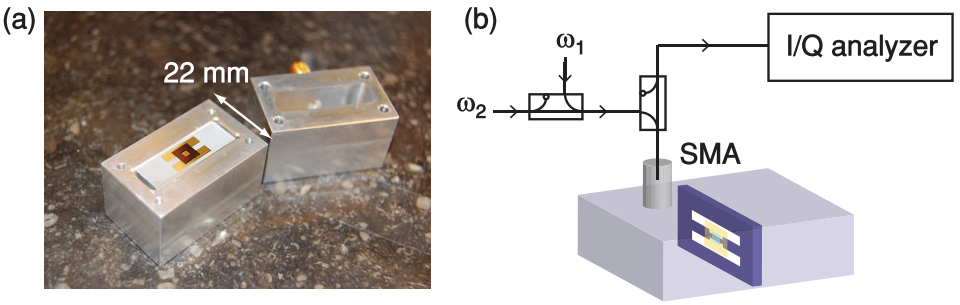

Figure 4.1: (a). Photograph of a physical device (Device I), showing two halves of the Al 3D cavity and the membrane resonator. (b). Schematic of the reflection measurement setup. Two microwave tones ω_1 and ω_2 are combined and launched into the membrane-embedded cavity placed inside a dilution refrigerator. The reflected signal is detected by an I/Q analyzer.

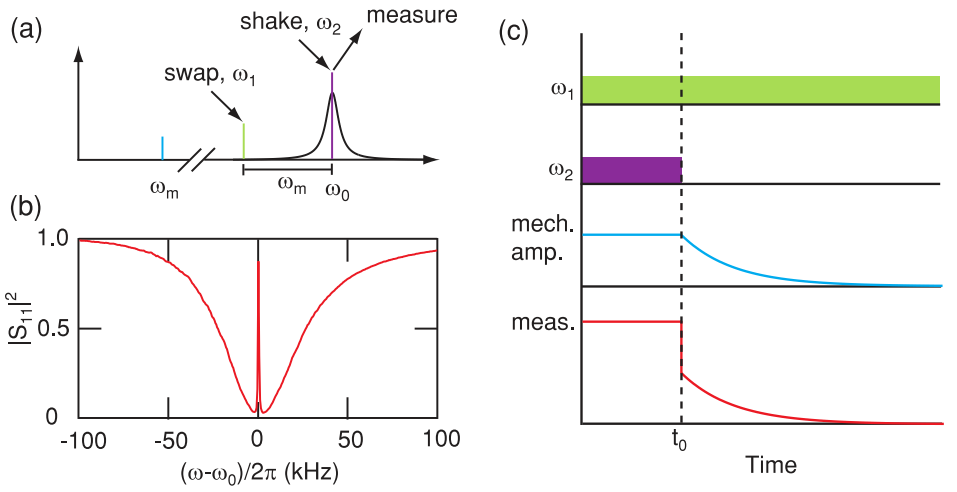

Figure 4.2: (a). Schematic of the measurement scheme. A swap tone at ω_1 is used to induce an optomechanical swap interaction between the cavity and the membrane. Another tone at $\omega_2 = \omega_0$ is used to shake the membrane. A vector signal analyzer is used to detect signal at ω_0. (b). OMIT with $C \gg 1$, showing $|S_{11}|^2$ as a function of frequency. To avoid optomechanical backaction, ringdown measurement is carried out in the $C \ll 1$ regime. (c) Schematic for measurement of ringdown with OMIT configuration. The swap tone ω_1 is kept on at all time while the shake tone is switched off at t_0, at which point the mechanical resonator starts to decay. The signal measured at ω_0 is a sum of the mechanical sideband generated by ω_1 and the reflected signal generated by ω_2. When ω_2 is switched off, the latter quickly diminishes (at a rate of κ), and the mechanical component of the signal at ω_2 rings down on a time scale corresponding to γ_m^{-1}.

4.2. EXPERIMENTAL DESIGN AND CHARACTERIZATION

A photograph of the device is shown in Fig. 4.1(a). The 3D cavity is formed by two halves of a machined Al block. An SMA connector is attached for reflection measurement. The mechanical resonator is a Norcada SiN_x membrane which can be seen on the sapphire support substrate. The membranes are 50 nm thick in a square of size $l \times l$ with l = 1.5 mm for Device I and l = 1 mm for Device II. We deposit a metal layer of 20 nm of Al on the membrane which forms a capacitor with the antenna pads deposited on the substrate. The motion of the membrane is coupled to the cavity field via the antenna. The membrane is anchored on the substrate with ~ 0.1 μl of 2-part epoxy at one corner of the silicon frame. The membrane-embedded 3D cavity is mounted with the plane of the membrane in the vertical direction in a cryo-free dilution refrigerator (BlueFors LD250) where fridge temperature is controlled between 14 mK and 800 mK.

We measure the cavity response and mechanical motion using microwave reflectometry as described in previous work [9]. A simplified schematic of the reflection measurement is illustrated in Fig. 4.1(b). Microwave signals are attenuated and sent into the cavity. The reflected signal is amplified and read out using a vector signal analyzer (Rohde and Schwarz FSV30) which records the in- and out-of-phase quadrature of the signal V_i and V_q as a function of time within a bandwidth up to 28 MHz around a local oscillator

reference frequency. We study two membrane-cavity devices. The cavity resonance ω_0 is $2\pi \times 5.23$ GHz for Device I and $2\pi \times 5.07$ GHz for Device II, with linewidths κ below 300 mK of $2\pi \times 56$ kHz and $2\pi \times 45$ kHz, respectively. The mechanical resonant frequency ω_m and the single-photon coupling rate g_0 for the modes studied are listed in table 4.1. In Device II, the gap to the antenna is 3μm. In Device I, the gap is 10μm, resulting in a significantly reduced g_0.

4.3. MECHANICAL QUALITY FACTOR RESULTS AND DISCUSSION

To measure the quality factor, we drive the membrane at its resonance frequency and then detect the timescale it takes for the motion to ring down (decay). The membrane is driven optomechanically, with a scheme based on an optomechanically-induced transparency (OMIT) measurement. As illustrated in Fig. 4.2(a), two phase-locked microwave signals are sent into the cavity: a swap tone at $\omega_1 = \omega_0 - \omega_m$ and a shake tone at $\omega_2 = \omega_0$. Photons at ω_1 are Raman scattered by the membrane resonator and upconverted into the cavity resonance, producing a mechanical sideband at ω_0. The shake tone at ω_2 is used to drive the membrane. The I/Q analyzer is set to detect the signal at ω_0 with a sample rate of 100 Hz. Fig. 4.2(b) shows an example of OMIT measurement taken with Device II in the limit of large optomechanical cooperativity $C = \frac{4g_0^2 N}{\kappa\gamma_m} \gg 1$, where N is the number of photons. To avoid backaction of the microwave fields on the motion, for the ringdown measurement we operate in a regime where the cooperativity C of the swap tone is sufficiently small ($C \ll 1$).

Device	I		II	
Mode	(1,1)	(1,1)	S	AS
$\omega_m/2\pi$ (kHz)	242	121	193	192
$g_0/2\pi$ (Hz)	0.03	0.22	0.01	0.01

Table 4.1: Summary of mechanical modes studied. Fundamental mode (1,1), symmetric mode (S), and antisymmetric mode (AS).

Fig. 4.2(c) illustrates the protocol of the optomechanical ringdown measurement. The membrane is first driven into motion when ω_1 and ω_2 are both on. The detected signal at ω_0 consists of the directly reflected signal of the shake tone at ω_2 as well as the mechanical sideband generated from the swap tone at ω_1. At t_0 the shake tone is switched off, while the swap tone ω_1 stays on. When turning off the shake tone, the associated microwave field at ω_0 decays on a timescale corresponding to κ^{-1}. In addition to the microwave field from the shake tone, there is a second microwave field at ω_0 that arises from a sideband of the swap tone generated by the mechanical motion. This second microwave field decays with a much slower timescale corresponding to γ_m^{-1}. On the I/Q analyzer, we then observe a signal at ω_0 from shake tone ω_2 that falls off at the cavity decay rate κ and the remaining mechanical ringdown signal is read out and used to calculate the mechanical amplitude as it decays.

Fig. 4.3(a) shows an example of a ringdown trace of the mechanical resonator taken at

14 mK. The y-axis is proportional to $V_i^2 + V_q^2$, representing the squared amplitude of the resonator. By fitting the curve to an exponential decay $e^{-\gamma_m t}$, γ_m and the quality factor $Q = \omega_m/\gamma_m$ can be extracted. We vary the cryostat temperature T and record the corresponding ringdown traces. The resultant Q-factor as a function of temperature T for Device I (1,1) mode is plot in a linear scale in Fig. 4.3(b). As T is decreased from 800 mK to 200 mK, there is a relatively flat plateau in Q, consistent with previous results with an optical detection scheme [17]. As T is further reduced to below 200 mK, Q begins to go up, and continues rising with no indication of saturation down to the base temperature of $T = 14$ mK. The highest value $Q = 1.27 \times 10^8$ corresponds to $\gamma_m = 1.9$ mHz and a time constant of $\tau = 2/\gamma_m = 1.6 \times 10^2$ s.

In Fig. 4.3(c) we plot the Q of Device I (1,1) mode (red), Device II (1,1) mode (blue) and Device II antisymmetric (AS) mode (green) together in a log scale. Note that the symmetry of the mode is determined with a reflection plane perpendicular to the membrane through the corner. Quality factors of all three modes are above 5×10^6 and show similar behavior, improving with decreasing temperature below 200 mK and leveling off between 200 mK and 800 mK. It is also interesting to note that although previous work with Device II observed a saturation of the mode temperature at 180 mK [9], Q continues to go up as the cryostat is cooled down to base temperature. In contrast to the other modes, symmetric (S) mode of Device II has a much lower $Q = 1.2 \times 10^5$ that is independent of temperature from 14 to 800 mK. Although the S mode and AS mode are separated by only 1 kHz in frequency, it is striking that Q-factors are different by orders of magnitude. The S mode could have a temperature-independent Q limited by radiation into the sapphire substrate, while the AS mode would then be limited by a different temperature-dependent mechanism.

In the ringdown experiments performed here with the I/Q analyzer, we are able to determine not only the energy loss rate of the mechanical resonator, but also to characterize the dephasing of its mechanical motion. Applying an FFT to the acquired I/Q data from sufficiently long ringdown time trace, one can reconstruct the spectral content of the mechanical resonance during ringdown, giving access to the spectral linewidth Q-factor [21]. To do this, we slightly detune the swap tone $\omega_1 = \omega_0 - \omega_m - \delta$ with $\delta = 2\pi \times 31.9$ mHz and measure the I/Q data for 10^4 seconds. In Fig. 4.4(a) the I/Q vector plot is shown, the x-axis representing the in-phase quadrature V_i and the y-axis the out-of-phase quadrature V_q. The trace forms a spiral: the decrease of the vector length corresponds to the decay in mechanical amplitude, and the angular frequency of the trajectory in the polar plot is determined by δ. To recontstruct a spectrum from the data, we perform an FFT of the complex vector $V_i + jV_q$, $j = \sqrt{-1}$, shown in Fig. 4.4(b). A fit to the lineshape gives the spectral $Q = 1.10 \pm 0.05 \times 10^8$, in agreement, to within the error margin, with the ringdown quality factor 1.14×10^8 extracted from the same dataset, demonstrating that the dephasing is not a significant source of decoherence for these membrane resonators.

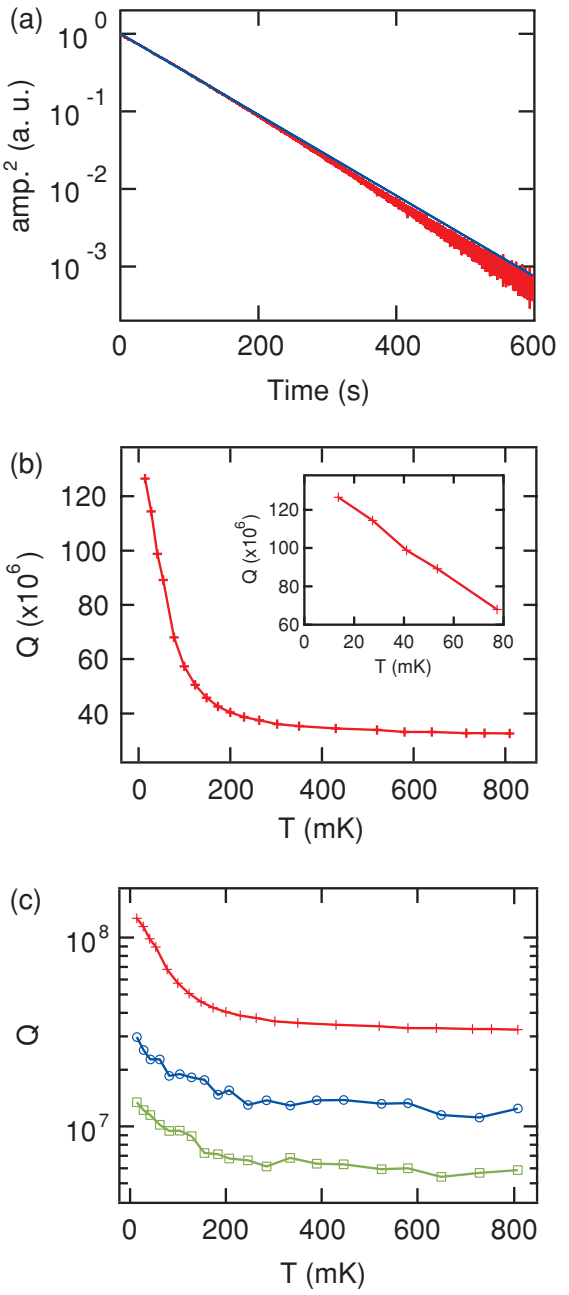

Figure 4.3: (a). Time trace of the mechanical amplitude during ringdown for Device I at 14 mK. From a fit to exponential decay, we extract the mechanical quality factor. Red: data; blue: fit. The deviation from a straight line may indicate some weak negative nonlinear damping. (b). Extracted quality factor Q of the membrane resonator as a function of cryostat temperature for Device I (1,1) mode. Inset: zoom-in for $T < 80$ mK. The highest value is $Q = 1.27 \times 10^8$ for Device I at 14 mK. (c). Extracted quality factor for both samples. Red: Device I (1,1) mode; blue: Device II (1,1) mode; green: Device II AS mode. Q decreases with increasing temperature for 14 mK $< T <$ 200 mK, leveling out between 200 mK and 800 mK.

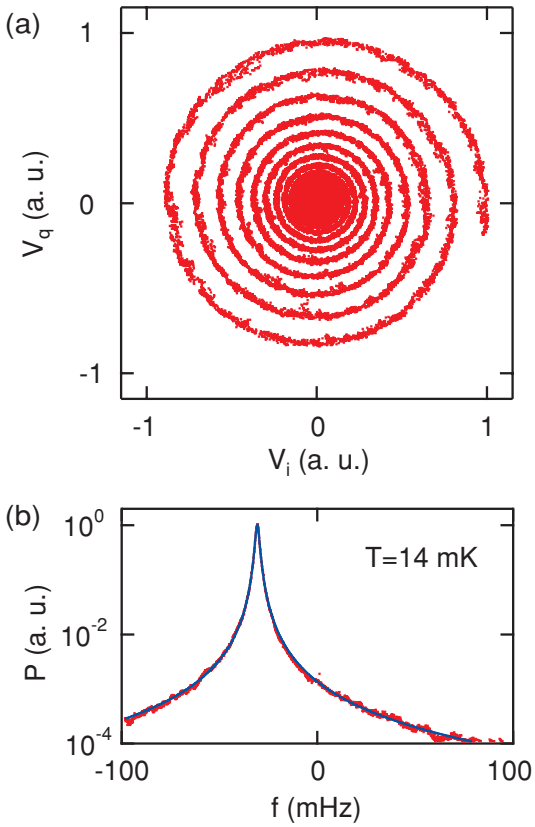

Figure 4.4: I/Q analysis of the ringdown trace. Swap tone is set to $\omega_1 = \omega_0 - \omega_m - \delta$, $\delta = 2\pi \times 31.9$ mHz. (a). Out-of-phase quadrature V_q vs. in-phase quadrature V_i. Decay of the amplitude in combination with the detuning δ of the swap tone results in spiral that circles around the origin at an angular frequency δ. (b). FFT spectrum of the complex temporal I/Q trace. Red: data; blue: fit. From the linewidth of the resonance the decoherence, including dephasing and relaxation, can be extracted. By comparing the spectral quality factor $1.10 \pm 0.05 \times 10^8$ and the ringdown quality factor 1.14×10^8, the contribution of dephasing to the spectral linewidth is negligible within the error margin.

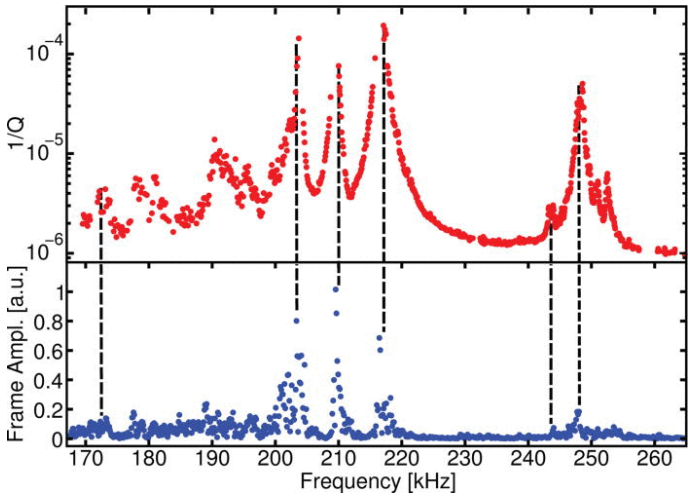

Figure 4.5: A figure taken from Ref. [29]. The upper plot describes the inverse quality factor Q^{-1} of the fundamental mode of the square membrane when measured by ringdown. The bottom plot shows the measured vibrations of the membrane substrate when the laser interferometer is pointed at the frame.

4.4. CONCLUSION

In conclusion, we have measured the quality factor of SiN_x membranes at millikelvin temperature with 3D optomechanical cavities. At the base temperature of 14 mK, Q-factors as high as 1.27×10^8 are observed for a fundamental mode, demonstrating the exceptional performance of SiN_x membranes as mechanical resonators. This high Q is achieved in the presence of an Al coating of the membrane, expanding their potential in electrical and microwave applications. By virtue of this low dissipation, SiN_x membranes could be a test bed for quantum superposition states of massive mechanical objects and other applications in optomechanics.

4.5. APPENDIX: EXTENDED DISCUSSION

On closer inspection, the fact that the fundamental modes of our silicon nitride membranes show temperature dependence is a little odd. Many articles have been written which demonstrate that lower modes of membranes tend to be limited by radiation losses [19, 22–24]. And often the effect is even worse when the substrate is glued to another surface [19, 25–27]. However, our paper is also not the only one to demonstrate temperature dependence [28]. If a resonator is limited by radiation losses, it would not show temperature dependence. We believe that the publication by Jöckel et al. most enlightens this issue [29].

The experiment describes a laser interferometer setup where the movement of a square silicon nitride membrane is measured inside a vacuum chamber and is driven by a piezo. Another laser is directed at the membrane and is able to heat the membrane,

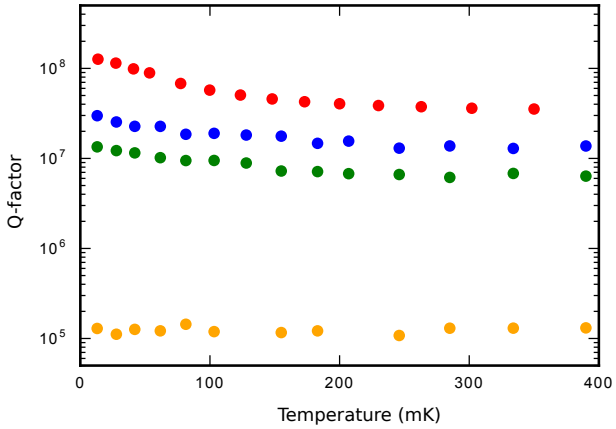

Figure 4.6: A more complete figure of all the quality factors measured of our two devices. Red: Device I (1,1) mode; blue: Device II (1,1) mode; green: Device II (1,2) mode; orange: Device II (2,1) mode. From this it can be seen that there is a huge discrepancy between the two AS/S modes of Device II. Mode S does not even show any temperature dependence.

causing tuneability of the membrane's frequency due to thermal expansion. They were able to measure the quality factor of the fundamental mode for a range of frequencies from 170 kHz to 260 kHz, as seen in Fig. 4.5 using ringdown measurements. At the same time, the interferometer can be pointed to the frame, and the amplitude of vibration can be measured for the same frequency range. What results is that at the frequencies where the frame amplitude is greatest, the quality factor of the fundamental mode of the membrane is also the lowest. What results is clear evidence that there is significant coupling between the frame modes and the membrane modes. Overlap between the two can lead to radiation losses.

The substrate of the membrane can act as a mechanical Purcell filter where the decay rate of the resonator is influenced by the density of states of its environment, and we believe such is the case in our experiment. Cooling of the device causes the modes of the bulk to change in frequency and in loss rate, which affects the overlap with the mechanical modes. Due to the fact that the modes always move up in quality factor the lower the temperature, we believe that the dominant effect is that the linewidth of the substrate modes become smaller, decreasing overlap.

Another culprit could be the change in mechanical properties of the glue over temperature. A change in stiffness could increase the mechanical impedance mismatch between the substrate and environment, which would effectively increase the quality factor of the substrate modes. We believe that the placement of the glue is also responsible for the symmetry dependence of radiation losses in the AS/S modes of Device II. Looking at Fig. 4.6 one can see that these two modes show widely different behavior.

The mode which has a node which crosses the glue will exert a smaller net force on the glue and will be less coupled to the environment. This is further evidence that our resonator is limited by radiation losses. Due to the inconsistencies of placing the glue on the membrane, many groups are taking the route of fabricating membranes with phononic shields [30, 31].

REFERENCES

[1] J. D. Thompson, B. M. Zwickl, A. M. Jayich, F. Marquardt, S. M. Girvin, and J. G. E. Harris, *Strong dispersive coupling of a high-finesse cavity to a micromechanical membrane.* Nature **452**, 72 (2008).

[2] G. Anetsberger, O. Arcizet, Q. P. Unterreithmeier, R. Rivière, A. Schliesser, E. M. Weig, J. P. Kotthaus, and T. J. Kippenberg, *Near-field cavity optomechanics with nanomechanical oscillators,* Nat. Phys. **5**, 909 (2009).

[3] M. D. LaHaye, O. Buu, B. Camarota, and K. C. Schwab, *Approaching the quantum limit of a nanomechanical resonator.* Science **304**, 74 (2004).

[4] A. Naik, O. Buu, M. D. LaHaye, A. D. Armour, A. A. Clerk, M. P. Blencowe, and K. C. Schwab, *Cooling a nanomechanical resonator with quantum back-action.* Nature **443**, 193 (2006).

[5] T. Rocheleau, T. Ndukum, C. Macklin, J. B. Hertzberg, A. A. Clerk, and K. C. Schwab, *Preparation and detection of a mechanical resonator near the ground state of motion,* Nature **463**, 72 (2010).

[6] T. P. Purdy, R. W. Peterson, and C. A. Regal, *Observation of radiation pressure shot noise on a macroscopic object.* Science **339**, 801 (2013).

[7] T. P. Purdy, P.-L. Yu, R. W. Peterson, N. S. Kampel, and C. A. Regal, *Strong Optomechanical Squeezing of Light,* Phys. Rev. X **3**, 031012 (2013).

[8] H. J. Eerkens, F. M. Buters, M. J. Weaver, B. Pepper, K. Heeck, P. Sonin, S. D. Man, and D. Bouwmeester, *Optical side-band cooling of a low frequency optomechanical system,* Opt. Express **23**, 71 (2015).

[9] M. Yuan, V. Singh, Y. M. Blanter, and G. A. Steele, Nat. Commun. **6**, 8491 (2015).

[10] T. Bagci, A. Simonsen, S. Schmid, L. G. Villanueva, E. Zeuthen, J. Appel, J. M. Taylor, A. Sørensen, K. Usami, A. Schliesser, and E. S. Polzik, *Optical detection of radio waves through a nanomechanical transducer,* Nature **507**, 81 (2014).

[11] R. Andrews, R. Peterson, T. Purdy, K. Cicak, R. W. Simmonds, C. A. Regal, and K. W. Lehnert, *Bidirectional and efficient conversion between microwave and optical light,* Nat. Phys. **10**, 321 (2014).

[12] Q. P. Unterreithmeier, E. M. Weig, and J. P. Kotthaus, *Universal transduction scheme for nanomechanical systems based on dielectric forces.* Nature **458**, 1001 (2009).

[13] T. Faust, P. Krenn, S. Manus, J. P. Kotthaus, and E. M. Weig, *Microwave cavity-enhanced transduction for plug and play nanomechanics at room temperature.* Nat. Commun. **3**, 728 (2012).

[14] K. Y. Fong, W. H. P. Pernice, M. Li, and H. X. Tang, *High Q optomechanical resonators in silicon nitride nanophotonic circuits,* Appl. Phys. Lett. **97**, 073112 (2010).

[15] S. S. Verbridge, J. M. Parpia, R. B. Reichenbach, L. M. Bellan, and H. G. Craighead, *High quality factor resonance at room temperature with nanostrings under high tensile stress,* J. Appl. Phys. **99**, 124304 (2006).

[16] D. Kleckner, B. Pepper, E. Jeffrey, P. Sonin, S. M. Thon, and D. Bouwmeester, *Optomechanical trampoline resonators,* Opt. Express **19**, 19708 (2011).

[17] B. M. Zwickl, W. E. Shanks, A. M. Jayich, C. Yang, A. C. Bleszynski Jayich, J. D. Thompson, and J. G. E. Harris, *High quality mechanical and optical properties of commercial silicon nitride membranes,* Appl. Phys. Lett. **92**, 103125 (2008).

[18] V. P. Adiga, B. Ilic, R. a. Barton, I. Wilson-Rae, H. G. Craighead, and J. M. Parpia, *Approaching intrinsic performance in ultra-thin silicon nitride drum resonators,* J. Appl. Phys. **112**, 064323 (2012).

[19] S. Chakram, Y. Patil, L. Chang, and M. Vengalattore, *Dissipation in Ultrahigh Quality Factor SiN Membrane Resonators,* Phys. Rev. Lett. **112**, 127201 (2014).

[20] J. Suh, A. J. Weinstein, and K. C. Schwab, *Optomechanical effects of two-level systems in a back-action evading measurement of micro-mechanical motion,* Appl. Phys. Lett. **103**, 052604 (2013).

[21] B. H. Schneider, V. Singh, W. J. Venstra, H. B. Meerwaldt, and G. A. Steele, *Observation of decoherence in a carbon nanotube mechanical resonator.* Nat. Comms. **5**, 5819 (2014).

[22] I. Wilson-Rae, R. Barton, S. Verbridge, D. Southworth, B. Ilic, H. Craighead, and J. Parpia, *High-q nanomechanics via destructive interference of elastic waves,* Physical review letters **106**, 047205 (2011).

[23] P.-L. Yu, T. P. Purdy, and C. A. Regal, *Control of Material Damping in High-Q Membrane Microresonators,* Phys. Rev. Lett. **108**, 083603 (2012).

[24] V. Adiga, B. Ilic, R. Barton, I. Wilson-Rae, H. Craighead, and J. Parpia, *Modal dependence of dissipation in silicon nitride drum resonators,* Applied Physics Letters **99**, 253103 (2011).

[25] D. J. Wilson, *Cavity optomechanics with high-stress silicon nitride films* (California Institute of Technology, 2012).

[26] L. G. Villanueva and S. Schmid, *Evidence of surface loss as ubiquitous limiting damping mechanism in SiN micro-and nanomechanical resonators,* Physical review letters **113**, 227201 (2014).

[27] D. Wilson, C. Regal, S. Papp, and H. Kimble, *Cavity optomechanics with stoichiometric sin films,* Physical review letters **103**, 207204 (2009).

[28] B. Zwickl, W. Shanks, A. Jayich, C. Yang, A. Bleszynski Jayich, J. Thompson, and J. Harris, *High quality mechanical and optical properties of commercial silicon nitride membranes,* Applied Physics Letters **92**, 103125 (2008).

[29] A. Jöckel, M. T. Rakher, M. Korppi, S. Camerer, D. Hunger, M. Mader, and P. Treutlein, *Spectroscopy of mechanical dissipation in micro-mechanical membranes,* Applied physics letters **99**, 143109 (2011).

[30] R. Fischer, N. Kampel, G. Assumpção, P.-L. Yu, K. Cicak, R. Peterson, R. Simmonds, and C. Regal, *Optical probing of mechanical loss of a si_ {3} n_ {4} membrane below 100 mk,* arXiv preprint arXiv:1611.00878 (2016).

[31] Y. Tsaturyan, A. Barg, E. S. Polzik, and A. Schliesser, *Ultracoherent nanomechanical resonators via soft clamping and dissipation dilution,* Nature nanotechnology **12**, 776 (2017).

5

A SPLIT 3D CAVITY DESIGN FOR THE INCORPORATION OF A DC BIAS

We report on a technique for applying a DC bias in a 3D microwave cavity. We achieve this by isolating the two halves of the cavity with a dielectric and directly using them as DC electrodes. As a proof of concept, we embed a variable capacitance diode in the cavity and tune the resonant frequency with a DC voltage, demonstrating the incorporation of a DC bias into the 3D cavity with no measurable change in its quality factor at room temperature. We also characterize the architecture at millikelvin temperatures and show that the split cavity design maintains a quality factor $Q_i \sim 8.8 \times 10^5$, making it promising for future quantum applications.

Parts of this chapter have been published. Cohen, M. A., Yuan, M., de Jong, B. W., Beukers, E., Bosman, S. J., Steele, G. A. (2017). A split-cavity design for the incorporation of a DC bias in a 3D microwave cavity. Applied Physics Letters, 110(17), 172601.

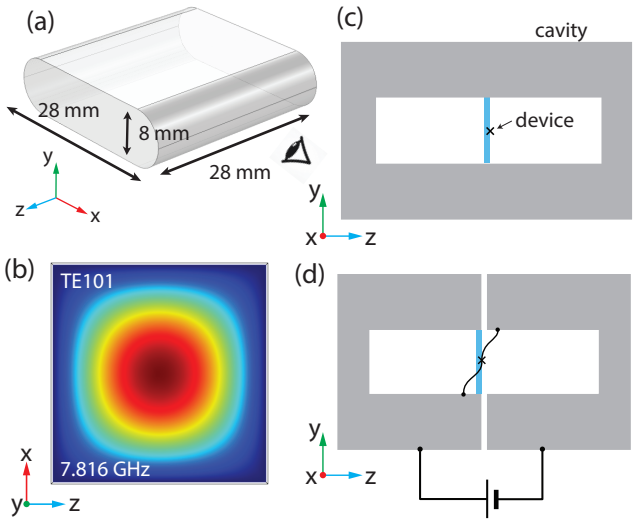

Figure 5.1: Implementation of a galvanically accessible 3D cavity by a split-cavity design. (a) Design of the 3D cavity. The eye icon signifies the viewpoint for subfigures (c) and (d). (b) Electric field magnitude of TE101 mode modelled by COMSOL. (c) A standard implementation of a nanodevice embedded inside 3D cavity without galvanic access. The blue line represents the substrate on which the device is fabricated, silicon or sapphire, for example. (d) Our proposed modification to the cavity geometry to allow a DC bias to be applied.

5.1. INTRODUCTION

In recent years, interest in 3D waveguide cavity resonators has been revived in the Josephson junction quantum bit (qubit) community [1–7]. Significantly enhanced relaxation and decoherence times on the order of hundreds of microseconds have been demonstrated for qubits in 3D cavities [7]. The 3D architecture has also enabled the measurement of entangled qubits [6], single-photon Kerr effect [2] as well as the Autler-Townes effect [3]. So far, these results are achieved without the need of applying DC currents or voltages to the devices embedded in the cavities. However, the ability to do so would significantly expand the application of 3D cavities, just as the introduction of a DC bias into a coplanar waveguide cavity made it much more versatile [8–10]. For example, such a DC bias could enable the tuning of a membrane in a 3D optomechanical device [11]. For qubit measurements, an on-chip flux bias can be added by applying a DC current bias to allow frequency tunability of the qubit.

Having galvanic access to a quantum device inside a 3D cavity presents a significant challenge. Planar geometries have a 1D confinement of the electromagnetic field and thus allows access from the side of the cavity [8, 9]. In 3D architectures currents run along a closed 3D surface: incorporating wires into devices inside the cavity without compromising the cavity quality factor is challenging. One study reports a technique of

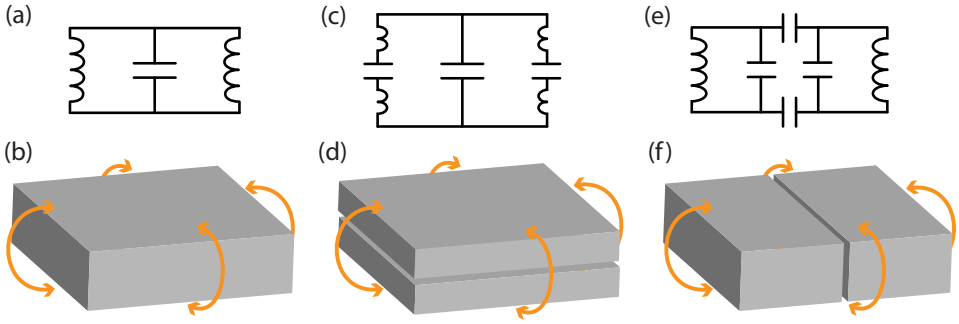

Figure 5.2: Minimizing losses of TE101 mode of a split-cavity through choice of orientation of splitting the cavity. (a) An LC circuit representation of a cavity resonating in the fundamental mode. (b) A corresponding 3D representation of a box cavity where the orange arrows show the direction of current flow. For the TE101 mode, the current paths along the side walls act as inductors, and the top and bottom walls as capacitor plates. (c-d) A circuit diagram and 3D representation of one proposed method of galvanically separating the box cavity. When introducing a separation perpendicular to the current flow, this adds capacitances between the inductors of the fundamental mode. (e-f) A circuit diagram and 3D representation of the method of separating the box cavity we use here for the incorporation of the DC bias. The plane of separation is parallel to the direction of current flow.

doing so by inserting a sample with wires on a PCB board into a hole in the side of the 3D cavity [12]. These DC wires enabled manipulation of a quantum dot inside the cavity, although this method suffered from a relatively low quality factor $Q_L = 1350$.

5.2. SPLIT 3D CAVITY DESIGN

We introduce a method for biasing a 3D cavity while maintaining an internal quality factor of $Q_i = 8.75 \pm 0.03 \times 10^5$. The dimensions of our near-rectangular cavity are illustrated in Fig. 5.1(a). The rounded corners in the xy-plane have a diameter equal to the height of the y-coordinate. According to a finite element simulation shown in Fig. 5.1(b) the resonant frequency of the lowest TE101 mode is expected to be around 7.816 GHz. The color corresponds to the magnitude of the electric field in the zx-plane, at the center of which the field reaches maximum. The measured resonant frequency of the bare cavity is $f_0 = 7.743$ GHz at room temperature and ambient conditions. The loaded Q-factor at room temperature is $Q_L = 3920$. Many implementations use a 3D cavity that is cut in half to allow for a nanodevice to be placed inside. The device is usually fabricated on a dielectric substrate and placed in the center to allow maximum interaction with the electric field. The idea in this article is to use this separation to our advantage by keeping the two halves galvanically separated and applying a DC voltage across it to bias the nanodevice. Such a connection could be achieved through a custom-designed substrate including connections to the back side of the substrate.

In designing the location of the split in the rectangular 3D cavity, it is important to consider how currents flow within such a resonant structure. For the fundamental mode

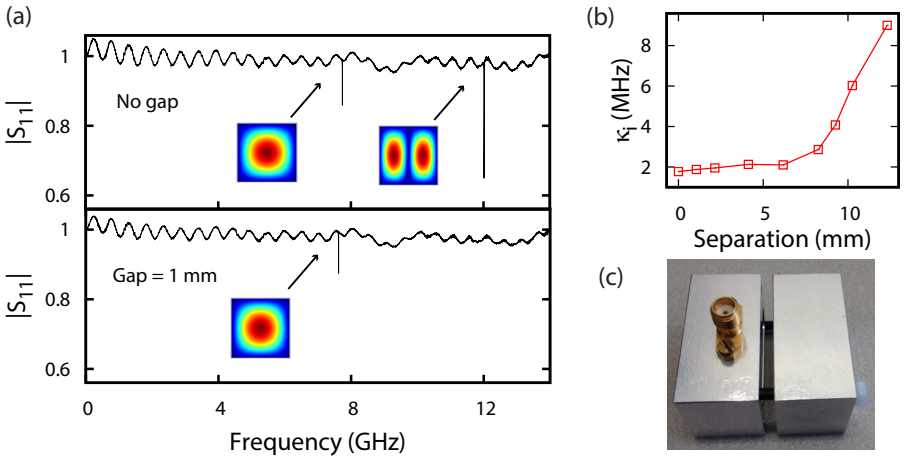

Figure 5.3: Experimental observations from room temperature measurements showing that TE101 mode is not affected to first order even for relatively large gaps. (a) Full spectrum of the reflection coefficient for a (top) closed cavity, and (bottom) a cavity separated by 1.07 mm measured at room temperature. The disappearance of the second mode is attributed to the restriction of current across the two halves. (b) A graph of the internal dissipation rate κ_i as a function of cavity separation. (c) A picture of the setup we used to separate the cavity halves. The screws used to connect them were surrounded by an insulating layer.

of the cavity, electrons oscillate back and forth between the plates with the largest area via the side walls. One can see this as a simple LC circuit, where the top and bottom plates act as a capacitor, and current path along the side walls as an inductance. There are two ways we can split this cavity, parallel or perpendicular to the direction of current flow. Fig. 5.2(c-d) shows a split cavity where the cut is perpendicular. Such a geometry creates additional capacitances in between the inductors which turns it into a dipole antenna, potentially causing losses by radiation. An alternative geometry would be to split the cavity as depicted in Fig. 5.2(e-f). The circuit diagram changes by splitting the capacitance of the LC circuit and separating these by two more capacitances. Since there is a far lower current density at the split, there likely is less chance of radiation losses. A thorough investigation into the losses from seams in cavities is given in Ref. [13].

Similar to the coaxial pin used to couple microwaves in and out of the cavity via the readout port, adding a DC wire that fully enters into the cavity would have a significant impact on the cavity Q-factor as it would act as an antenna and contribute heavily to radiative losses. It is in principle possible to partially suppress this leakage using low pass filters, although this presents challenges in terms of the loss rates of the elements and maintaining sufficient grounding to limit radiative losses. In the approach presented here, we avoid such potential problems by separating the two hemispheres of the cavity with a thin layer of insulator and using them directly as electrodes. The interface of the two halves forms a large capacitor that acts as a low-pass filter. We directly apply the DC voltage on the aluminum blocks, which can then be accessed from inside the cavity to

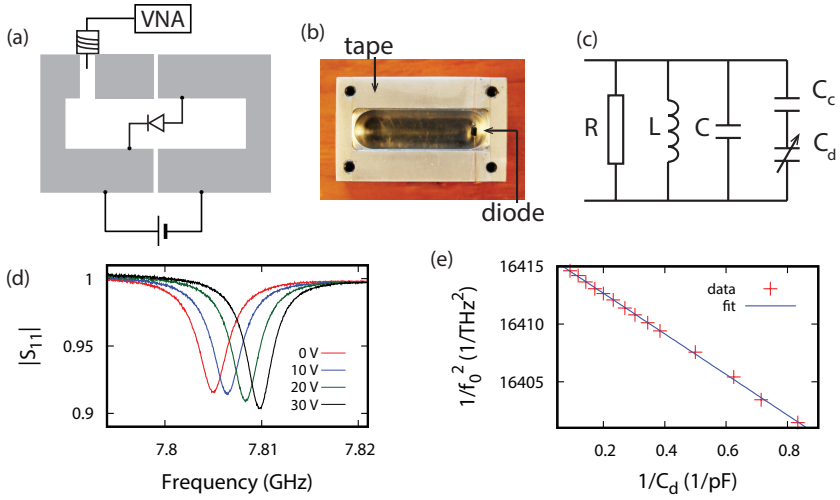

Figure 5.4: Proof-of-concept demonstration of a DC tuneable 3D cavity using an embedded reverse biased diode. (a) Schematic of the experimental setup. The diode is reverse-biased by an external voltage applied across the cavity and the resonant frequency is measured reflectively. (b) A photograph of one half of the aluminum cavity. (c) An equivalent circuit diagram. The tuneable diode capacitance C_d is coupled in parallel to the main cavity through C_c. (d) Representative S_{11} curves measured by the vector network analyzer at room temperature as the bias voltage is varied. The resonant frequency is shifted but the quality factor preserves. (e) Inverse square of the resonant frequency as a function of the inverse of the diode capacitance.

connect the DC signals to the device, as illustrated in Fig.5.1(d). Using superconducting wires from the two halves of the cavity to devices embedded in it, such as qubits, one can then apply voltage or current biases to the devices. This could also potentially be implemented with traces directly on the sapphire substrates used to hold the devices in the cavity. The bandwidth of this DC bias scheme is limited by the capacitance between the two hemispheres and can be carefully engineered. For a 50 Ω source impedance supplying the DC signals and a 100 μm layer Kapton tape insulator with a 180 pF capacitance between the hemispheres, we estimate the bandwidth for the DC signals to be around 18 MHz, and could be even higher if the driving were provided by a lower impedance source.

5.3. MEASUREMENT OF BIASED 3D SPLIT CAVITY

To demonstrate the viability of biasing a split 3D cavity, we first present measurements studying how the quality factor is affected by introducing this split at room temperature. In Fig. 5.3(a) we show a full spectrum sweep as allowed by our vector network analyzer when the cavity is closed and when the cavity halves are separated by around 1.07 mm. Both configurations display a fundamental frequency, however with a slight shift: 7.74 GHz when closed, 7.62 GHz when opened, about a 1.6% change. This percentage shift was predicted well by finite element simulations by increasing the length of the box resonator, ignoring the open walls in the region of the gap. There is also a second mode, TE201, at 12.02 GHz, but this can only be detected when the cavity is closed. One can understand this by the fact that the TE201 mode has a large component of current that flows across the split. When the two halves are separated, this current is presented with a large impedance from the capacitor and is therefore strongly suppressed. Even up to very large gaps on the order of millimeters, the linewidth of the TE101 mode, shown in Fig. 5.3(b), is relatively constant, indicating that at room temperature, the radiative losses are negligible even for millimeter gaps between the two halves.

To demonstrate the principle of DC operation of a device inside a cavity, we embed a diode (NXP BB131) inside the cavity. The diode capacitance can be tuned by a reverse voltage bias and the cavity resonant frequency is subsequently shifted. The interface of the left and right halves are separated by a thin layer of scotch tape which acts as an insulator (0.05 mm thickness), and nylon screws are used to avoid shorts. Inside, the anode (cathode) of the diode is attached to the right (left) half of the cavity. An external DC voltage source is attached to the aluminum blocks, reverse-biasing the diode via the cavity walls. One half of the actual cavity is shown in Fig. 5.4(b). An equivalent parallel circuit model is illustrated in Fig. 5.4(c), in which the resistance R, the inductance L and the capacitance C model the basic resonance while the capacitance of the diode C_d is coupled to the circuit in the model via an effective coupling capacitor C_c.

We perform a reflection measurement with an input power of 0 dBm. In Fig. 5.4(d), we plot the reflection coefficient S_{11}, normalized by the off-resonant background as a function of the frequency f. The resonant frequency f_0 shifts to higher values as we increase the reverse bias voltage V applied on the diode. The quality factors of the cavity show no signs of decrease for V as high as 30 V, and also show no systematic change

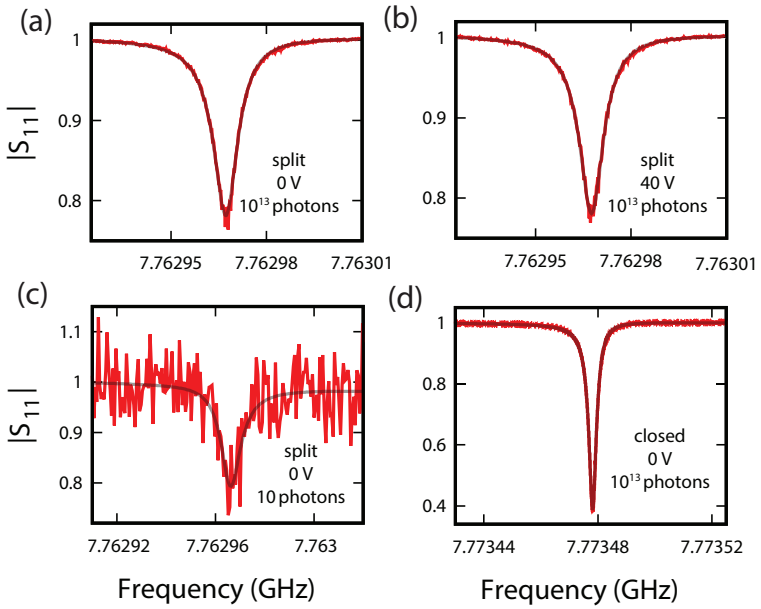

Figure 5.5: Characterization of the internal losses of a split cavity at 16 mK inside a dilution refrigerator. Reflection coefficient measurement of a split cavity separated by 100 μm Kapton tape at $P_{\text{in}} = -30$ dBm and a DC voltage of 0 V (a) and 40 V (b) with a quality factor $Q_{\text{i}} = 8.75 \pm 0.03 \times 10^5$ and $Q_{\text{i}} = 8.82 \pm 0.03 \times 10^5$, respectively. (c) A reflection measurement at $P_{\text{in}} = -148$ dBm (average photon occupation $N = 10$), with $Q_{\text{i}} = 8 \pm 1 \times 10^5$. (d) Reflection measurement of a closed cavity at $P_{\text{in}} = -30$ dBm showing an intrinsic quality factor $Q_{\text{i}} = 2.748 \pm 0.001 \times 10^6$. Black transparent lines indicate fits to the data.

compared to the quality factor of the cavity without diode at room temperature. The loaded quality factor is $Q_L \approx 2084$ at 0 V and $Q_L \approx 2292$ at 30 V. From the circuit diagram in Fig. 5.4(c) we can derive $\omega_0^{-2} = L(C + (1/C_c + 1/C_d)^{-1})$, where $\omega_0 = 2\pi f_0$. Assuming $C_d \gg C_c$, rewriting $1/\omega_0^2$ as y and $1/C_d$ as x, the above equation can be rearranged into a linear equation $y = L(C + C_c) - LC_c^2 x$. Using the value of C_d corresponding to each V provided by the diode data sheet, we plot $1/f_0^2$ as a function of $1/C_d$ and perform a linear fit as shown in Fig. 5.4(e). We further approximate the value of the characteristic impedance $Z_0 = \sqrt{L/C}$ to be $Z_{TE101} \approx 540\ \Omega$, and obtain the following parameters: $L \approx 10$ nH, $C \approx 35$ fF, $C_c \approx 6.65$ fF.

CRYOGENIC MEASUREMENTS

To investigate the feasibility of the split-cavity technique for quantum experiments, in Fig. 5.5 we show the response of a split-cavity design made from 6061 aluminum alloy measured at a temperature of 16 mK. Kapton tape of 100 μm thick was used to galvanically isolate the two halves of the cavity. Fig. 5.5(a) shows the reflection coefficient without any voltage bias, and Fig. 5.5(b) shows the same when applying 40 V. Both measurements reveal similar quality factors, $Q_i = 8.75 \pm 0.03 \times 10^5$ and $Q_i = 8.82 \pm 0.03 \times 10^5$, respectively, where the errors are statistical errors from the fit. Although the internal quality factor from such fits, determined by the depth of the dip in the reflection coefficient, can be include systematic error from cable reflections, we also estimate a lower bound of the internal quality factor from the loaded quality factor obtained from the resonance linewidth. For all cryogenic measurements reported here, we find a lower bound of $Q_i > 7.5 \times 10^5$. Fig. 5.5(c) shows a measurement at a cavity input power $P_{in} = -148$ dBm (10 photons) with a fit that corresponds to an intrinsic quality factor of $Q_i = 8 \pm 1 \times 10^5$. This independence of internal losses to input power has been observed in previous experiments and is one of the key advantages of 3D cavities over planar resonators [14]. For the closed cavity with no Kapton tape, we find an intrinsic quality factor $Q_i = 2.748 \pm 0.001 \times 10^6$. Although the split cavity has a smaller quality factor, the reported $Q_i > 7.5 \times 10^5$ is sufficient to enable sensitive quantum experiments in a 3D microwave architecture.

5.4. CONCLUSION

We have demonstrated a simple method of applying a DC bias up to 40 V in a 3D microwave cavity that maintains a high quality factor. We show that the intrinsic quality factor can be as high as $Q_i = 8.75 \pm 0.03 \times 10^5$ at dilution refrigerator temperatures, making it suitable for use in 3D implementations of microwave nano and quantum devices.

5.5. APPENDIX: CRYOGENIC MEASUREMENTS

Cryogenic measurements were done inside of a Triton dilution refrigerator. A picture showing the loading chamber containing the split-cavity is shown in Fig. 5.6. The cavity was split by Kapton tape which offers electrical insulation but relatively high thermal conductivity. The half with the SMA connection for the reflection measurement was

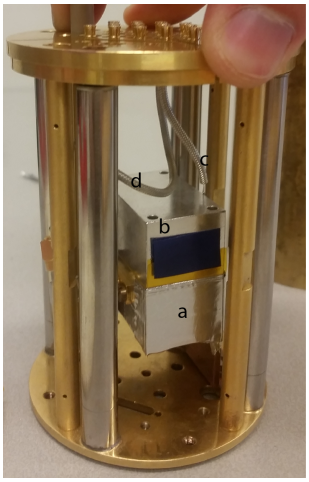

Figure 5.6: Photograph of wiring setup while performing cryogenic characterization of the split-cavity design. Label (a) shows the bottom half of the split cavity design, which is grounded and thermally anchored by a copper block in the background. Label (b) shows the top half, which is completely floating, except for a galvanic connection to the center pin of a coax as shown by label (c). The reflection measurement is done through wire labelled (d) which connects to the bottom half of the cavity with an SMA connector.

electrically grounded and thermally anchored with a copper block attached to the bottom plate. The other cavity half was floating and attached to the center pin of another coax which supplied the DC bias. The coaxial cables were made of gold-plated copper-beryllium. Before cooling down the setup, we first test the conductive paths of the cables using a multimeter to make sure everything is sufficiently galvanically connected.

Fig. 5.7 shows a graph of all the DC measurements taken. From 0 to 40 V the quality factor has a flat trend, which demonstrates the independence of DC voltage to internal losses of the split cavity.

A second measurement sweep was performed in which the input power to the cavity was modulated. Fig. 5.8 shows two of such data points, along with their fits. The fact that these data points can almost perfectly be overlayed shows that there equally is no dependence on input power to the internal losses of the cavity design.

5.6. APPENDIX: FITTING PROCEDURE

We start by unwrapping the phase, which corresponds to eliminating the electrical length of the cables running to the inside of the dilution refrigerator. The second step is to rotate the quadratures so that the real part purely represents the dissipative component and the imaginary part purely represents the dispersive component of the response. Along with this rotation the response is scaled such that off-resonance the reflection is unity. Lastly, the response is fitted using a least-squares method with the following formula:

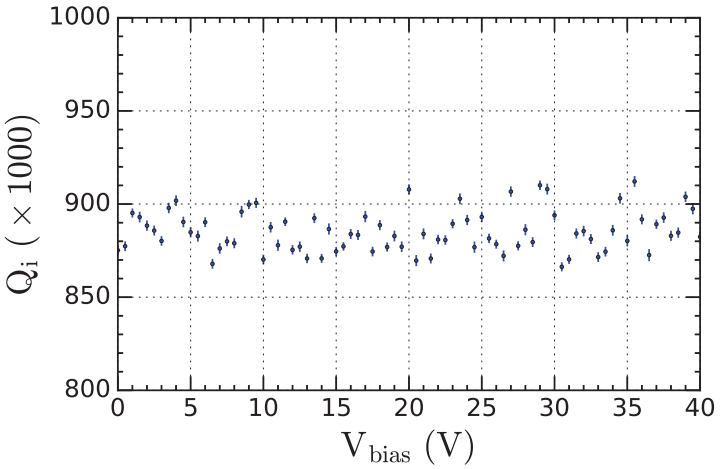

Figure 5.7: Graph of all intrinsic quality factor measurements as a function of bias voltage. Error bars indicate the fitting error.

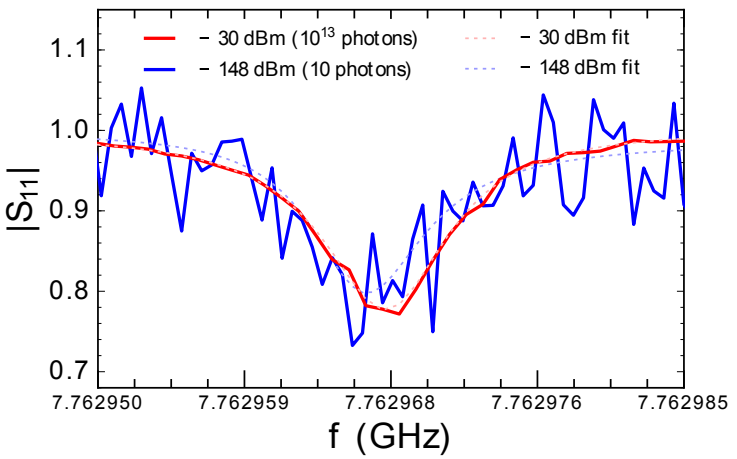

Figure 5.8: Graph overlaying reflection measurements at input powers of -30 dBm and -148 dBm, along with their fits.

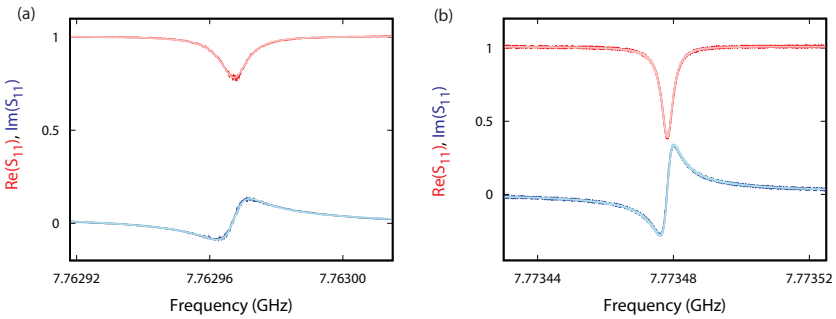

Figure 5.9: S_{11} measurements of split cavities. Shown are the real and imaginary quadratures of the S_{11} parameter of the aluminum cavity in (a) split geometry and (b) closed geometry. Derived values can be read from Table S1. Lighter lines indicate the fit.

$$S_{11}(\omega) = \frac{2\kappa_e e^{i\theta}}{\kappa + 2i(\omega - \omega_0)} - 1 \tag{5.1}$$

The exponential factor in the numerator approximates the asymmetric lineshape one would see when parasitic reflections interfere significantly (i.e. a Fano lineshape). In the case of very large cable resonance and strongly overcoupled cavities, there can be offsets of the quadratures that we cannot systematically eliminate from the fit, leaving systematic error in the extraction of Q_i from the data. On the other hand, from the rotated quadratures plotted in Fig. 5.9, one can reliable extract the loaded quality factor Q_L from the resonance linewidth. In this case, we can then place a conservative lower bound on Q_i given by Q_L. Table 5.1 states all the components for the quality factors for the split and closed cavities measured at cryogenic temperatures, along with Fig. 5.9 showing the fits in quadrature format.

Cavity state	Q_i	Q_e	Q_L
Split	$8.75 \pm 0.03 \times 10^5$	$7.04 \pm 0.02 \times 10^6$	$7.79 \pm 0.03 \times 10^5$
Closed	$2.748 \pm 0.001 \times 10^6$	$6.242 \pm 0.001 \times 10^6$	$1.908 \pm 0.001 \times 10^6$

Table 5.1: Quality factor measurements of our aluminium cavity in open and split configurations. The split is created by 100 μm Kapton tape.

REFERENCES

[1] H. Paik, D. Schuster, L. S. Bishop, G. Kirchmair, G. Catelani, A. Sears, B. Johnson, M. Reagor, L. Frunzio, L. Glazman, *et al.*, *Observation of high coherence in josephson junction qubits measured in a three-dimensional circuit qed architecture,* Physical Review Letters **107**, 240501 (2011).

[2] G. Kirchmair, B. Vlastakis, Z. Leghtas, S. E. Nigg, H. Paik, E. Ginossar, M. Mirrahimi, L. Frunzio, S. M. Girvin, and R. J. Schoelkopf, *Observation of quantum state collapse and revival due to the single-photon kerr effect,* Nature **495**, 205 (2013).

[3] S. Novikov, J. Robinson, Z. Keane, B. Suri, F. Wellstood, and B. Palmer, *Autler-townes splitting in a three-dimensional transmon superconducting qubit,* Physical Review B **88**, 060503 (2013).

[4] D. Riste, M. Dukalski, C. Watson, G. De Lange, M. Tiggelman, Y. M. Blanter, K. Lehnert, R. Schouten, and L. DiCarlo, *Deterministic entanglement of superconducting qubits by parity measurement and feedback,* Nature **502**, 350 (2013).

[5] L. Sun, A. Petrenko, Z. Leghtas, B. Vlastakis, G. Kirchmair, K. Sliwa, A. Narla, M. Hatridge, S. Shankar, J. Blumoff, L. Frunzio, M. Mirrahimi, M. Devoret, and R. Schoelkopf, *Tracking photon jumps with repeated quantum non-demolition parity measurements,* Nature **511**, 444– (2014).

[6] E. Flurin, N. Roch, J.-D. Pillet, F. Mallet, and B. Huard, *Superconducting quantum node for entanglement and storage of microwave radiation,* Physical review letters **114**, 090503 (2015).

[7] M. Reagor, W. Pfaff, C. Axline, R. W. Heeres, N. Ofek, K. Sliwa, E. Holland, C. Wang, J. Blumoff, K. Chou, *et al.*, *Quantum memory with millisecond coherence in circuit qed,* Physical Review B **94**, 014506 (2016).

[8] F. Chen, A. J. Sirois, R. W. Simmonds, and A. Rimberg, *Introduction of a dc bias into a high-q superconducting microwave cavity,* Applied Physics Letters **98**, 132509 (2011).

[9] S. J. Bosman, V. Singh, A. Bruno, and G. A. Steele, *Broadband architecture for galvanically accessible superconducting microwave resonators,* Applied Physics Letters **107**, 192602 (2015).

[10] S. E. de Graaf, D. Davidovikj, A. Adamyan, S. Kubatkin, and A. Danilov, *Galvanically split superconducting microwave resonators for introducing internal voltage bias,* Applied Physics Letters **104**, 052601 (2014).

[11] M. Yuan, V. Singh, Y. M. Blanter, and G. A. Steele, *Large cooperativity and microkelvin cooling with a three-dimensional optomechanical cavity,* Nature communications **6** (2015).

[12] W.-C. Kong, G.-W. Deng, S.-X. Li, H.-O. Li, G. Cao, M. Xiao, and G.-P. Guo, *Introduction of dc line structures into a superconducting microwave 3d cavity,* Review of Scientific Instruments **86**, 023108 (2015).

[13] T. Brecht, M. Reagor, Y. Chu, W. Pfaff, C. Wang, L. Frunzio, M. Devoret, and R. Schoelkopf, *Demonstration of superconducting micromachined cavities,* Applied Physics Letters **107**, 192603 (2015).

[14] M. Reagor, H. Paik, G. Catelani, L. Sun, C. Axline, E. Holland, I. M. Pop, N. A. Masluk, T. Brecht, L. Frunzio, *et al.*, *Reaching 10 ms single photon lifetimes for superconducting aluminum cavities,* Applied Physics Letters **102**, 192604 (2013).

6

OPTOMECHANICAL SIGNAL AMPLIFICATION WITHOUT MECHANICAL AMPLIFICATION

High-gain and low-noise signal amplification is a valuable tool in various cryogenic microwave experiments. A microwave optomechanical device, in which a vibrating capacitor modulates the frequency of a microwave cavity, is one technique that is able to amplify microwave signals with high gain and large dynamical range. Such optomechanical amplifiers typically rely on strong backaction of microwave photons on the mechanical mode achieved in the sideband-resolved limit of optomechanics. Here, we observe microwave amplification in an optomechanical cavity in the extremely unresolved sideband limit. A large gain is observed for any detuning of the single pump tone within the cavity linewidth, a clear indication that the amplification is not induced by dynamical backaction. By being able to amplify for any detuning of the pump signal, the amplification center frequency can be tuned over the entire range of the broad cavity linewidth. Additionally, by providing microwave amplification without mechanical amplification, we predict that using this scheme it is possible to achieve quantum-limited microwave amplification despite a large thermal occupation of the mechanical mode.

Parts of this chapter have been published to a public archive. Cohen, M. A., Bothner, D. J., Blanter, Y. M., Steele, G. A. (2018). Optomechanical amplification without mechanical amplification. arXiv:1812.05459.

6.1. INTRODUCTION

Amplification is an essential part of any measurement system where there is a need to distinguish a signal from noise. Cryogenic measurement systems for quantum experiments often use a high-electron-mobility transistor amplifier in their amplification chain [1–3]. However, they typically operate with higher added noise levels than the theoretical limit imposed by quantum mechanics, something readily achieved in the optical domain [4]. Josephson junction based microwave amplifiers [5, 6], on the other hand, can have quantum-limited noise and have been used to entangle superconducting qubits [7], to convert quantum states to mechanical motion [8], and to implement error-correction in quantum circuits [9]. In such amplifiers, a Josephson junction is used as a low-loss nonlinear element that enables parametric amplification driven by an external pump tone.

A mechanically compliable capacitor coupled through radiation pressure to a superconducting circuit [2, 10] – a microwave optomechanical system – can also be used as a nonlinear circuit and can create a microwave amplifier [11]. A Josephson parametric amplifier (JPA) typically has a strong x^3 Kerr (Duffing) nonlinearity in the restoring force in the equation of motion for parametric amplification (where the coordinate x for a JPA would refer to the phase difference across the junction). Although the Kerr nonlinearity is not necessary for amplification, it can result in amplifier saturation already at 100 photons [12, 13].

In optomechanical amplification cubic nonlinearities are weak compared to a JPA. Typical schemes operate by driving the optomechanical system at a frequency positively detuned from the cavity frequency (blue-sideband driving): doing so, one can produce amplification analogous to a non-degenerate two-mode amplifier, where the cavity mode and mechanical mode act as signal and idler, respectively [11]. With mechanical frequencies in the MHz range, it is then neccessary to cool the mechanical element to $< 50\mu$K such that the microwave amplification is not dominated by thermal noise and the amplifier can approach the quantum limit. A more recent optomechanical microwave amplification scheme has approached this problem by using two pump tones, a red-detuned tone to provide cooling to the mechanical mode and a blue-detuned one to provide amplification, either in one cavity [14, 15], or in two separate cavity modes coupled to one mechanical mode [13].

Here, we present an observation of amplification of cavity fields mediated by a mechanical oscillator which, in contrast to earlier works [11], does not make use of dynamical backaction, and results in no amplification of the mechanical motion. Strikingly, we observe optomechanical microwave amplification in the presence of a drive tone red-detuned from the cavity resonance frequency, a regime associated with mechanical damping and not amplification. The amplification mechanism observed does not rely on dynamical backaction, and results in no amplification of the mechanical motion. Based on the mechanism we identify, we predict that the amplification presented here has the potential to amplify microwave signals with only quantum-limited added noise, even in the presence of large thermal occupations of the mechanical resonator without cooling of the mechanical mode.

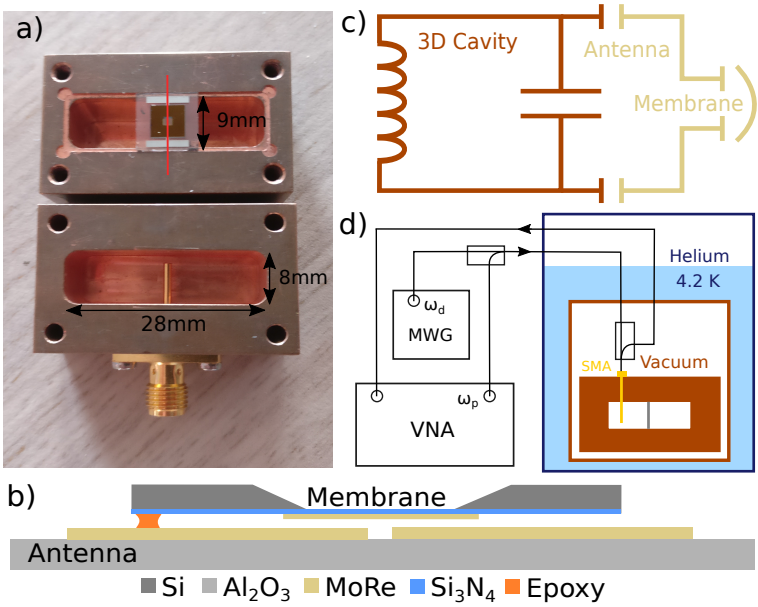

Figure 6.1: A 3D optomechanical cavity in the sideband-unresolved regime at 4K. (a) A photograph of the copper 3D cavity used in this experiment. The inner dimensions of the cavity correspond to $28 \times 28 \times 8$ mm^3 and microwave signals are coupled in an out using a single SMA connector. The depth of the pin determines the external coupling. The red line through the chip shows the cross-section shown in (b). This cross-section shows the thin film layers of the antenna chip and membrane chip. The membrane chip is a 50 nm thick silicon nitride window with 20 nm thick MoRe alloy sputtered on top. The antenna chip is made from double side-polished sapphire with 100 nm thick MoRe antennas patterned on top. The two chips are fixed together with a single drop of epoxy in one corner. (c) A circuit diagram which corresponds to the optomechanical system. The fundamental mode of the 3D cavity is represented by an LC resonator, and the antennas act as capacitors which concentrate the electric field towards the membrane, which itself can be represented as a mechanically compliable capacitor. The membrane motion modulates the resonance frequency of the 3D cavity. (d) We put the 3D optomechanical setup inside a vacuum can and cool it to 4.2 K in liquid helium. Using two directional couplers we probe the cavity by means of a vector network analyzer (VNA) while simultaneously sending a drive signal with a microwave generator (MWG).

6.2. DEVICE DESIGN AND FABRICATION

The experimental setup is shown in Fig. 6.1. As microwave cavity we use a 3D copper cavity with dimensions $28 \times 28 \times 8$ mm^3 with a bare frequency of 7.59 GHz. We fabricated the antenna chip and membrane chip separately [16, 17]. The antenna chip was made from double-side polished sapphire 420 μm thick and it was pre-cleaned using a Piranha solution – H_2SO_4 and H_2O_2 in (3:1) concentration, heated to 80° C for roughly 10 minutes. We sputter-deposited 100 nm of Molybdenum-Rhenium alloy (MoRe 60/40) [18] and spun AZ ECI 3007 photoresist. The antennas were patterned using a Durham Magneto Optics Microwriter ML-2 laserwriter and the remaining MoRe was then etched away using an SF_6/He plasma. The photoresist was stripped using warm N-Methyl-2-pyrrolidone (NMP).

The membrane chip was metalized using a lift-off method because we had adhesion issues when spinning photoresist onto a MoRe-coated membrane. The photoresist would crack off which we believe is because the membrane was an unstable surface which could move when the photoresist would be developed. We patterned using a negative photoresist – AZ 5214E – and sputtered 20 nm of MoRe. We made sure that the patch overlapped with the frame of the Norcada membrane to induce mechanical losses and increase the amplification bandwidth[19]. The lift-off procedure was then also performed using warm NMP. We flipped the two chips on top of each other and fixed them by using a small drop of epoxy on the corner of the membrane chip. We would wait an hour until we were sure the drop of glue was healed.

The microwave optomechanical system can be understood using the effective circuit diagram in Fig. 6.1(c). The fundamental mode of the 3D cavity is represented by an LC circuit, and the antenna-chip structure is a capacitive circuit in which the middle two capacitors are modulated in-phase by the motion of the membrane. We measure the 3D optomechanical setup in vacuum with a bath temperature of 4.2 K by means of a microwave reflection measurement using an Agilent PNA N5221A vector network analyzer (VNA). In the case that measurements require two microwave tones, a weak probing tone, with frequency ω_p, is provided by the output port of our VNA, and a second stronger drive tone, with frequency ω_d, is generated by a Rohde & Schwarz SMB100A microwave generator. The signals are combined using a directional coupler where the transmitted port is used for the drive tone to allow for maximum drive power.

6.3. ESTIMATING COUPLING CONSTANT

We estimate the optomechanical coupling constant using finite element model simulations in COMSOL. We recreate the geometry of our chip by including a sapphire chip with a thickness of 430 μm, on top of which we patterned our antennas. In between the arms of the antennas we put a 1×1 mm metal square which corresponds to the metalized membrane, as sketch of which can be seen in Fig. 6.2. Even though the geometry of the capacitance between the antennas and cavity walls is different in the COMSOL model due to computational ease, we compensate for this by decreasing the gap between the antennas and the wall such that the resonance frequency of the entire structure matches what we measured empirically. We can use the following formula to derive the coupling

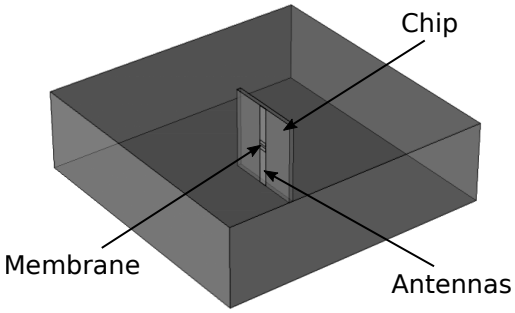

Figure 6.2: A figure showing the geometry of our COMSOL simulation. The chip in the middle contains two antennas and a membrane in the center which approximates our capacitive circuit. The gap of the membrane is modulated to calculate the coupling constant.

constant

$$g_0 = \frac{d\omega_0}{dx} x_{\text{zpf}} \tag{6.1}$$

where $\frac{d\omega_0}{dx}$ is the rate of change of the cavity resonance frequency with respect to the membrane gap. x_{zpf} corresponds to the zero point fluctuations of the mechanical oscillator and can be calculated by $x_{\text{zpf}} = \sqrt{\frac{\hbar}{2m\Omega_{\text{m}}}}$ which for our MoRe-coated membrane is 0.28 fm. We determine the rate of change of the cavity by simulating the resonance at two points around the estimated membrane gap of 2 μm and arrive at $\frac{d\omega_0}{dx} \approx 246$ kHz/nm. This results in a coupling strength $g_0/2\pi \approx 0.069$ Hz.

6.4. NORMALIZATION OF BACKGROUND SIGNAL

Before we fit and extract data from the reflection measurement, we have to fit the background signal. For this we use a complex polynomial as an approximation

$$S_{11,\text{b}}(\omega) = (a + b\omega + c\omega^2)e^{i(a' + b'\omega)} \tag{6.2}$$

where all variables except ω are fitting constants. When fitting the full cavity response we first extract the resonance frequency and eliminate it from the data. We then make a preliminary fit of this modified data. Using the fit parameters for the complex polynomial above, we then refit the raw data using both the background and a Lorentzian for the cavity response using the following formula

$$S_{11}(\omega) = S_{11,\text{b}}(\omega) \times \left(\frac{2\kappa_{\text{e}} e^{i\theta}}{\kappa_{\text{e}} + \kappa_{\text{i}} - 2i(\omega - \omega_0)} - 1 \right) \tag{6.3}$$

where, again, all variables except ω are fitting constants. Figure 6.3 shows the raw data with both fits.

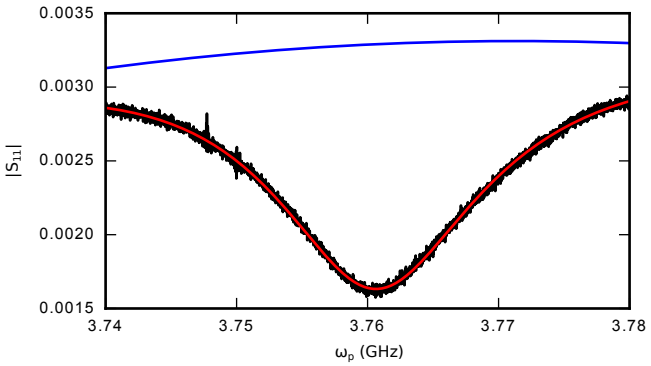

Figure 6.3: A reflection measurement of the cavity response in linear units. The data in black is the raw signal, blue signifies the background fit, and red is the total fit.

6.5. RESULTS AND DISCUSSION

Figure 6.4 shows a characterization of the optomechanical system. The cavity resonant frequency is found to be $\omega_0/2\pi = 3.76$ GHz, with a linewidth of $\kappa/2\pi = 23.5$ MHz, (intrinsic losses $\kappa_i/2\pi = 17.6$ MHz, external losses $\kappa_e/2\pi = 5.9$ MHz) which results in a relatively low quality factor of $Q = 160$ compared to other microwave optomechanical amplification devices. A reflection measurement of the cavity resonance including a fit line is shown in Fig. 6.4(a). The cavity is undercoupled, as $\eta = \kappa_e/\kappa = 0.25$. To measure the mechanical resonance, a two-tone measurement scheme called optomechanically induced reflection (OMIR), an analogue of optomechanically induced transparency [20] in a reflection geometry is used, illustrated in Fig. 6.4(b). A strong drive tone is applied at the cavity resonance frequency, and a second weak probe tone is swept around a range of frequencies detuned by the mechanical frequency from the drive tone. We define a detuning $\Delta = \omega_d - \omega_0$ between the drive frequency ω_d and the cavity resonance frequency, as well as a detuning $\Omega = \omega_p - \omega_d$ between the drive frequency and the probe frequency ω_p. When $\Omega = \pm\Omega_m$, an interference effect in the measured reflection at the probe frequency is observed, shown in Fig. 6.4 for the case where $\Omega = -\Omega_m$. In the measurement, the mechanical resonance is excited by the oscillating radiation pressure from the beating of the pump and drive tones, which then creates a sideband of the drive tone which interferes with the probe field. Using this technique, we find a mechanical frequency of $\Omega_m/2\pi = 228.65$ kHz and damping rate $\gamma_m/2\pi = 22.0$ Hz. From the ratio $\kappa/\Omega_m = 103$, the system is found to be deep in the sideband-unresolved limit, illustrated in Fig. 6.4(a) and (b). We also estimate our coupling constant $g_0 = 69$ mHz using finite element simulations.

Figure 6.5(a) shows a measurement similar to that in Fig. 6.4(c) but now with $\Delta/2\pi = -3$ MHz and higher drive power. Strikingly, we observe that the reflection coefficient goes significantly above one, indicating that there is microwave amplification of 13 dB being performed by the system. This is surprising since in the usual paradigm in op-

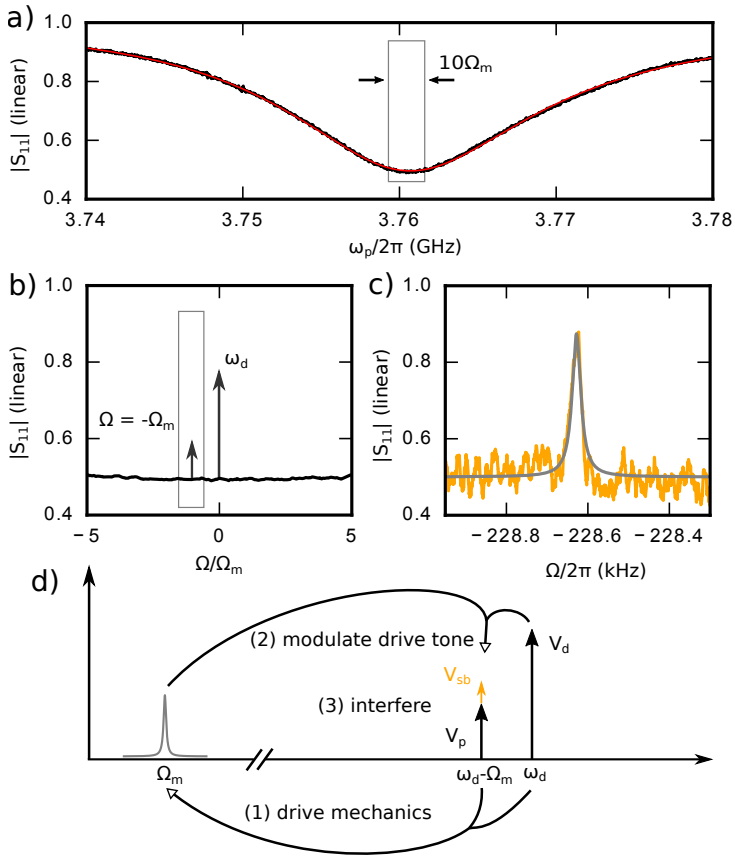

Figure 6.4: Optomechanically induced reflection (OMIR) in the sideband-unresolved regime. (a) A reflection measurement of the copper cavity, black dots show raw data and red line a fit. The fit result in a center frequency of $\omega_0/2\pi = 3.76$ GHz and a linewidth of $\kappa/2\pi = 23.5$ MHz. The grey rectangle is zoomed in on panel (b) and shows the width of 10 mechanical frequencies, $10\Omega_m$, a visual demonstration that the optomechanical system is deep in the sideband-unresolved regime. The curve is normalized to a background level detuned from the resonance. (b) Experimental scheme: We send a strong drive tone at $\omega_d = \omega_0$ ($\Delta = 0$) and sweep a weak additional probe tone around one mechanical frequency detuned from the drive tone, here $\omega_p - \omega_d = \Omega \approx -\Omega_m$. The grey box is zoomed-in in the next subfigure. (c) A sample reflection measurement that we obtain when driving at low power. What results is an OMIR interference effect. (d) A diagram which shows the basic mechanism of the observed effect. (1) The probe and the drive tone interfere, causing a beating pattern which oscillates at the mechanical frequency. By means of radiation pressure, this coherently drives the mechanical resonator. (2) The coherent oscillations of the mechanical oscillator then in turn modulate the cavity frequency which phase modulates the drive tone, creating sidebands at $\pm\Omega_m$. (3) The sideband and the probe tone interfere, which gives rise to OMIR. Note that there is no cooling or amplification of the mechanical oscillator when $\Delta = 0$.

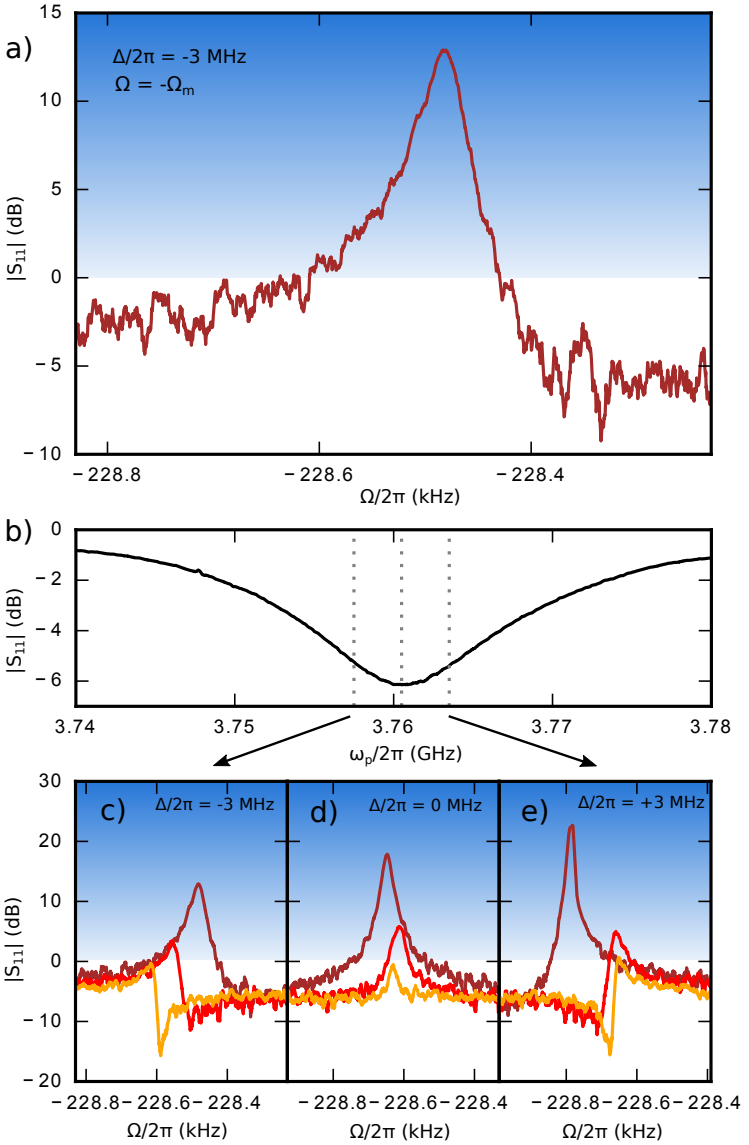

Figure 6.5: Optomechanical microwave amplification with negative probe detuning. (a) A reflection measurement when the drive detuning $\Delta/2\pi = -3$ MHz at -11 dBm, and probe detuning $\Omega = \omega_p - \omega_d = -\Omega_m$ showing gain up to 13 dB. (b) The experimentally determined cavity resonance with three vertical lines indicate the positions for the three drive detunings $\Delta_1/2\pi = -3$ MHz, $\Delta_2/2\pi = 0$ MHz, $\Delta_3/2\pi = +3$ MHz used in (c), (d), (e), respectively. (c)-(e) Probe sweeps of the lower sideband $\omega_p \approx \omega_0 - \Delta_i - \Omega_m$ for three different drive tone powers, -11 dBm (brown), -15 dBm (red), -19 dBm (orange), showing probe tone gain for all three chosen detunings. The cavity resonance shift slightly with respect to drive power and detuning. The responses are normalized such that a signal above 0 dB corresponds to gain > 1. The highest gain is observed when the drive detuning is positive, which shows that dynamical backaction does play a contributing role. One can also see an asymmetric Fano lineshape when the detuning is non-zero.

tomechanics, a negative detuning results in damping and not amplification: a strong indication that dynamical backaction is not the origin of the observed microwave gain.

We can understand the origin of the observed microwave amplification qualitatively using the illustration in Fig. 6.4(d) and looking at how the amplitudes of the different signals change when increasing the amplitude of the drive tone V_d at ω_d while keeping the amplitude of the probe signal V_p constant. The amplitude of the mechanical motion, indicated by the height of the arrow Ω_m is proportional to the product of the probe and the drive tone amplitudes; increasing the drive power will drive the mechanical resonator to a large coherent amplitude. The drive tone mechanical sideband amplitude V_{sb} has a height that is proportional to both the mechanical amplitude and the drive amplitude V_d. Consequently, the sideband of the drive, V_{sb}, will be proportional to V_d^2. For sufficiently large drive powers, V_{sb} will become larger than V_p: if they add in phase, this will then give maximum amplification.

One way to think about this amplification process is as a frequency mixing process, where the drive tone is not only down-converting the signal, but also amplifies it. In this sense, this amplification process can be thought of as a "double mixer amplifier". Note that this "double mixer" process does not make use of dynamical backaction [10], and also does not result in any mechanical amplification. For $\Delta = 0$, there is only coherent driving of the mechanical oscillator with no damping or amplification, while when $\Delta < 0$ both mechanical cooling and microwave amplification are attained simultaneously with a single drive tone. The fact that microwave amplification can occur without mechanical amplification also potentially enables quantum-limited amplification even if the mechanical resonator is not cooled to the ground state. The quantum-limited regime is reached in the optomechanical mixing amplification scheme when V_d is large enough such that the first step of the mixing amplification, corresponding to the radiation pressure driving of the mechanical resonator, results in translation of the quantum noise of the input probe field to an amplitude that is larger than the thermal noise of the mechanical mode. Quantum limited operation becomes possible for cooperativities $C > kT_m/\hbar\Omega_m = n_{th}$ for an optimal amplifier configuration, corresponding to the criteria of reaching the radiation pressure shot noise limit where the quantum fluctuation of the input field dominate the force noise of the mechanical resonator.

Figure 6.5(c)-(e) show the microwave responses for different detunings Δ, illustrated in Fig. 6.5(b). We observe that the gain depends on detuning, with the largest amplification occurring for positive Δ. This indicates that there is also a contribution from dynamical backaction in these measurements, reducing the gain for $\Delta < 0$ and providing additional gain for $\Delta > 0$. The data also show a shift of the mechanical frequency for $\Delta \neq 0$ due to the optical spring effect, confirming the presence of dynamical backaction. We note however that this dynamical backaction is not needed for the amplification: amplification also occurs at $\Delta = 0$ in the absence of dynamical backaction, and for $\Delta < 0$ in spite of mechanical damping from dynamical backaction. We believe that previous works with two-tone schemes for optomechanical amplification in the sideband-resolved regime [13, 14] also work on a similar amplification principle as the process described here, and dynamical backaction amplification of the mechanics is avoided by

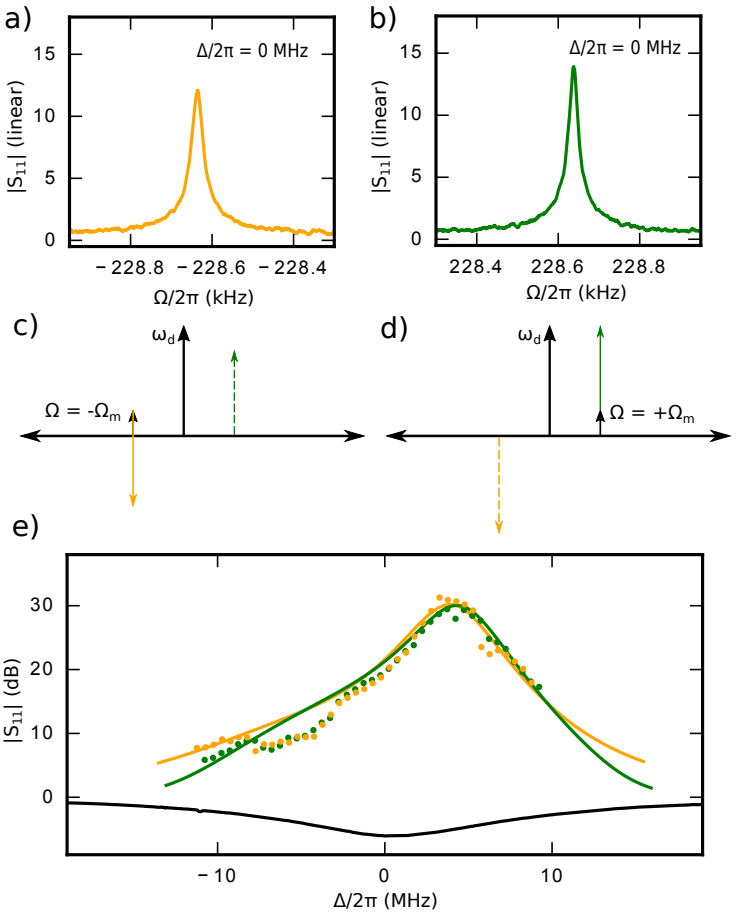

Figure 6.6: Understanding the mechanism of amplification and how the gain depends on probe and drive detuning. (a)-(b) Reflection spectra taken with a -9 dBm drive on cavity resonance and with the probe at the lower drive sideband $\Omega = -\Omega_m$ in (a), and the probe at the upper drive sideband $\Omega = +\Omega_m$ in (b). Note that the maximum gain differs between the sidebands. (c)-(d) A more precise explanation of the interference effect, idealized for when the drive detuning is zero, $\Delta = 0$. The phase modulations of the drive tone produce sidebands which have opposite phase and thus interfere constructively or destructively depending on which sideband is probed. This is why one gets a slightly lower gain for $\Omega = -\Omega_m$ (c) and slightly higher gain for $\Omega = +\Omega_m$ (d). (e) We performed a sweep of varying drive detunings, Δ, and measured the maximum gain value at constant drive power for both the upper and lower drive sidebands, in yellow and green, respectively. Dots show experimental data points and lines show the result of theoretical calculations. As one might expect, the gain is the highest when there is a positive contribution from dynamical backaction.

balancing the backaction from the blue and red drive tones.

In Fig. 6.6, we explore in detail the dependence of the gain on detuning Δ of the drive tone from the cavity resonance, for both positive and negative $\Omega = \pm\Omega_m$, respectively. Note that in the sideband-resolved limit $\kappa < \Omega_m$, features corresponding to Ω and Δ having the same sign are usually not accessible experimentally as they correspond to features far outside the cavity resonance. However in the case $\kappa \gg \Omega_m$, both of these features are accessible and can be equally strong. Figure 6.6(a) and (b) show the reflection coefficient of the cavity for $\Delta = 0$ and for positive and negative Ω, respectively. It is interesting to note that the gain is larger for $+\Omega_m$ than for $-\Omega_m$. This can be understood by the fact that with a drive on cavity resonance the up-converted mechanical sidebands of the drive tone have opposite phase compared to the probe signal, as shown in (c) and (d). This asymmetry in (a) and (b) can then be understood as arising from the difference in constructive and destructive interference of the probe and the sideband, as shown in (c) and (d). Fig. 6.6(e) shows the dependence of the observed and theoretically calculated gain for positive (green) and negative (orange) Ω as a function of drive-cavity detuning Δ. Due to the additional gain from dynamical backaction, the gain is maximum for positive drive detuning, but is still larger than unity for all detunings when the drive is sufficiently strong. We also note that there are several transitions where the relative amplitudes of positive and negative $\Omega = \pm\Omega_m$ changes sign (crossing of the green/yellow curves in Fig. 6.6(e)), which is a result of changes in the relative phase of the sidebands as a function of detuning.

6.6. CONCLUSION

In conclusion, we have demonstrated microwave amplification in an optomechanical system which does not depend on dynamical backaction. Since our amplification scheme works even in the sideband-unresolved limit, we are able to center the amplification window over a relatively wide cavity linewidth. Futhermore, since the thermal noise of the mechanical mode is not amplified, this method could achieve quantum-limited microwave amplification without the necessity to cool the mechanical oscillator.

6.7. APPENDIX: DERIVATION OF FULL EQUATIONS OF MOTION

Much of this derivation has already been covered in chapter 2, but we recapitulate it here for clarity. We start by citing the classical optomechanical equations of motion as derived throughout literature in the field of optomechanics [10, 20]

$$\ddot{x} = -\Omega_m^2 x - \Gamma_m \dot{x} + \frac{\hbar G}{m}|\alpha|^2 \tag{6.4}$$

$$\dot{\alpha} = i(\Delta + Gx)\alpha - \frac{\kappa}{2}\alpha + \sqrt{\kappa_e}s_d \tag{6.5}$$

The first equation describes the displacement x of the mechanical oscillator, the second describes the intracavity field amplitude α. In the first equation, Ω_m is the resonance frequency of the mechanical oscillator, Γ_m is the mechanical damping rate and

m is the effective mass of the mechanical oscillator. The last term is the radiation pressure force, where $G = -\partial\omega_0/\partial x$ is the cavity pull parameter. In the second equation the light field amplitude α is normalized such that $|\alpha|^2$ is the photon number in the cavity, $\Delta = \omega_d - \omega_0$ denotes the detuning between the drive frequency ω_d and the cavity resonance frequency ω_0. κ is the total cavity linewidth and κ_e is the external coupling constant. s_d is an input drive signal.

We assume now that a static equilibrium solution exists with $\dot{x} = \dot{\alpha} = 0$ and $x = \bar{x}$ and $\alpha = \bar{\alpha}$. We find from the equations of motion

$$\bar{x} = \frac{\hbar G}{m\Omega_m^2}|\bar{\alpha}|^2 \tag{6.6}$$

$$\bar{\alpha} = s_d \frac{\sqrt{\kappa_e}}{\frac{\kappa}{2} - i\bar{\Delta}} \tag{6.7}$$

where $\bar{\Delta} = \omega_d - \omega_0 + G\bar{x}$. (Note that in the main text we simplify by using Δ when in reality we mean $\bar{\Delta}$.) Secondly, we assume that it is sufficient to consider small deviations from this equilibrium solution and set $\alpha = \bar{\alpha} + \delta\alpha$ and $x = \bar{x} + \delta x$. We linearize the equations of motion and throw away quadratic terms in δx and $\delta\alpha$. We arrive at the two coupled, linearized equations

$$\delta\ddot{x} = -\Omega_m^2\delta x - \Gamma_m\delta\dot{x} + \frac{\hbar G\bar{\alpha}}{m}(\delta\alpha + \delta\alpha^*) \tag{6.8}$$

$$\delta\dot{\alpha} = \left[i\bar{\Delta} - \frac{\kappa}{2}\right]\delta\alpha + iG\bar{\alpha}\delta x + \sqrt{\kappa_e}s_p \tag{6.9}$$

where we assume that $\bar{\alpha}$ is real and where the last term accounts for small additional probe fields $s_p = s_0 e^{-i\Omega t}$ with the difference between the probe and drive frequency $\Omega = \omega_p - \omega_d$ in the frame rotating with ω_d.

To solve the equations, we use the ansatz

$$\delta\alpha = a_- e^{-i\Omega t} + a_+ e^{+i\Omega t} \tag{6.10}$$

$$\delta\alpha^* = a_-^* e^{+i\Omega t} + a_+^* e^{-i\Omega t} \tag{6.11}$$

$$\delta x = x_1 e^{-i\Omega t} + x_1^* e^{+i\Omega t} \tag{6.12}$$

and we keep only the terms resonant with the drive $\propto e^{-i\Omega t}$.

We get three equations

$$x_1[\Omega_m^2 - \Omega^2 - i\Omega\Gamma_m] = \frac{\hbar G\bar{\alpha}}{m}(a_- + a_+^*) \tag{6.13}$$

$$a_-\left[\frac{\kappa}{2} - i(\bar{\Delta} + \Omega)\right] = iG\bar{\alpha}x_1 + \sqrt{\kappa_e}s_0 \tag{6.14}$$

$$a_+^*\left[\frac{\kappa}{2} + i(\bar{\Delta} - \Omega)\right] = -iG\bar{\alpha}x_1 \tag{6.15}$$

Next, we remove a_+^* and x_1 from the first equation with the second and third and get for a_- the expression

$$a_- = \frac{1 + if(\Omega)}{\kappa/2 - i(\bar{\Delta} + \Omega) + 2\bar{\Delta}f(\Omega)}\sqrt{\kappa_e}s_0 \tag{6.16}$$

with

$$f(\Omega) = \frac{\hbar G^2 \bar{\alpha}^2}{\kappa/2 + i(\bar{\Delta} - \Omega)} \chi_{\mathrm{m}}(\Omega) \tag{6.17}$$

and the mechanical susceptibility

$$\chi_{\mathrm{m}}(\Omega) = \frac{1}{m(\Omega_{\mathrm{m}}^2 - \Omega^2 - i\Omega\Gamma_{\mathrm{m}})} \tag{6.18}$$

We can use input-output theory to use these equations to calculate a reflection coefficient at a single port cavity:

$$S_{11} = 1 - \sqrt{\kappa_{\mathrm{e}}} \frac{a_-}{s_0} \tag{6.19}$$

We calculate the reflection coefficient when there is no dynamical backaction by setting the drive tone resonant with the cavity frequency $\bar{\Delta} = 0$ and the probe detuning to negative and positive the mechanical frequency $\Omega = \pm\Omega_{\mathrm{m}}$

$$S_{11}(\bar{\Delta} = 0, \Omega = \pm\Omega_{\mathrm{m}}) = 1 - \frac{\kappa_{\mathrm{e}}}{\kappa/2 \mp i\Omega_{\mathrm{m}}} \pm C \frac{\kappa\kappa_{\mathrm{e}}/2}{(\kappa/2 \mp i\Omega_{\mathrm{m}})^2} \tag{6.20}$$

where $C = \frac{4g_0^2}{\Gamma_{\mathrm{m}}\kappa} n_{\mathrm{d}}$ is the multi-photon cooperativity. The first two terms are the typical cavity response function, while the last term is purely due to optomechanical interactions. We can further simplify by assuming we are deeply sideband-unresolved ($\kappa \gg \Omega_{\mathrm{m}}$) and using $\eta = \kappa_{\mathrm{e}}/\kappa$

$$S_{11}(\pm\Omega_m) = 1 - 2\eta \pm 2\eta C = 1 - 2\eta(1 \mp C) \tag{6.21}$$

which exceeds 1 in the limit $C \gg 1$, indicating amplification.

6.8. APPENDIX: DERIVATION OF MIXING PICTURE

We can derive Eq. (6.20) in a slightly different way to give more insight as to why this amplification occurs. Starting with mechanical displacement, we will do this in four steps.

MECHANICAL DISPLACEMENT

The radiation pressure force onto the mechanical oscillator due to an intracavity field is given by

$$F_r = \hbar G |\alpha|^2. \tag{6.22}$$

Assuming again that the intracavity field can be approximated by $\alpha = \bar{\alpha} + \delta\alpha$ with constant $\bar{\alpha}$ this reads

$$F_r \approx \hbar G |\bar{\alpha}|^2 + \hbar G(\bar{\alpha}^* \delta\alpha + \bar{\alpha}\delta\alpha^*) \tag{6.23}$$

where we once again omitted the term $\propto |\delta\alpha|^2$.

We get the mechanical displacement $\delta x = x - \bar{x}$ for a driving frequency $\Omega = \pm\Omega_{\mathrm{m}}$ from here by using the mechanical susceptibility Eq. (6.18) as

$$\delta x = \pm i\hbar G \frac{\bar{\alpha}^* \delta\alpha + \bar{\alpha}\delta\alpha^*}{m\Omega_\mathrm{m}\Gamma_\mathrm{m}} \tag{6.24}$$

or for a real-valued average amplitude $\bar{\alpha}$

$$\delta x = \pm i \frac{\hbar G\bar{\alpha}}{m\Omega_\mathrm{m}\Gamma_\mathrm{m}} \left(\delta\alpha + \delta\alpha^*\right) \tag{6.25}$$

EXCITING THE MECHANICAL OSCILLATOR

Next, we assume that we drive the cavity with a strong microwave tone s_in on resonance $\bar{\Delta} = 0$ and with a much smaller probe tone s_0 one mechanical frequency detuned from it $\Omega = \pm\Omega_\mathrm{m}$. The intracavity field to first order is then given by

$$\bar{\alpha} + \delta\alpha = 2\frac{\sqrt{\kappa_\mathrm{e}}}{\kappa} s_\mathrm{in} + \frac{\sqrt{\kappa_\mathrm{e}}}{\kappa/2 \mp i\Omega_\mathrm{m}} s_0 e^{\mp i\Omega_\mathrm{m} t}. \tag{6.26}$$

and the term relevant for the radiation pressure force by

$$\delta\alpha + \delta\alpha^* = \frac{\sqrt{\kappa_\mathrm{e}}}{\kappa/2 \mp i\Omega_\mathrm{m}} s_0 e^{\mp i\Omega_\mathrm{m} t} + \frac{\sqrt{\kappa_\mathrm{e}}}{\kappa/2 \pm i\Omega_\mathrm{m}} s_0 e^{\pm i\Omega_\mathrm{m} t} \tag{6.27}$$

We implicitly assumed here that s_0 is real-valued, fixing the phase between s_in and s_0 at $t = 0$.

From here, we can calculate x_1 and x_2 of $\delta x = x_1 e^{-i\Omega_\mathrm{m} t} + x_2 e^{+i\Omega_\mathrm{m} t}$ as

$$x_1 = \pm i \frac{\hbar G\bar{\alpha}}{m\Omega_\mathrm{m}\Gamma_\mathrm{m}} \frac{\sqrt{\kappa_\mathrm{e}}}{\kappa/2 \mp i\Omega_\mathrm{m}} s_0 \tag{6.28}$$

$$x_2 = \pm i \frac{\hbar G\bar{\alpha}}{m\Omega_\mathrm{m}\Gamma_\mathrm{m}} \frac{\sqrt{\kappa_\mathrm{e}}}{\kappa/2 \pm i\Omega_\mathrm{m}} s_0 \tag{6.29}$$

We note, that in this choice of phases we get $\delta x(+\Omega_\mathrm{m}) = -\delta x(-\Omega_\mathrm{m})$, i.e., for blue vs red detuned probe tone the mechanical oscillations are shifted by π with respect to each other. Also, due to fixing the phase of s_0 above, we cannot use the general approach $\delta x = x_1 e^{-i\Omega_\mathrm{m} t} + x_1^* e^{+i\Omega_\mathrm{m} t}$ as we have to allow for an additional phase shift. Here, we get as result $x_2 = -x_1^*$.

DRIVE SIDEBAND GENERATION

Now we assume the cavity is driven on resonance $\bar{\Delta} = 0$ with a single tone and that the mechanical resonator is oscillating with $\delta x(t) = x_1 e^{-i\Omega_\mathrm{m} t} - x_1^* e^{+i\Omega_\mathrm{m} t}$. From Eq. (6.14), we get for this case

$$a_{s-} = iG\frac{\bar{\alpha}}{\kappa/2 - i\Omega_\mathrm{m}} x_1 \tag{6.30}$$

$$a_{s+} = -iG\frac{\bar{\alpha}}{\kappa/2 + i\Omega_\mathrm{m}} x_1^*. \tag{6.31}$$

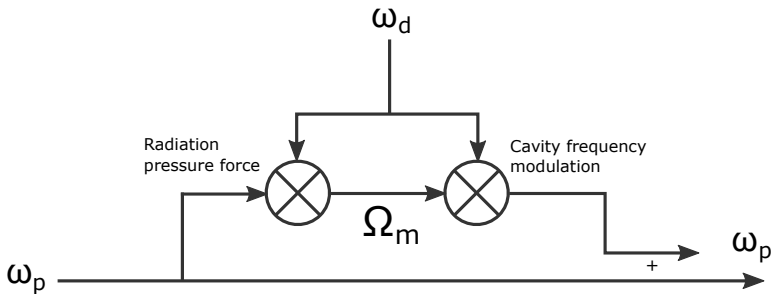

Figure 6.7: (a) A circuit diagram interpretation of the amplification mechanism. The amplification can be viewed as the effect of two frequency mixers – one which corresponds to the driving of the mechanics by the beating of the probe ω_p and drive ω_d, and one which is caused by the mechanical modulation of the cavity frequency. The result of the last mixing step creates sidebands of the drive tone, one of which interferes with the probe tone.

These two amplitudes correspond to the two sidebands to the resonant drive tone, which are generated by the mechanical motion. One sideband with amplitude a_{s+} is oscillating at $\omega_0 + \Omega_m$ and one with amplitude a_{s-} at $\omega_0 - \Omega_m$, cf. Eq. (6.10). As can be derived from the expressions, there is also a phase-shift of π between them, which means that $\delta\alpha_s + \delta\alpha_s^* = 0$ with $\delta\alpha_s = a_{s-}e^{-i\Omega_m t} + a_{s+}e^{+i\Omega_m t}$, i.e., that there is no dynamical backaction acting upon the mechanical oscillator when only considering a resonant drive and those two sidebands, cf. Eq. (6.8).

AMPLIFICATION FOR $\Omega = +\Omega_M$

Finally, we put the ingredients together. The mechanical oscillator is driven into a motional state with amplitude δx by a combination of a drive tone resonant with the cavity and a probe tone one mechanical frequency detuned. The resulting motion modulates the cavity frequency and generates sidebands to the drive tone, one of which interferes with the probe tone. The intracavity field at this frequency is then given by the interference of the probe tone amplitude and the sideband of the drive

$$a_- = \delta\alpha + a_{s-} = \frac{\sqrt{\kappa_e}}{\kappa/2 - i\Omega_m} s_0 - \frac{\kappa}{2} C \frac{\sqrt{\kappa_e}}{(\kappa/2 - i\Omega_m)^2} s_0 \tag{6.32}$$

The resulting microwave signal coming out of the cavity is an interference between the probe tone and the sideband at the same frequency and is calculated as

$$S_{11} = 1 - \frac{\kappa_e}{\kappa/2 - i\Omega_m} + C \frac{\kappa\kappa_e/2}{(\kappa/2 - i\Omega_m)^2} \tag{6.33}$$

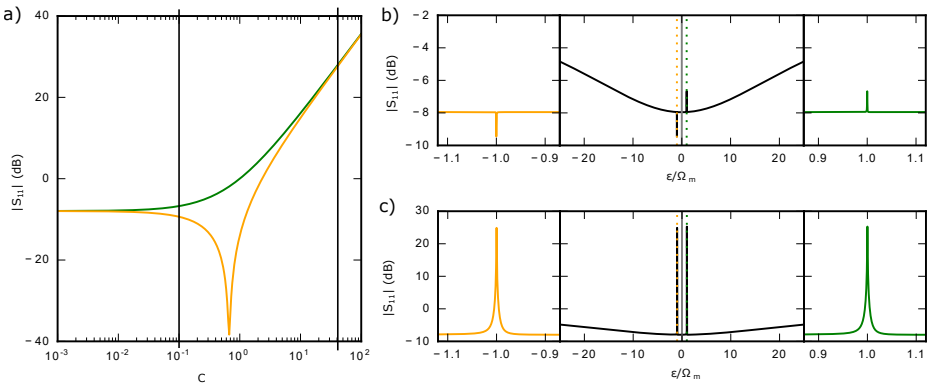

Figure 6.8: (a) The trend of the magnitude of the reflection coefficient of the sidebands, depending on the multi-photon cooperativity. The parameters we chose are for an undercoupled cavity $\eta = 0.3$ and a highly sideband unresolved cavity $\Omega_m/\kappa = 0.01$. The green curve corresponds to $\Omega = +\Omega_m$ and the yellow curve corresponds to $\Omega = -\Omega_m$. There are two linecuts in the figure, one at $C = 0.1$, which is further shown in (b) and another at $C = 30$ which is shown in (c). (b)-(c) Are linecuts where we show the entire cavity response in the center and zoom-ins of the upper (green) and lower (yellow) sidebands on the sides.

6

AMPLIFICATION FOR $\Omega = -\Omega_M$

When we probe on the red side of the drive, the physical mechanisms are essentially identical to the blue detuned probe. We get

$$a_- = \frac{\sqrt{\kappa_e}}{\kappa/2 + i\Omega_m} s_0 + \frac{\kappa}{2} C \frac{\sqrt{\kappa_e}}{(\kappa/2 + i\Omega_m)^2} s_0 \tag{6.34}$$

and

$$S_{11} = 1 - \frac{\kappa_e}{\kappa/2 + i\Omega_m} - C \frac{\kappa\kappa_e/2}{(\kappa/2 + i\Omega_m)^2}. \tag{6.35}$$

6.9. APPENDIX: DOUBLE MIXER AMPLIFICATION

The amplification mechanism can be understood as a frequency mixing circuit as depicted in Fig. 6.7. Note that this assumes that there are no dynamical effects, as this model is most accurate when the drive tone is at the center of the cavity frequency. There are two frequency mixing steps in this optomechanical amplifier. First, the probe and drive tone interfere and beat at their difference frequency, which is the same as the mechanical frequency Ω_m. Due to the radiation pressure force, the mechanical resonator is coherently driven by the amplitude modulations. The mechanical resonator is also coupled to the cavity frequency, and the cavity response will oscillate. Since the drive tone is tuned to the center, it will only experience phase modulation, the magnitude of this being proportional to the slope of the cavity phase response at the center frequency. The sidebands then created from the drive tone are of equal magnitude, but opposite

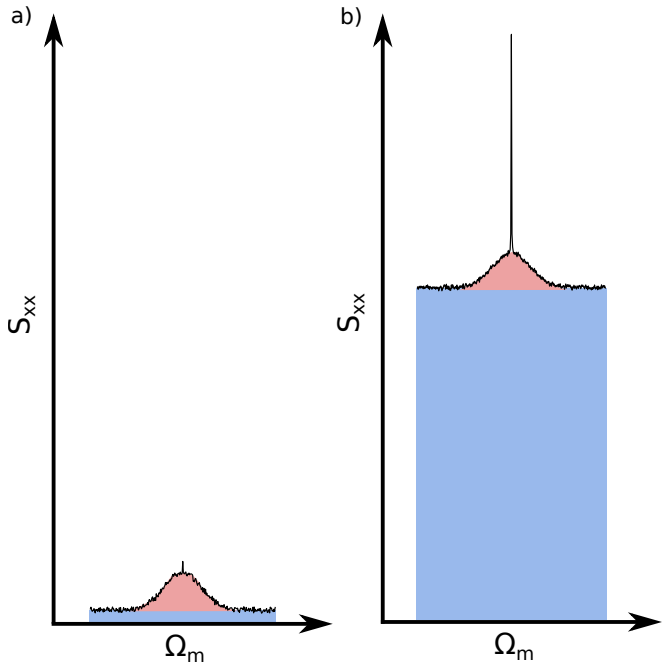

Figure 6.9: A schematical description of how quantum-limited amplification is possible in this optomechanical system. Both graphs show the power spectral density of the mechanical oscillator and are a combination the quantum noise floor (blue area), thermal noise (red area) and a delta peak which is driven by the beating of the pump and probe. (a) At low pump power, the thermal noise is quit large compared to the quantum noise floor. (b) At high powers, both the delta peak and noise floor are increased in magnitude, but the thermal noise stays the same. Taken to sufficiently high powers, the thermal noise is insignificant compared to the quantum noise.

phase, and thus interfere with the probe tone in opposite directions, as shown in the last term of Eq. (6.20). This effect is visually shown in Fig. 6.8. When the magnitude of the sidebands are smaller than the magnitude of the reflected probe tone, one can see in Fig. 6.8(b) that the interference is destructive for the lower sideband and constructive for the upper sideband. Note that this effect is exactly the opposite for the upper and lower sidebands when the cavity is overcoupled such that the slope of the phase is equal but opposite in sign. When the pump power is increased such that the sidebands are of a far greater magnitude than the reflected probe tone, it overpowers the probe tone and both detunings converge to the same high gain value in magnitude.

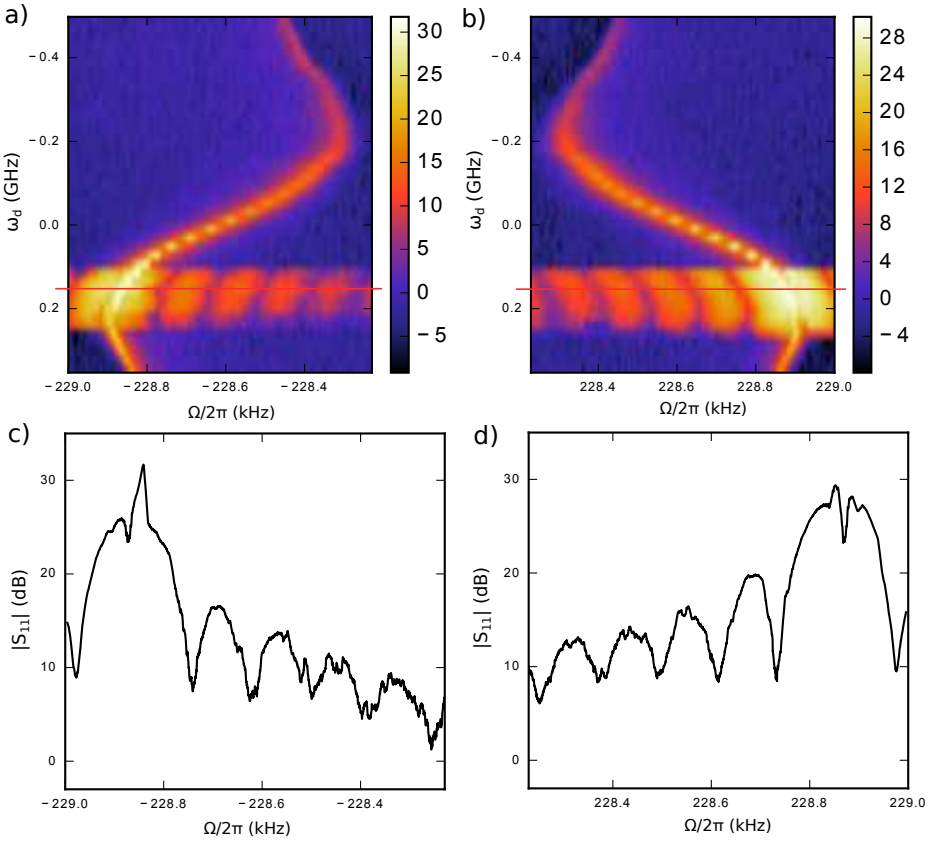

Figure 6.10: A 2D plot showing the magnitude of the reflection coefficient with respect to the drive tone and the probe detuning around $\Omega \sim -\Omega_m$ (a) and $\Omega \sim +\Omega_m$ (b) at -9 dBm input power at the cavity. The optical spring effect is expressed as a detuning-dependent mechanical frequency. However, when the drive detuning is positively detuned, we see an artifact which seems to be self-oscillations. The red line in (a) corresponds to the linecut taken for (c). Likewise, the red line in (b) is plotted in (d).

6.10. APPENDIX: INTUITION BEHIND QUANTUM-LIMITED AMPLIFICATION

An amplifier is said to be quantum limited if the dominant cause of noise in the amplified signal is due to quantum processes instead of thermal noise. Fig. 6.9 gives a diagrammatic explanation of how our system would allow quantum-limited amplification provided the drive tone is strong enough. Thermal noise of the mechanical mode is a Lorentzian distribution in the power spectral density centered around the mechanical resonance frequency where the area is proportional to the average number of phonons. Coherently driving this mode using the beating of the probe and pump tone will excite

a delta peak inside of the Lorentzian profile, as seen in Fig. 6.9. The important part is that no matter how strong the drive tone is, the thermal peak will stay the same size, while the delta peak will increase. Furthermore, the probe tone will inevitably have a small frequency-independent quantum noise floor, indicated by the blue areas. Once the power is sufficient such that the thermal noise if proportionally insignificant to the amplified quantum noise, the amplification is said to be quantum-limited.

6.11. APPENDIX: OPTICAL SPRING EFFECT

We detune the drive tone from the cavity resonance and observe the optical spring effect[21] – a mechanical spring constant, hence also frequency, that is dependent on the drive detuning – in both the upper and lower sidebands of the OMIR signal. We observe a deviation which spans 580 Hz which is $\approx 27\Gamma_m$. A byproduct of optical damping is that one can decrease the mechanical linewidth to such an extent that the effective loss rate becomes negative, indicating self-oscillations, which can be seen for our system in Fig. 6.10(c)-(d) for both negative and positive probe detunings. The measurement takes the shape of a Fraunhofer diffraction pattern when we seep the probe tone of the vector network analyzer.

REFERENCES

[1] A. Wallraff, D. I. Schuster, A. Blais, L. Frunzio, R.-S. Huang, J. Majer, S. Kumar, S. M. Girvin, and R. J. Schoelkopf, *Strong coupling of a single photon to a superconducting qubit using circuit quantum electrodynamics,* Nature **431**, 162 (2004).

[2] C. Regal, J. Teufel, and K. Lehnert, *Measuring nanomechanical motion with a microwave cavity interferometer,* Nature Physics **4**, 555 (2008).

[3] J. Teufel, T. Donner, D. Li, J. Harlow, M. Allman, K. Cicak, A. Sirois, J. D. Whittaker, K. Lehnert, and R. W. Simmonds, *Sideband cooling of micromechanical motion to the quantum ground state,* Nature **475**, 359 (2011).

[4] A. A. Clerk, M. H. Devoret, S. M. Girvin, F. Marquardt, and R. J. Schoelkopf, *Introduction to quantum noise, measurement, and amplification,* Reviews of Modern Physics **82**, 1155 (2010).

[5] A. Roy and M. Devoret, *Introduction to parametric amplification of quantum signals with josephson circuits,* Comptes Rendus Physique **17**, 740 (2016).

[6] R. Movshovich, B. Yurke, P. Kaminsky, A. Smith, A. Silver, R. Simon, and M. Schneider, *Observation of zero-point noise squeezing via a josephson-parametric amplifier,* Physical review letters **65**, 1419 (1990).

[7] D. Riste, M. Dukalski, C. Watson, G. De Lange, M. Tiggelman, Y. M. Blanter, K. Lehnert, R. Schouten, and L. DiCarlo, *Deterministic entanglement of superconducting qubits by parity measurement and feedback,* Nature **502**, 350 (2013).

[8] A. Reed, K. Mayer, J. Teufel, L. Burkhart, W. Pfaff, M. Reagor, L. Sletten, X. Ma, R. Schoelkopf, E. Knill, *et al., Faithful conversion of propagating quantum information to mechanical motion,* Nature Physics **13**, 1163 (2017).

[9] N. Ofek, A. Petrenko, R. Heeres, P. Reinhold, Z. Leghtas, B. Vlastakis, Y. Liu, L. Frunzio, S. Girvin, L. Jiang, *et al., Extending the lifetime of a quantum bit with error correction in superconducting circuits,* Nature **536**, 441 (2016).

[10] M. Aspelmeyer, T. J. Kippenberg, and F. Marquardt, *Cavity optomechanics,* Reviews of Modern Physics **86**, 1391 (2014).

[11] F. Massel, T. Heikkilä, J.-M. Pirkkalainen, S.-U. Cho, H. Saloniemi, P. J. Hakonen, and M. A. Sillanpää, *Microwave amplification with nanomechanical resonators,* Nature **480**, 351 (2011).

[12] C. Eichler and A. Wallraff, *Controlling the dynamic range of a josephson parametric amplifier,* EPJ Quantum Technology **1**, 2 (2014).

[13] C. Ockeloen-Korppi, E. Damskägg, J.-M. Pirkkalainen, T. Heikkilä, F. Massel, and M. Sillanpää, *Low-noise amplification and frequency conversion with a multiport microwave optomechanical device,* Physical Review X **6**, 041024 (2016).

[14] C. Ockeloen-Korppi, E. Damskägg, J.-M. Pirkkalainen, T. Heikkilä, F. Massel, and M. Sillanpää, *Noiseless quantum measurement and squeezing of microwave fields utilizing mechanical vibrations,* Physical review letters **118**, 103601 (2017).

[15] C. Ockeloen-Korppi, T. Heikkilä, M. Sillanpää, and F. Massel, *Theory of phase-mixing amplification in an optomechanical system,* Quantum Science and Technology **2**, 035002 (2017).

[16] M. Yuan, V. Singh, Y. M. Blanter, and G. A. Steele, *Large cooperativity and microkelvin cooling with a three-dimensional optomechanical cavity,* Nature communications **6** (2015).

[17] A. Noguchi, R. Yamazaki, M. Ataka, H. Fujita, Y. Tabuchi, T. Ishikawa, K. Usami, and Y. Nakamura, *Ground state cooling of a quantum electromechanical system with a silicon nitride membrane in a 3d loop-gap cavity,* New Journal of Physics **18**, 103036 (2016).

[18] V. Singh, B. H. Schneider, S. J. Bosman, E. P. Merkx, and G. A. Steele, *Molybdenum-Rhenium alloy based high-Q superconducting microwave resonators,* Applied Physics Letters **105**, 222601 (2014).

[19] P.-L. Yu, T. Purdy, and C. Regal, *Control of material damping in high-q membrane microresonators,* Physical review letters **108**, 083603 (2012).

[20] S. Weis, R. Rivière, S. Deléglise, E. Gavartin, O. Arcizet, A. Schliesser, and T. J. Kippenberg, *Optomechanically induced transparency,* Science **330**, 1520 (2010).

[21] M. Hossein-Zadeh and K. J. Vahala, *Observation of optical spring effect in a microtoroidal optomechanical resonator,* Optics letters **32**, 1611 (2007).

7

CONCLUSIONS

This is the part where I give a summary of this thesis and tie it up into a bigger picture. My thesis is called "Optomechanics in a 3D microwave cavity" because a 3D cavity was the device that I used to obtain my results, but each experimental chapter gives insights into specific elements relevant to an optomechanical system. I will summarize them individually and give them an outlook in the following sections.

7.1. HIGH Q-FACTOR SILICON NITRIDE MEMBRANES

In chapter 4 we observed an exponential increase in the quality factor of a commercial store-bought square silicon nitride membrane at millikelvin temperatures. Most quality factor measurements of membranes are performed with a laser interferometer, however, implementing a laser into a dilution refrigerator is a whole engineering problem itself and often has the unwanted effect of heating up your system. In our system we go around this problem by incorporating our square membrane into an optomechanical device in the microwave frequency regime. This allows easy driving through radiation pressure instead of piezo actuation. We observed a massive increase in quality factor for the fundamental frequency of the square membrane. Interestingly, we observed a huge discrepancy between the two degenerate second modes. We see that the geometry of the mode does have a great factor and is a big indication that radiation losses are still significant. We attribute the increase in quality factor to a dispersively coupled TLS, however, the exact microscopic origin of this effect is difficult to determine.

This paper follows a common trend in nanomechanics to engineer a mechanical resonator to be as lossless as possible, and many groups have used different techniques to achieve this goal. Almost a decade ago, it was discovered that a simple technique for increasing the quality factor of nanomechanical resonators was to increase the tensile stress as this would increase the total stored energy, but only marginally increase the loss per oscillation cycle [1]. A group in Yale discovered that commercial silicon nitride membranes developed for transmission electron microscopy windows also had excellent mechanical properties, and also showed a trend towards increasing quality factor at lower temperatures [2]. These silicon nitride membranes have also been used to serve as a window for coupling electromagnetic and optical modes [3]. Since our paper, much progress has been made to further increase this Q-factor limit. One of the most promising candidates has been reported in the paper by Tsaturyan et al. [4] where they achieve a quality factor above 10^8 at room temperature. Their technique is to pattern a phononic cavity into the membrane itself to create a phononic shield which limits radiation losses. Their system provides soft clamping, where the radius of curvature of the bending is minimized thereby also reducing internal losses.

7.2. 3D CAVITIES WITH DC BIAS ACCESS

In chapter 5 we tried our solution to the problem of inserting a DC bias into a device embedded into a 3D cavity. 3D cavities have the benefit that they have extremely high quality factors compared to planar resonators [5, 6], however, incorporating a DC bias is difficult. Most other attempts have tried to insert electrodes into the cavity, but this

comes with the added price of greatly reducing the quality factor [7] due to the necessity of adding a hole which increases radiation losses. We demonstrated a design for incorporating a DC bias into a 3D microwave cavity. We did this by turning the walls of the 3D cavity into electrodes by splitting the cavity along the direction of current flow. We show that we are able to attain intrinsic quality factors as high as $Q = 9 \times 10^5$ at the single photon level.

The cavity was a proof-of-concept, and we did not demonstrate an actual device at millikelvin temperatures. At room temperature we used a diode as an example, but this cannot be used at too low temperatures. An integrated 3D cavity device with a tuneable transmon qubit would be a great way to show the feasibility of this split cavity design in quantum circuit electrodynamics experiments.

7.3. MICROWAVE AMPLIFICATION USING OPTOMECHANICS

Optomechanical systems can be used as a device for microwave signal amplification, and have been demonstrated using a few different methods [8–11]. Due to the radiation pressure force in optomechanics it is possible to influence the loss rate of the mechanical oscillator using a light field which is detuned from the cavity resonance. The first method showed that it was possible to amplify microwave tones through an amplified mechanical mode [8]. The issue that came with this was that the mechanical oscillator was too low in frequency to have a negligible amount of thermal noise. Other methods used a protocol where the mechanical element was both cooled and heated at the same time to avoid the thermal noise of the mechanical oscillator becoming significant. All these method depended on the optomechanical system being in the sideband-resolved limit.

Our device showed that it is possible to amplify a microwave signal using an optomechanical cavity that was not inside the sideband-resolved limit. The method depends on *driving* instead of *amplifying* the mechanics, and thus avoids the risk of adding the mechanic's thermal noise to the microwave tone. The device can be understood as a double-mixer circuit where the two mixing steps are the driving of the mechanics using the beating of the two tones, and the modulation of the drive tone, creating the sidebands at the signal frequency. This model is in fact applicable to any optomechnical system, however the threshold for high gain is lower when the cavity is not sideband-resolved.

A logical next step is to demonstrate the possibility of having it behave as a quantum-limited amplifier. For the device to behave as such, an inequality must be satisfied $C > n_{\text{th}}$, where C is the cooperativity, and n_{th} is the average number of phonons in the bath. To achieve this, we would have to improve on the coupling rate and the mechanical quality factor, because we would ideally want to keep the quality factor of the cavity as low as possible to increase the bandwidth of the amplifier.

REFERENCES

[1] Q. P. Unterreithmeier, T. Faust, and J. P. Kotthaus, *Damping of nanomechanical resonators,* Physical review letters **105**, 027205 (2010).

[2] B. Zwickl, W. Shanks, A. Jayich, C. Yang, A. Bleszynski Jayich, J. Thompson, and J. Harris, *High quality mechanical and optical properties of commercial silicon nitride membranes,* Applied Physics Letters **92**, 103125 (2008).

[3] R. W. Andrews, R. W. Peterson, T. P. Purdy, K. Cicak, R. W. Simmonds, C. A. Regal, and K. W. Lehnert, *Bidirectional and efficient conversion between microwave and optical light,* Nature Physics **10**, 321 (2014).

[4] Y. Tsaturyan, A. Barg, E. S. Polzik, and A. Schliesser, *Ultracoherent nanomechanical resonators via soft clamping and dissipation dilution,* Nature nanotechnology **12**, 776 (2017).

[5] M. Reagor, H. Paik, G. Catelani, L. Sun, C. Axline, E. Holland, I. M. Pop, N. A. Masluk, T. Brecht, L. Frunzio, *et al.*, *Reaching 10 ms single photon lifetimes for superconducting aluminum cavities,* Applied Physics Letters **102**, 192604 (2013).

[6] T. Brecht, M. Reagor, Y. Chu, W. Pfaff, C. Wang, L. Frunzio, M. Devoret, and R. Schoelkopf, *Demonstration of superconducting micromachined cavities,* Applied Physics Letters **107**, 192603 (2015).

[7] W.-C. Kong, G.-W. Deng, S.-X. Li, H.-O. Li, G. Cao, M. Xiao, and G.-P. Guo, *Introduction of dc line structures into a superconducting microwave 3d cavity,* Review of Scientific Instruments **86**, 023108 (2015).

[8] F. Massel, T. Heikkilä, J.-M. Pirkkalainen, S.-U. Cho, H. Saloniemi, P. J. Hakonen, and M. A. Sillanpää, *Microwave amplification with nanomechanical resonators,* Nature **480**, 351 (2011).

[9] C. Ockeloen-Korppi, T. Heikkilä, M. Sillanpää, and F. Massel, *Theory of phase-mixing amplification in an optomechanical system,* Quantum Science and Technology **2**, 035002 (2017).

[10] C. Ockeloen-Korppi, E. Damskägg, J.-M. Pirkkalainen, T. Heikkilä, F. Massel, and M. Sillanpää, *Low-noise amplification and frequency conversion with a multiport microwave optomechanical device,* Physical Review X **6**, 041024 (2016).

[11] C. Ockeloen-Korppi, E. Damskägg, J.-M. Pirkkalainen, T. Heikkilä, F. Massel, and M. Sillanpää, *Noiseless quantum measurement and squeezing of microwave fields utilizing mechanical vibrations,* Physical review letters **118**, 103601 (2017).

SUMMARY

This thesis explores certain technologies that are related to the field of cavity optomechanics; specifically, optomechanics where the cavity is a 3D microwave cavity.

In chapter 1 we give a broad introduction to the field, starting with its basic element: the harmonic oscillator. From this starting point we try to make the reader understand the physical principles behind an optomechanical system at the undergraduate level. Emphasis is put more on pedagogy and historical context rather than precision.

Chapter 2 gives a rigorous theoretical background to many of the concepts which are discussed in the previous chapter. Again, we start from the simple harmonic oscillator and add a loss term, and eventually add a driving term. This model is used to describe both the mechanical oscillator and the electromagnetic mode which is situated inside the 3D microwave cavity. The electromagnetic mode is given further attention to derive the formula for the reflection coefficient which is often the first step into characterizing your optomechanical system. Next, the two modes are connecting using an interaction term and the full optomechanical equations of motion are derived. Subsequently, the mechanical mode is studied on its own, most importantly, the mechanism of the loss channels. The same is done for the electromagnetic mode.

Chapter 3 explores the fabrication techniques which were employed in the construction of the devices in this thesis. A few different methods for metalizing the silicon nitride membranes from the Canadian company NORCADA are discussed, and their difficulties and why certain techniques are preferred over others. We also discuss the complete fabrication of other types of silicon nitride membranes, geometries we call trampolines. Metalization of these structures is also mentioned. The fabrication of other elements of our full 3D microwave cavity optomechanical are mentioned: the cleaning procedure of the pure aluminium cavities, and the construction of the antenna chips on which we put the metalized membranes. We spend some time discussing the intricacies of performing the flip-chip procedure. Lastly, we discuss the cryogenic measurement setups that we employed for our experiments.

Chapter 4 is the first chapter which goes into depth about some of the results obtained in this thesis. We demonstrate a temperature dependence of the quality factor of a metalized NORCADA silicon nitride membrane. We observe the fundamental mode of the membrane to reach up to $Q = 10^8$ at 16 mK. We also see a strong dependence of the mechanical mode shape on the quality factor, such as the (2,1) mechanical mode showing no temperature dependence at all. We attribute this to radiation losses into the substrate.

In chapter 5 we show a 3D cavity setup which allows easy access of a DC voltage bias to a device inside the cavity. We do this by cutting the 3D cavity along the axis of current flow, such that the radiation losses are minimized. The dependence of the size of

the gap on the quality factor of the 3D cavity is measured and discussed. Furthermore, we implement an experiment where we enter the full 3D cavity setup into a dilution refrigerator at 15 mK and show that there is no degradation of the quality factor when biasing the cavity up to 30 V, and show no measurable power dependence.

Chapter 6 explores an optomechanical amplification method which makes use of a cavity which has a relatively low quality factor. Usual amplification schemes rely on having a drive which is detuned from the cavity resonance to use dynamical backaction to its advantage. Our setup relies solely on frequency mixing effects which are independent of dynamical backaction and can thus be tuned over the entire width of the cavity response. Our method also has the ability to allow for amplification which is only limited by quantum noise.

Chapter 7 is a conclusion chapter which tries to bring the whole thesis into a broader picture and shows the way forward for certain techniques to be applied to other future experiments.

SAMENVATTING

Dit proefschrift onderzoekt bepaalde technologieën die verband houden met het gebied van cavity optomechanica; optomechanica waarbij de cavity een 3D supergeleidende holte is.

In hoofdstuk 1 geven we een brede inleiding op het veld, beginnend met zijn basis element: de harmonische oscillator. Vanaf dit startpunt proberen we de fysische principes achter een optomechanisch systeem te introduceren. De nadruk ligt meer op pedagogie en historische context in plaats van nauwkeurigheid.

Hoofdstuk 2 geeft een grondige theoretische achtergrond voor veel van de concepten die worden besproken in het vorige hoofdstuk. Nogmaals, we beginnen met de harmonische oscillator en voegen een verliesterm toe en voegen uiteindelijk een driving term toe. Dit model wordt gebruikt om zowel de mechanische oscillator als de elektromagnetische modus te beschrijven die zich in de 3D holte bevindt. De elektromagnetische modus krijgt extra aandacht voor het afleiden van de formule voor de reflectiecoëfficiënt. Vervolgens verbinden we de twee modi met behulp van een interactieterm en het volledige optomechanische vergelijkingen is dan afgeleid. Vervolgens wordt de mechanische modus bestudeerd, vooral het mechanisme van de verlieskanalen. Hetzelfde word gedaan voor de elektromagnetische modus.

Hoofdstuk 3 onderzoekt de fabricagetechnieken die in de constructie werden gebruikt van de apparaten in dit proefschrift. Een paar verschillende methoden voor het metalliseren van de siliciumnitride membranen van het Canadese bedrijf NORCADA worden besproken, en hun moeilijkheden en waarom bepaalde technieken de voorkeur hebben boven andere. Wij brespreken ook de complete fabricage van andere typen siliciumnitridemembranen, geometrieën die we trampolines noemen. Metalisatie van deze structuren wordt ook beschreven. De fabricage van andere elementen van onze volledige 3D cavity optomechanisch systeem worden bestudeerd: de reinigingsprocedure van de puur aluminium holtes, en de constructie van de antennechips waarop we de gemetalliseerde membranen plaatsen. Wij besteden wat tijd aan het bespreken van de fijne details van het uitvoeren van de flip-chip-procedure. Ten slotte bespreken we de cryogene meetopstellingen die we hebben gebruikt voor onze experimenten.

Hoofdstuk 4 is het eerste hoofdstuk dat dieper ingaat op enkele resultaten verkregen in dit proefschrift. We demonstreren een temperatuurafhankelijkheid van de Q-factor van een gemetalliseerde NORCADA siliciumnitride membraan. We observeren dat het fundamentele modus van het membraan $Q = 10^8$ bij 16 mK bereikt. We zien ook een sterke afhankelijkheid van de mechanische modusvorm op de kwaliteitsfactor, zoals de (2,1) mechanische modus die helemaal geen temperatuurafhankelijkheid vertoont. Wij geloven dat dit word veroorzaakt door stralingsverliezen in het substraat.

In hoofdstuk 5 laten we een 3D cavity-opstelling zien die een gemakkelijke toegang

tot een gelijkspanning mogelijk maakt. We doen dit door de 3D-holte langs de as van de stroom te snijden, zodat de stralingsverliezen tot een minimum worden beperkt. De afhankelijkheid van de grootte van de opening op de kwaliteitsfactor van de 3D-holte wordt gemeten. Bovendien implementeren we een experiment waarbij we de volledige 3D cavity systeem binnen een koelkast stoppen tot 15 mK en laten zien dat er geen degradatie van de kwaliteitsfactor word veroorzaakt.

Hoofdstuk 6 onderzoekt een optomechanische amplificatiemethode die gebruikt maakt van een holte die een relatief lage kwaliteitsfactor heeft. Gebruikelijke amplificatieschema's vertrouwen op het gebruik van dynamische backaction door het systeem aan te drijven met een lagere of hogere frequencie dan de resonatiefrequencie. Onze opstelling is uitsluitend afhankelijk van frequentie-mixeffecten die onafhankelijk zijn van dynamische backaction en dus kunnen worden afgestemd op de volledige breedte van de caviteitsreactie. Onze methode heeft ook de mogelijkheid om toe te staan versterking die alleen wordt beperkt door kwantumruis.

Hoofdstuk 7 is een conclusie hoofdstuk dat probeert de hele these in één te brengen en toont de weg vooruit.

CURRICULUM VITÆ

Martijn Antonio COHEN

28-10-1992 Born in New York, United States.

EDUCATION

2008–2010 International Bacchalaureate
American School of Paris, France

2012 Internship
BASF, Ludwigshafen, Germany

2013 Internship
KiloLambda, Tel Aviv, Israel

2010–2014 M.Sci. in Chemical Physics
University College London, United Kingdom
Thesis: Interactions between protein and amphiphilic block-copolymer structures
Supervisor: Prof. G. Battaglia

2015–2019 Ph.D. in Physics
Technical University of Delft, the Netherlands
Thesis: Optomechanics in a 3D microwave cavity
Promotor: Prof. dr. G. A. Steele
Promotor: Prof. dr. Y. M. Blanter

List of Publications

3. **M. A. Cohen***, D. J. Bothner*, Y. M. Blanter, G. A. Steele, *Optomechanical microwave amplification without mechanical amplification*, arXiv:1812.05459

2. **M. A. Cohen**, M. Yuan, B. W. A. de Jong, E. Beukers, S. J. Bosman, G. A. Steele, *A split-cavity design for the incorporation of a DC bias in a 3D microwave cavity*, Applied Physics Letters **110**, 172601 (2017)

1. M. Yuan, **M. A. Cohen**, G. A. Steele, *Silicon nitride membrane resonators at millikelvin temperatures with quality factors exceeding* 10^8, Applied Physics Letters **107** 263501 (2015)

ACKNOWLEDGEMENTS

The acknowledgements section is the part where I show gratitude to the dozens of people which contributed, however indirectly, to the completion and success of this dissertation – a glorified 'credits' section to this four-year long movie. Unlike in movies, however, this section will probably achieve the highest readership. So for your beloved entertainment, I will try my best to wrap my gratitude into an interesting narrative on my PhD experience. In keeping with the movie metaphor, I shall introduce the characters *in order of appearance*. Roughly.

Gary, you were my first point of contact into this world of academia, and you have been the most important, too. I remember scanning through your website and found that you had posted an available position in something called nanomechanics. I was intrigued. But also, I was impressed by your openness. I don't remember exactly the wording that was used, but you had a sentence on your website which could be paraphrased as *come schedule a meeting if you want to have a chat.* And so I did, and I could immediately tell that you would be a great supervisor to work for. You have a contagious enthusiasm for explaining anything physics, and, miraculously, this enthusiasm remains even after being asked to re-explain for the third time. Beyond research, however, you tend to treat your PhD students well, you show an appreciation for work-life balance, and you are accepting of people's flaws. I am rooting hard for your success (and the whole of SteeleLab), not because I am an alumnus, but because you deserve it.

In the beginning, SteeleLab numbered few. Salomon, I feel like I owe you for the massive amounts of help you gave me in the beginning. I enjoyed our not-always-sober conversations on random topics, and even though some of our views run orthogonally, they always gave me an interesting perspective. I also envy your ability to insert physics metaphors into any subject (e.g. "Judaism has a very large Q-factor"). Best of luck with your company, Delft Circuits, or as I also like to call it, SteeleLab's official ex-student recruiter. Mingyun, thank you for helping me out with all intricacies regarding flipping chips and soldering cables. I hope you are enjoying your new scientific post in Berlin. My sincerest thanks also extend towards Shun and Vibhor; I remember you guys also having to put up with my countless requests for advice and help.

Slowly, SteeleLab started growing, and it started with a guy who permanently wears his jacket. DJ Bothner (the J stands for Jacket), I was very happy when I heard you would be joining the team. (Side note: when I started my PhD I remember counting all the nationalities in our department and was surprised to find not even one German. You were one of the first Germans to join. And now it's swimming with them! I promise this is not the start of a World War 2 joke.) Anyway, I definitely think we formed a close bond, a bond which mostly revolved around eating kebab for lunch, but some physics, too. We were truly blessed with the long overdue arrival of the food trucks and SPAR.

On a serious note, though, your scientific contributions to my PhD, after Gary, probably ranks highest. So thank you! The second to join, was a scientist who has since been in a superposition between our lab and that of the molecular guys: Nikos. Is he in our lab or in Herre's lab? You can only know for sure once you observe him. Although perhaps our scientific lives did not overlap much, we shared a great adventure in an exotic land, a place filled with snakes, elephants, and tigers. Literally. You are next in line to graduate, and I hope it goes as smoothly as your scientific knowledge would suggest.

Then came the soon-to-be cleanroom guru, Felix. (He prefers the name Fortunato, though.) First of all, thanks for being my paranymph – I hope the suit fits you as naturally as cleanroom garments do. Second of all, I think I, and most of SteeleLab, should be grateful for your attention to *organization*. Without you, the wiki would be a total mess. I am also extremely happy to hear about your engagement to Katrine. However, I can't help but be disappointed that you didn't take my suggestion to get married in a cleanroom suit seriously. A pity. A description of Felix would not be complete without a mention of his loyal graphene-team buddy; a postdoc with a sense of sarcasm so raw, you run the risk of catching Salmonella. Mark, countless thanks for your `git commits`, and your willingness to drop whatever you're doing to answer a question. Although perhaps the move was perceived unusual, I hope you thrive in your new post – remember that there is no shame in going corporate.

Suddenly, about half-way through my own PhD, SteeleLab experienced the research group's equivalent of cosmic inflation – a period of intense expansion of funds, and thus, PhD-student capacity. We were terrified. *So much cleanroom training*. Within a few months, the group practically doubled. Our initial trepidations were subdued by the sense that SteeleLab was... changing. It had reached critical mass and was experiencing a phase transition. We started going on *uitjes* and dinners together; social gatherings with emphasis on the non-scientific aspects of being a scientist. Lunch together also became a daily affair, and we adopted the habit of convening at the first floor lunch table, to discuss important topics such as the Dutch healthcare system and also the Dutch healthcare system. I want to show my gratitude to this second wave of PhD students, although the order of their arrival eludes me.

Sarwan, you have been my office buddy for almost two years now, and you have taken on the task of continuing my project. May you flip chips as best as anyone can. We shared some great conversations – about things that made us different and things that bolstered our similarities. Don't lose hope if things don't move as quickly as you want. Mario, you epitomize the phrase *a day of calculation can save a year in the laboratory*. Thanks for your readiness at joining my daily pilgrimage for decent lunch food. Marios, you made the conversion from QuTech to QN for all the right reasons, and you *shouldn't* [pun omitted] ever have any doubts about that. Yıldız, thank you for always being down for a good party, and for delighting in the scary treck to Rotterdam. Inês, I hope one day you chase that dream of being a fitness instructor in LA. But for now, science is king. Keep pushing. Byoung-Moo, I've heard legendary stories of your veiled sense of humor, perhaps one day I will experience it in person. Good luck with your project. To the new postdocs, Hadi and Fatemeh; although we haven't had much opportunity to collaborate,

I am sure both SteeleLab and the Netherlands will treat you well. To the current master and bachelor students: keep believing in yourself. And consider applying to Delft Circuits.

This concludes the acknowledgements of my closest scientific next-of-kin – the ones with whom I share a supervising professor – and we change scenery to a new location with new characters: the cleanroom. For the non-scientific folk reading, I believe a small introduction to the place that I spent next to half of my time in, is in order. The next paragraph is an explanatory interlude, and is read best in the voice of a condescending man with a Mid-Atlantic accent.

The cleanroom. An amalgamation of the words *clean* and *room*. *Clean*, because, well, this place is clean. Not so much in the same sense as hospitals, but in the sense that there are very elaborate ventilation systems installed such that there is an as-small-as-possible concentration of dust particles floating in the air. Why? Because this laboratory facilitates the fabrication of tiny, fragile chips, and a dust particle which is small – even imperceptible – to us, is destructive at the nanoscale. The suffix *room* is a lie, because this place is not a room. It's a palace, factory, dungeon, Disneyland, state-of-being, depending on whom you ask and what mood they're in. Entering this place is no easy task; you might have taken a shower today, but by cleanroom standards, you're not clean. You must first dress from head to toe in a protective fabric which shields the cleanroom from all particles which likely adhere to your clothes, hair, and body. The requirement of protective garments is twofold, however; this laboratory contains reactants and etchants which could severely harm you if it came into contact with your skin. The overall process is cumbersome and requires extensive training, but is a strict necessity for performing cutting-edge research at the nanoscale.

In this cleanroom, I met many great people. First of all, my sincerest thanks to the staff of the Kavli Nanolab. Marco, Marc, Anya, Ewan, Eugene, Arnold, Charles, Frank, to name a few. There's a reason why I have heard quite a few visiting scientists admit that the facilities in Delft are world-leading. I also became close to the members of GröblacherLab, or GLab – our scientific cousins – in the cleanroom. In many cases our fabrication procedures overlapped (despite their phobia for metals), and so we exchanged ideas, tips, and occasional complaints. The first person to mention is the group's eponymous leader, Simon. In many occasions you served as a second supervisory voice in the field of optomechanics, a counterpoint to Gary's melody. Thanks for your help. João, your fabrication stint was short-lived, but sweet (I hope?). Thanks for helping me with measuring trampolines, and for the culinary advice on Rotterdam restaurants. Words of a *connoisseur*. Richard, you were actually one of the first people I met here, because I remember running into you at the kebab place before I had even started my PhD. Thanks for countless amount of advice and help, and, of course, for being on my committee. Congratulations on achieving professorship, too! Claus, you have often played the role of the wise man with prophetic metaphors on the struggles of PhD life. I share with everyone one of your most poetic: "If you're in the middle of the ocean and you don't see land, you're gonna drown." Moritz, thanks for providing comic relief in between fabrication steps. Andreas and Igor, you guys make everyone's publication record

look amateurish. Keep up the good work! A few other characters often provided the role of fabrication consultant: Alessandro, Nikolai, and David. Thanks a lot!

I want to dedicate the following sentences to persons I had trouble categorizing into the previous paragraphs, but who undoubtedly had a great influence on my PhD experience. I would like to thank the PhD committee for taking the time to read my dissertation and provide feedback. Special thanks go to Eva and Ignacio for having to take the long journey to attend the defence. Yaroslav, you often provided much-needed theoretical wisdom into my work, thank you. João (the theory João), we had a great time going to Les Houches in the beginning of our PhD, and I wish you the best of luck in your continued academic endeavours. My first office mates – Dejan, Mafalda, and Alexandra – thanks for the many conversations and distractions. To my two KuipersLab office mates, Thomas and Felipe, best of luck for whatever scientific adventure awaits. Felipe, special thanks for helping me practice my *castellano*! Many thanks to the plethora of master and bachelor students that I helped supervise, and, reciprocally, helped me out: Alexander, Bas, Lieuwe, Jonathan, Marijn and Ewout. A few QuTech members also deserve gratitude: Suzanne, for the times we struggled through grading QM1 exams; Ramiro, for courageously tolerating spicy food in India; and Chris, for injecting cQED wisdom into SteeleLab.

I now come to my second paranymph. Although the placement of this paragraph seems to suggest a latecomer in my academic life, it is quite the opposite. When I gave my presentation for my PhD application, the person in the audience with the largest appetite for questions was an Indian girl called Nandini. I later learned that she had an even greater appetite for memorizing capital cities and enriching her vocabulary, the latter of which becomes evident by her occasional mispronunciation of words (e.g. *lettyooce*) – a sign of someone who learns through reading. An odd story involving a lizard introduced another person into our friendship; a guy as proud an Eastern European as they come. Ranko, I am even prouder of the fact that you have decided to make Rotterdam your home, and that you will soon take on the Dutch nationality. To both of you, I hope we continue our meetups even once our academic lives are over. An honorary mention must to go Nandini's husband, whom I got to know well when I witnessed their wedding in India; a man whose passion for snakes and reptiles surpasses even his wife's passion for vocabulary (he has scars to prove it). Best of luck with your marriage and life, I hope you two hold your experience in the Netherlands with high regard, despite the lack of reptiles.

Some might have noticed that I have mentioned the city *Rotterdam* a few times. Where is this place? It sounds foreign – and to many Delftians, who relish in the comfort of 5-minute bike rides, it probably is. It is the place in which I chose to keep my residence for four years, in the company of two *hermanos* with personalities so different from mine, it's a surprise this arrangement worked out at all. Two sleazy salesmen and an awkward physicist walk into a bar... I don't know how this joke ends, but perhaps our friendship is the joke. And I mean that in the best way. The truth, however, is that our similarities are far more numerous than our differences. We share a common taste in music, a love for the surreal, and a passion for mimicking *de dutch aksunt*. Vincent

and Fionn, I give you both a copy of this dissertation as a gift, use it in whatever way you see fit. My gratitude also extends – over the Atlantic ocean – to my twin; for being a positive influence in my life, although I wish this influence was as strong as it used to be. Caroline, best of luck on your LA adventure.

We conclude with the last and perhaps most important two people in my life: my loving parents. I owe most things in my life to you, so whenever you feel proud of your son, remember to feel proud of yourself. It is for this reason that I dedicate this thesis in your honor, for getting me this far. Thank you!